Mathematical Modelling of Thixotropic and Antithixotropic Fluids

Catriona R. McArdle

Department of Mathematics and Statistics

University of Strathclyde

Glasgow, UK

April 2013

This thesis is submitted to the University of Strathclyde for the degree of Doctor of Philosophy in the Faculty of Science.

This thesis is the result of the author's original research. It has been composed by the author and has not been previously submitted for examination which has led to the award of a degree.

Signed: Date:

Acknowledgements

I would like to thank the Engineering and Physical Sciences Research Council (EPSRC) for the three and a half years of funding I received from them.

I am indebted to both of my supervisors, David Pritchard and Stephen Wilson, who have guided me through the years with patience and expertise. They told me early on that there was no such thing as a stupid question and I hope they still believe that. I would also like to thank Michelle Taroni for interesting and fruitful conversations.

I have to thank (and apologise to) those in the department who put up with my moaning and who answered countless questions about LaTeX, Maple and printers. Finally, I would like to thank my mum, dad, Eileen, Roisin, Patricia, Siobhan and Paddy who have pretended to have an interest in "that tomato sauce thing" for too long now. They have been supportive and understanding, even during my most stressful days, and most importantly have kept me well fed. I could not have done this without them.

Abstract

In this thesis we consider two fundamental flow problems, the Stokes problem and flow in a slowly-varying channel, for complex fluids. Specifically, we investigate these problems for thixotropic and antithixotropic fluids described by Mewis and Wagner's [*Advances in Colloid and Interface Science*, **147-148**, 214–227 (2009)] general structure parameter model together with a version of the constitutive law proposed by Moore [*Transactions and Journal of the British Ceramic Society*, **58**, 470–494 (1959)]. In certain limits, this model reduces to the generalised Newtonian power-law model, which we also consider.

In chapters 2 and 3 we consider the Stokes problem for power-law, and thixotropic and antithixotropic fluids, respectively. Our main motivation for studying the Stokes problem is to investigate the interplay between the timescales of the fluid response and the forcing. Therefore, the emphasis of our investigations is on the periodic oscillatory behaviour of the systems, rather than on the transient initial phase during which the system adjusts to the attracting periodic solution.

In chapter 4 we consider the two-dimensional flow of a thixotropic or antithixotropic fluid along a slowly-varying channel. Although previous studies have considered similar geometries, ours appears to be the first systematic development of a thin-film theory for a thixotropic or antithixotropic fluid. Like the conventional lubrication approach for a Newtonian fluid, our approach is

based on an asymptotic expansion in powers of the aspect ratio δ in the limit $\delta \to 0$. Under appropriate assumptions concerning the Reynolds number and the dimensionless structure response rates, we obtain the governing equations for the velocity, pressure and structure parameter up to $O(\delta)$. In contrast to the Newtonian case, the lubrication equations include terms at $O(\delta)$, and it is at this order that thixotropic and antithixotropic effects occur.

Contents

Chapter 1

Introduction

1.1 What are non-Newtonian fluids?

This thesis concerns non-Newtonian fluids. In this section we will give a qualitative introduction to non-Newtonian fluids; we will then make these qualitative ideas more precise in section 1.2. Fluids can be defined as either Newtonian or non-Newtonian depending on how they behave when deformed. Newtonian fluids have shear stress which is proportional to the shear rate. Although no fluid can be described exactly by the Newtonian model, it is a very good approximation for many fluids, including water and air (Barnes *et al.* 1989).

In contrast, other common fluids, such as tomato sauce and colloidal suspensions for example muds, change their physical properties when subjected to shear and are therefore non-Newtonian fluids. When tomato sauce (see figure 1.1 a) is shaken it gets "runnier", i.e. its viscosity decreases, but it eventually returns to its original state, i.e. its viscosity increases, when the bottle is put back on the shelf. Cornflour solution behaves in the opposite manner and becomes very "sticky" when a high shear is applied; however, its viscosity starts to decrease when the shear stops (see figure 1.1 b). So running over a cornflour

(a) 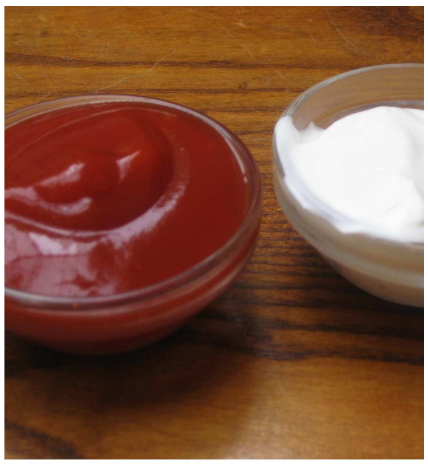 (b) 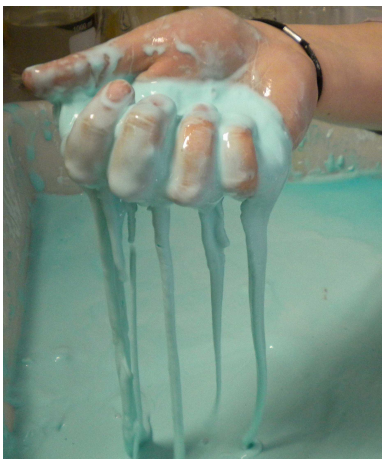

Figure 1.1: (a) Tomato sauce and mayonnaise with kind permission from Joe Brooker (see http://www.flickr.com/photos/9107386@N06/4470879909/). (b) Cornflour solution, with kind permission from Nicole Walshe and Christine Conroy (see http://www.nuigalway.ie/chemistry/kitchenchemistry/experiments/nonnewtonian.html).

solution increases the viscosity of the solution enough to support a person's weight, whereas dipping a hand into the solution does not. Thus, cornflour solution can be used in the popular trick of "walking on water" [1]. Fluids such as tomato sauce which show a decrease in their effective viscosity under shear are known as shear-thinning fluids. Conversely, fluids such as cornflour solution which show an increase in their effective viscosity under shear are known as shear-thickening fluids.

These changes in non-Newtonian fluids depend on the behaviour of their microstructure. Non-Newtonian fluids can have various kinds of microstructure, for example networks of flocculated colloidal particles, tangles of polymers, or spatial arrangements of suspended particles or drops (Barnes 1997). When subjected to high shear rates, the microstructure gradually breaks down or builds up. For example, when shear is applied to a non-Newtonian fluid made up of polymers, the polymers either "comb out" or tangle up, and the

[1] See www.youtube.com/watch?v=GkY2nT-3Glo

fluid becomes less or more viscous.

We extend the definitions of shear-thinning and -thickening fluids to define a thixotropic fluid to be a shear-thinning fluid whose structure takes a finite time to relax to local conditions, and an antithixotropic (or rheopectic) fluid to be a shear-thickening fluid which takes a finite time to relax to local conditions (see, for example, Barnes 1997). Mewis and Wagner (2009) state that it was only relatively recently that agreement was reached on the definition of thixotropy: thixotropic fluids should display a continuous decrease of viscosity with time when flow is applied to a sample that has been previously at rest, and the subsequent recovery of viscosity in time when the flow is discontinued. The converse holds for antithixotropy.

Shear-thinning and thickening behaviour are not the only non-Newtonian effects. In particular, some fluids also exhibit viscoplasticity and/or viscoelasticity.

Viscoplastic materials remain solid until the shear stress has reached a specific value, known as the yield stress, at which point the fluid begins to flow. Common viscoplastic materials are toothpaste, mayonnaise and drilling mud (Raju 2011).

A viscoelastic fluid displays both viscous and elastic behaviour. When stresses are applied to a viscous material the material flows like a liquid. When stresses are applied to a perfectly elastic material the material stretches but returns to its original state when the stress is removed. Viscoelastic fluids display a combination of these behaviours: the applied stresses are accommodated by a combination of stretching and flowing. In this thesis, we will look at purely thixotropic or antithixotropic fluids and neglect viscoplasticity and viscoelasticity effects.

1.2 Mathematical models of rheology

Rheology is the study of the deformation and flow of matter (Barnes, Hutton, and Walters 1989): its name comes from the Greek word "rheos" meaning "to flow". We will set up the mathematical framework of rheology to make the qualitative ideas introduced in section 1.1 more precise.

We start with the generalised Navier-Stokes momentum equation and we use the summation convention throughout[1],

$$\hat{\rho}\frac{\mathrm{D}\hat{u}_i}{\mathrm{D}\hat{t}} = -\frac{\partial}{\partial \hat{x}_i}\hat{p} + \frac{\partial}{\partial \hat{x}_j}\hat{\tau}_{ij}, \tag{1.1}$$

where $\hat{\tau}_{ij}$ is the deviatoric stress tensor, $\mathrm{D}/\mathrm{D}\hat{t} \equiv \partial/\partial\hat{t} + \hat{\mathbf{u}} \cdot \hat{\nabla}$ is the convective derivative, $\hat{\mathbf{u}}$ is the flow velocity with components $\hat{u}_i$, $\hat{\rho}$ is the density, $\hat{p}$ is the pressure and $\hat{t}$ is time. (Here and throughout this thesis, unless otherwise stated, carets denote dimensional quantities, while dimensionless quantities are unadorned.) The task of a rheological model is to determine $\hat{\tau}_{ij}$.

We now introduce the symmetrised shear rate tensor $\hat{e}_{ij}$, the total shear rate $\dot{\gamma}$ and the shear stress $\hat{\tau}$,

$$\hat{e}_{ij} = \frac{\partial \hat{u}_i}{\partial \hat{x}_j} + \frac{\partial \hat{u}_j}{\partial \hat{x}_i}, \quad \dot{\gamma} = \sqrt{\frac{1}{2}\hat{e}_{ij}\hat{e}_{ij}} \quad \text{and} \quad \hat{\tau} = \sqrt{\frac{1}{2}\hat{\tau}_{ij}\hat{\tau}_{ij}}. \tag{1.2}$$

Using these quantities we can define shear–stress relations for specific models, starting with the Newtonian model.

[1] When a suffix appears twice in any single term in an expression then it is implicitly summed, e.g. $a_j b_j = \sum_j a_j b_j$ for any a_j or b_j.

1.2.1 Newtonian fluids

For a Newtonian fluid, $\hat{\tau}_{ij}$ is defined by

$$\hat{\tau}_{ij} = \hat{\mu}\hat{e}_{ij}, \tag{1.3}$$

where $\hat{\mu}$ is a scalar constant of proportionality, the Newtonian dynamic viscosity. The kinematic viscosity $\hat{\nu}$ is related to $\hat{\mu}$ through the relation $\hat{\nu} = \hat{\mu}/\hat{\rho}$.

To illustrate the Newtonian model we consider how the shear–stress relation simplifies in simple shearing flow between two parallel plates. The bottom plate is stationary and the top plate moves unidirectionally. Let $\hat{u}_1 = \hat{u}(\hat{y})$ and $\hat{u}_2 = 0 = \hat{u}_3$, where $\hat{x}_1 = \hat{x}$, $\hat{x}_2 = \hat{y}$ and $\hat{x}_3 = \hat{z}$. Therefore

$$\hat{e}_{ij} = \begin{bmatrix} 0 & \dfrac{\mathrm{d}\hat{u}}{\mathrm{d}\hat{y}} & 0 \\ \dfrac{\mathrm{d}\hat{u}}{\mathrm{d}\hat{y}} & 0 & 0 \\ 0 & 0 & 0 \end{bmatrix} \tag{1.4}$$

and so

$$\dot{\gamma} = \sqrt{\frac{1}{2}\left(\left(\frac{\mathrm{d}\hat{u}}{\mathrm{d}\hat{y}}\right)^2 + \left(\frac{\mathrm{d}\hat{u}}{\mathrm{d}\hat{y}}\right)^2\right)} = \left|\frac{\mathrm{d}\hat{u}}{\mathrm{d}\hat{y}}\right|. \tag{1.5}$$

From equation (1.3)

$$\hat{\tau}_{ij} = \begin{bmatrix} 0 & \hat{\mu}\dfrac{\mathrm{d}\hat{u}}{\mathrm{d}\hat{y}} & 0 \\ \hat{\mu}\dfrac{\mathrm{d}\hat{u}}{\mathrm{d}\hat{y}} & 0 & 0 \\ 0 & 0 & 0 \end{bmatrix} \tag{1.6}$$

and so

$$\hat{\tau} = \hat{\mu}\left|\frac{\mathrm{d}\hat{u}}{\mathrm{d}\hat{y}}\right|. \tag{1.7}$$

We can see that the shear stress is proportional to the shear rate.

1.2.2 Generalised Newtonian fluids

The simplest type of non-Newtonian fluid model is the generalised Newtonian model, in which the shear stress can be written as

$$\hat{\tau}_{ij} = \hat{\eta}(\dot{\gamma})\hat{e}_{ij}, \tag{1.8}$$

where $\hat{\eta}(\dot{\gamma})$ is the apparent viscosity.

The simplest non-Newtonian rheological model is the power-law model (sometimes referred to as the Ostwald-de Waele model; see Chhabra 2010). Power-law fluids are a particular type of shear-thinning or shear-thickening fluids for which $\hat{\eta} = \hat{\mu}_n \dot{\gamma}^{n-1}$ and so equation (1.8) yields

$$\hat{\tau}_{ij} = \hat{\mu}_n \dot{\gamma}^{n-1} \hat{e}_{ij}, \tag{1.9}$$

where $\hat{\mu}_n$ is the consistency parameter and n is the power-law exponent. The value $n = 1$ recovers Newtonian rheology; values $n < 1$ correspond to shear-thinning fluids; and values of $n > 1$ correspond to shear-thickening fluids.

To illustrate the power-law model we again consider simple shearing flow as for a Newtonian fluid. The shear rate $\dot{\gamma}$ is as in equation (1.5) and $\hat{\tau}_{ij}$ is given by

$$\hat{\tau}_{ij} = \begin{bmatrix} 0 & \hat{\mu}_n \left|\dfrac{\mathrm{d}\hat{u}}{\mathrm{d}\hat{y}}\right|^{n-1} \dfrac{\mathrm{d}\hat{u}}{\mathrm{d}\hat{y}} & 0 \\ \hat{\mu}_n \left|\dfrac{\mathrm{d}\hat{u}}{\mathrm{d}\hat{y}}\right|^{n-1} \dfrac{\mathrm{d}\hat{u}}{\mathrm{d}\hat{y}} & 0 & 0 \\ 0 & 0 & 0 \end{bmatrix}. \tag{1.10}$$

Therefore $\hat{\tau}$ is given by

$$\hat{\tau} = \hat{\mu}_n \left| \frac{\mathrm{d}\hat{u}}{\mathrm{d}\hat{y}} \right|^n, \tag{1.11}$$

and $n = 1$ reduces equation (1.11) to the Newtonian case, equation (1.7). As the shear rate increases so too does the shear stress. However, the effective viscosity (the ratio of shear stress to shear rate) may increase with increasing shear (for $n > 1$) or decrease (for $n < 1$).

There are other generalised Newtonian models, for example, the Carreau model and the Cross model (Barnes 1997), but we will only be concerned with the power-law model.

1.2.3 Viscoplastic fluids

Viscoplastic fluids usually obey the generalised Newtonian model when $\hat{\tau} > \hat{\tau}_y$, i.e. when the stress exceeds the yield stress $\hat{\tau}_y$. A popular model for capturing the yield stress and shear-thinning or -thickening behaviour is the Herschel-Bulkley model (Balmforth and Craster 2001),

$$\hat{\tau}_{ij} = \left(\hat{\mu}_n \dot{\gamma}^{n-1} + \frac{\hat{\tau}_y}{\dot{\gamma}} \right) \hat{e}_{ij} \quad \text{for} \quad \hat{\tau} \geq \hat{\tau}_y. \tag{1.12}$$

A simple version of this, $n = 1$, is the Bingham model,

$$\hat{\tau}_{ij} = \left(\hat{\mu}_n + \frac{\hat{\tau}_y}{\dot{\gamma}} \right) \hat{e}_{ij} \quad \text{for} \quad \hat{\tau} \geq \hat{\tau}_y. \tag{1.13}$$

In both cases $\hat{e}_{ij} = 0$ for $\hat{\tau} < \hat{\tau}_y$.

1.2.4 Viscoelastic fluids

The generalised Newtonian model does not capture elastic behaviour, and so cannot be used to model viscoelastic fluids. The simplest viscoelastic model is

the Maxwell model. Fluids which behave according to the equation

$$\hat{\tau}_{ij} + \hat{\zeta}\frac{\partial \hat{\tau}_{ij}}{\partial \hat{t}} = \hat{\mu}\hat{e}_{ij} \tag{1.14}$$

are known as Maxwell fluids, where $\hat{\zeta}$ is the relaxation time (Joseph 1990). Although the Maxwell model can be used in many circumstances, the main drawback is that the model is not frame-indifferent. This means that if the coordinates change to a moving frame then the equations change, which should not happen with material behaviour. A number of generalised frame-indifferent Maxwell models have been constructed, which involve replacing the time derivatives in (1.14) with more complicated operators (Balmforth and Craster 2001). The time derivatives can be replaced with the upper-convective derivatives (upper-convected Maxwell model, UCM), lower-convective derivatives (lower-convected Maxwell model, LCM), corotational rate (corotational Maxwell model, COM) or the interpolated convected time derivative (interpolated Maxwell model) (Joseph 1990).

1.2.5 Thixotropic and antithixotropic fluids

Recall that thixotropic and antithixotropic fluids display finite-time responses to changes in shear. The ratio of the response time to the time over which flow evolves is called the Deborah number (Barnes, Hutton, and Walters 1989, §1. 4). In principle, any fluid might be thixotropic or antithixotropic, but these effects are only important if the Deborah number is not negligibly small.

The most popular approach to describe the dynamics of thixotropic and antithixotropic fluids, introduced by Moore (1959) , is to characterise the local state of the structure by a single scalar parameter, λ, governed by an appropriate evolution equation. In some models (for example, those used by Fredrickson

(1970) and Pritchard and Pearson (2006)) the structure parameter is identified directly with a rheological quantity such as the fluidity; in others it remains an additional variable.

The simplest structure parameter model for thixotropic and antithixotropic fluids is the modified generalised Newtonian model in which $\hat{\eta}$ depends on λ,

$$\hat{\tau}_{ij} = \hat{\eta}(\dot{\gamma}, \lambda)\hat{e}_{ij}. \tag{1.15}$$

The structure parameter λ is dimensionless and is usually defined so that it takes values between zero (a fully unstructured fluid) and one (a fully structured fluid). Structural models remain essentially phenomenological, and many variations are in use.

A recent review by Mewis and Wagner (2009) described a general structural model for thixotropic and antithixotropic fluids, of which some of the models used in the papers discussed in section 1.3 are special cases. Their general model comprises an evolution equation for the scalar structure parameter λ together with a constitutive relation giving the shear stress tensor $\hat{\tau}_{ij}$ in terms of the shear rate tensor $\hat{e}_{ij}$ and the local value of λ. The structure equation is

$$\frac{\mathrm{D}\lambda}{\mathrm{D}\hat{t}} = -\hat{k}_1\dot{\gamma}^a\lambda^b + \hat{k}_2\dot{\gamma}^c(1-\lambda)^d, \tag{1.16}$$

where $\hat{k}_1$ and $\hat{k}_2$ are the rate constants for structural breakdown and build-up respectively and $\dot{\gamma}$ is the total shear rate which is related to the shear rate tensor $\hat{e}_{ij}$ in the usual manner by (1.2), while a, b, c and d are non-negative dimensionless exponents. The four exponents a, b, c and d can, in principle, be chosen independently, so equation (1.16) can represent a very wide variety of behaviours. It is assumed in most modelling work that the behaviour of a fluid should be relatively insensitive to these choices, so one may choose simple values and con-

Study	Yield stress $\hat{\tau}_y(\lambda)$	Viscosity $\hat{\eta}(\lambda, \dot{\gamma})$
Moore (1959)	-	$\hat{\eta}_0 + (\hat{\eta}_\infty - \hat{\eta}_0)\lambda$
Worrall and Tuliani (1964)	$\hat{\tau}_{y,0}$	$\lambda\hat{\eta}_0$
Nguyen and Boger (1985)	$\lambda\hat{\tau}_{y,0}$	-
Toorman (1997)	$\lambda\hat{\tau}_{y,0}$	$\lambda\hat{\eta}_0$
Mujumdar *et al.* (2002)	$\lambda^{a+1}\hat{G}_0\hat{\gamma}_c^a$	$-\lambda\hat{K}_0\dot{\gamma}^{n-1}$
Coussot *et al.* (2002)	-	$\hat{\eta}_0(1+\lambda^n)$
Huynh *et al.* (2005)	-	$\hat{\eta}_0(1+\lambda^n)$
Dullaert and Mewis (2006)	$\lambda\hat{G}_0\hat{\gamma}_c(\lambda\dot{\gamma})^a$	$\lambda\hat{\eta}_0$
Liu and Zhu (2011)	$\dfrac{\hat{\eta}_0(1+\lambda^n)}{\hat{\alpha}\hat{\theta}\lambda}$	$\hat{\eta}_0(1+\lambda^n)\dot{\gamma}$
Livescu *et al.* (2011)	-	$\hat{\eta}_0 + (\hat{\eta}_\infty - \hat{\eta}_0)\lambda$
	-	$\dfrac{\hat{\eta}_0\hat{\eta}_\infty}{(\hat{\eta}_0 + \hat{\eta}_\infty - \hat{\eta}_\infty\lambda)^2}$

Table 1.1: Some relations between rheological parameters and the structure parameter, adapted from table 2 in Mewis and Wagner (2009). (In the viscosity column, $\hat{\eta}_0$ is the viscosity of the fluid when the structure is completely broken down and $\hat{\eta}_\infty$ is the viscosity of the fluid when the structure is completely built up. Definitions of various plastic and elastic terms from the yield stress column can be found in Mewis and Wagner (2009).)

centrate on determining the form of the constitutive equation. For example, the model of Coussot *et al.* (2002) corresponds to $a = 1$, $b = 1$, $c = 0$, $d = 0$; that of Billingham and Ferguson (1993), neglecting the diffusive term, corresponds to $a = 1$, $b = 1$, $c = 0$, $d = 1$. One of the contributions of the present work is to investigate different parameter choices and see the impact it has on the behaviour of the flow.

Mewis and Wagner (2009) tabulate a variety of constitutive relations, and there are many possible choices. Table 1.1 (adapted from table 2 in Mewis and Wagner (2009)) shows yield stresses and viscosities of several thixotropic models. The most popular models are based around the model by Moore (1959) or a power-law type model.

In this thesis, for convenience and to allow us to explore the possible regimes of behaviour of equation (1.16) without introducing an unmanageable number

of parameters, we use the simplest of these. This is the simplified relation due to Moore (1959) in which the effective viscosity is proportional to λ,

$$\hat{\tau}_{ij} = \hat{\eta}_0 \lambda \hat{e}_{ij}, \tag{1.17}$$

where $\hat{\eta}_0$ is a constant viscosity parameter.

An alternative approach is the model of Harris (1967). In its simplest form, the Harris model gives the viscosity as

$$\hat{\mu}(t) = \hat{\mu}_0 - \hat{K}_1 \dot{\gamma} + \hat{K}_2 \frac{\mathrm{D}\dot{\gamma}}{\mathrm{D}t}, \tag{1.18}$$

where $\hat{K}_1$ and $\hat{K}_2$ are material constants, $\hat{\mu}_0$ is the zero-shear viscosity, and $\dot{\gamma}$ is the second invariant of the deformation-rate tensor. However, this model has been found inadequate for practical purposes in recent studies (Sadeqi *et al.* 2011), so we shall not pursue it.

1.2.6 Rheometry

Rheometers are an important component of rheological research (Barnes *et al.* 1989). They are instruments used to measure how a Newtonian or non-Newtonian fluid flows in response to applied forces and to record quantities such as shear stress and shear rate. Many theoretical studies involve trying to fit solutions of governing equations to experimental data obtained from rheometers. We will describe some of the most popular rheometers.

Rotational rheometers have two parts with the fluid between them (figure 1.2). Concentric-cylinder, cone-and-plate and parallel-plate rheometers are shown in figures 1.2 a, b and c, respectively. In concentric-cylinder (also known as Couette or coaxial) rheometers, the fluid is contained between two cylinders.

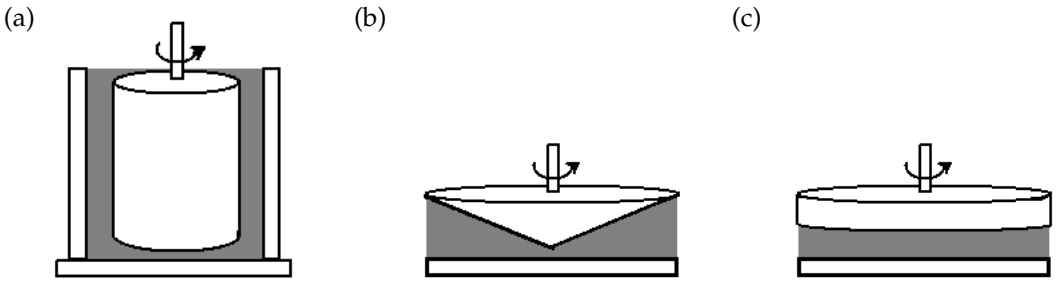

Figure 1.2: Three common types of rotational rheometers; (a) concentric-cylinder rheometer, (b) cone-and-plate rheometer and (c) parallel-plate rheometer.

The outer, inner or both cylinders rotate and the shear rate and shear stress can be measured. An advantage of using concentric-cylinder rheometers is that the shear rate is constant in space. If the inner cylinder is replaced with vane spindles it is called a vane rheometer. In cone-and-plate rheometers, the fluid is contained between an inverted rotating cone and a fixed plate. As in a concentric-cylinder rheometer, the shear rate for a fluid in a cone-and-plate rheometer is constant in space. In parallel-plate rheometers, the fluid is contained between a rotating plate and a fixed plate and the shear rate is not uniform. However there are advantages to using a parallel-plate rheometer: for example, only a small sample size is needed, and they are also easy to clean.

Capillary rheometers are different from rotational rheometers: the fluid sample is forced through the capillary die (tube) with either the shear rate or the shear stress fixed and the other measured. Capillary rheometers are important as they are the only type of rheometer which can investigate die swell and melt fracture. Die swell occurs when a fluid is squeezed through the die and "swells" on exit before returning to its former shape (Phan-Thien 2002). Melt fracture is

when the surface of the fluid is distorted when leaving the die; the effect can range from minor ripples to severe distortion (Whelan 1994).

A standard form in which to present rheometric data is a plot of the shear stress against the shear rate in the rheometer, often called a rheogram. Rheograms help to identify key features of the fluid. For a Newtonian fluid the relationship between the shear rate and shear stress is linear, but this is generally not the case for non-Newtonian fluids which we will consider in later chapters. In particular, for thixotropic fluids a hysteresis loop develops as the stress lags behind the shear rate (Mewis and Wagner 2009).

1.3 Previous modelling work on thixotropic fluids

Thixotropic effects were first described by Schalek and Szegvari (1923) in iron oxide dispersions and the first paper using the term "thixotropy" was published four years later by Péterfi (1927). The word "thixotropy" comes from a combination of the Greek words "thixis" (meaning stirring or shaking) and "trope" (meaning turning or changing) (Mewis and Wagner 2009). In this section we will not attempt a comprehensive review of ninety years of research, but will concentrate on work from the last two decades.

As mentioned previously, some authors have chosen to include viscoplastic and viscoelastic terms in their models for thixotropic fluids, usually in order to model specific fluids, but many choose not to. Accordingly, in the next three sections we consider viscoplastic thixotropic fluids, viscoelastic thixotropic fluids and purely thixotropic fluids.

1.3.1 Viscoplastic thixotropic fluids

Billingham and Ferguson (1993) studied pipe flow of a thixotropic fluid with a yield stress, specifically bentonite mud. They used a rheological model with a structure parameter like that described in section 1.2, but with the addition of a diffusive term in the structure equation, to investigate both start-up and steady-state problems. They also plotted and discussed rheograms as described in section 1.2.6.

Coussot *et al.* (2002) looked at avalanche behaviour in yield-stress fluids and performed physical experiments on inclined planes. An avalanche occurs when spatially uniform flow down an inclined plane cannot remain steady and accelerates in time, due to runaway feedback between the breakdown of structure and the speed of flow. The authors carried out physical experiments using parallel-plate and vane rheometers for a gel, a colloidal glass and a bentonite mud. All three fluids obey the general rheological model presented by the authors. A follow-up study by Huynh *et al.* (2005) built on the work by Coussot *et al.* (2002). The authors concentrated on the flow of a thin layer of thixotropic fluid down an inclined plane. They investigated both the critical time at which the avalanche begins and the conditions for a thin layer of fluid to start flowing down the plane. They compared the results of their theory with experimental data. We will consider thin-film flow of thixotropic and antithixotropic fluids in more detail in section 1.5.

Liu and Zhu (2011) also investigated flow down an inclined plane, and examined avalanche flow theoretically, building on the work by Coussot *et al.* (2002). They were mainly interested in the start-up problem and considered three cases: when the flow before the avalanche was not noticeable; when the flow before the avalanche was noticeable; and when there was no avalanche flow. The flow before the avalanche was noticeable if the apparent viscosity

of the fluid was initially small and not noticeable if it was initially large. In certain limits, the results for no noticeable flow before the avalanche and for no avalanche flow agreed with Huynh *et al.* (2005). When the flow before the avalanche was noticeable, the velocity profiles changed from Newtonian before to Bingham after the avalanche as shear-thinning effects became apparent.

Chanson *et al.* (2006) modelled bentonite mud as a thixotropic fluid with a yield stress. They were the first to conduct a systematic study of the so called dam-break problem for a thixotropic fluid, that is when fluid is suddenly released and flows along a surface, in this case an inclined plane. The authors used the model described by Coussot *et al.* (2002), whose predictions they successfully compared to experimental data from a parallel-plate rheometer. They found different regimes of dam-break behaviour depending on the properties of the fluid and the flow conditions. Potanin (2010) attempted to bridge the gap between rheological and computational fluid dynamics (CFD) communities. He experimented with three pastes in two rheometers (Couette and vane-cup geometries) and looked at both the break down and build up of the pastes. The CFD predictions of the model with appropriate rheology incorporated compared favourably with the experimental data.

A well-known everyday fluid which displays yield stress properties is toothpaste, and Ardakani *et al.* (2011) investigated the thixotropic flow of toothpaste. They chose the parameters for their model, taken from Derksen and Prashant (2009), based on experimental data from a capillary rheometer. They investigated how the structure parameter behaves at various apparent shear rates. They compared the predictions of their structure parameter model with the experimental data and the differences in the results were attributed to elastic properties which may also be present in toothpaste.

Work is still ongoing regarding viscoplastic fluid flows, and very recently a

special issue of the *Journal of Non-Newtonian Fluid Mechanics* was wholly concerned with viscoplastic fluids (see Balmforth and de Bruyn 2013).

1.3.2 Viscoelastic thixotropic fluids

Some authors include viscoelastic effects in their models for thixotropic fluids. Motivated by pulsatile blood flow, Shadrina (1978) developed solutions for weak oscillations superimposed on a steady background flow of a viscoelastic thixotropic fluid. The presence of a background flow makes this significantly different from the classical Stokes problem, which we will discuss in section 1.4. We will return to both channel flow and oscillating walls when we consider the Stokes problem and slowly-varying channel flow in chapters 2, 3 and 4, respectively.

Bautista *et al.* (1999) considered the steady and unsteady flow of viscoelastic micellar solutions and liquid crystals, focusing on the thixotropic and anti-thixotropic behaviour. They used the upper-convected Maxwell constitutive equation (mentioned in section 1.2) and a kinetic equation first proposed by Fredrickson (1970). They considered steady simple shear flow and also stress relaxation after a step change in the stress or shear rate. Finally, they studied stress cycles by gradually increasing and decreasing the shear stress and plotting the shear viscosity against shear rate (compare the rheograms described in section 1.2.6).

Corvisier *et al.* (2001) conducted a pipe flow experiment in which fluid flowed from a large tank. They used two viscoelastic fluids, veegum and laponite colloidal suspensions, and concentrated on flow development. The authors compared two measuring techniques, ultrasonic velocity profiling (UVP) and particle image velocimetry (PIV), both chosen because the velocity profile can be measured nearly instantaneously. As the fluid flowed down the pipe the veloc-

ity profiles flattened in the centre, where the lower shear caused the structure of the fluid to build up leading to a plug region developing.

Mujumdar *et al.* (2002) developed a new model to describe viscoelastic thixotropic fluids and used it to examine various flow problems. They compared the predictions of their model to experimental data for ceramic suspensions. Their model was designed to capture the smooth transition from elastic to viscous behaviour, rather than considering purely elastic and purely viscous behaviour separately. The authors considered the start-up of steady shear flow, stress relaxation after the forcing has stopped, and oscillatory shear flow.

More recently, de Souza Mendes (2009) built a new model to describe viscoelastic thixotropic behaviour. De Souza Mendes (2009) pointed out that many authors make *ad hoc* assumptions purely to simplify their models, rather than using physical arguments. The predictions of their new model, adapted from the well-known Maxwell model, described in section 1.2.4, was successfully compared to various rheometric flows. The key difference between the Maxwell model and the new model is that the shear modulus and structural viscosity in the new model depend on the structure parameter (see section 1.2.5). A simplified, inelastic version of this model was recently considered by de Souza Mendes *et al.* (2012).

Some rheological models for thixotropic fluids include both viscoplastic and viscoelastic properties, called elasto-viscoplastic fluids. A recent overview by de Souza Mendes and Thomson (2012) considered two types of models; a viscoplastic model with elastic properties (Type I) and a viscoelastic model with a yield stress (Type II). The Type II models can describe thixotropic and elastic effects. The authors discussed two Type I models, modified from the models proposed by Mujumdar *et al.* (2002) and Dullaert and Mewis (2006). They constructed a Type II model by adding yield stress to the viscoelastic model

proposed by de Souza Mendes (2009). These types of model were compared and the framework of Type II models was found to be more robust. One reason is that, in general, the Type II models could easily be adapted to describe many materials including inelastic thixotropic viscoplastic materials, viscoelastic solids and fluids; another was that, unlike Type I models, Type II models were consistent with the classical definition of yield stress.

1.3.3 Purely thixotropic fluids

The model we will use in the present work is for purely thixotropic fluids, and therefore includes no yield stress or viscoelastic terms. Accordingly we will discuss some papers which also neglect elastic and plastic effects and concentrate on purely thixotropic effects. It appears to be only in recent years that purely thixotropic fluids have been considered. Our work therefore contributes to this recent interest in isolating the effects of thixotropy from those of plasticity and elasticity.

Pearson and Tardy (2002) examined the interactions between complex fluids and porous media. According to the authors, there was little agreement on how to model complex fluids (including thixotropic fluids) in porous medium. Investigating channel flow is the first step to investigating flow in a porous medium, and we will consider slowly-varying channel flow for thixotropic and antithixotropic fluids in chapter 4. Pritchard and Pearson (2006) investigated a purely thixotropic fluid in a porous medium or a narrow fracture, using a modified version of the model used by Bautista *et al.* (1999) together with a "gap-averaged" structure parameter; the latter will be discussed in section 1.5.

Derksen and Prashant (2009) looked at the flow of purely viscous thixotropic fluids. They considered simple shear flow, plane Poiseuille flow, and lid-driven cavity flow. All flows started with a Newtonian fluid, with the structure param-

eter set to zero, then the thixotropic rheology was "switched on" and velocity and structure parameter profiles evolved. Finally, the authors investigated thixotropic fluids in mixing tanks and calculated snapshots, i.e. profiles at various times, of the velocity and structure parameter.

Najmi *et al.* (2010) presented a numerical study of pressure-driven thixotropic fluid flow above a fixed plate, using the rheological model described by Harris (1967) (see section 1.2.5). Sadeqi *et al.* (2011) investigated thixotropic fluids above a fixed semi-infinite plate (Blasius flow) also using a simplified Harris model.

Livescu *et al.* (2011) addressed the levelling under gravity of thixotropic fluids on a horizontal substrate. They compared two rheological models, one of which was chosen for simplicity and one to try to capture more complex behaviour, and these models will be discussed in more detail in section 1.5.

Although there has been much work done concerning thixotropic fluids, the literature is still lacking in many areas. Huynh *et al.* (2005) point out that there is a lack of studies of thixotropic fluids in many practical situations, including free-surface flows. Mewis and Wagner (2009) and de Souza Mendes (2009) argue that an accurate general model for thixotropy is still lacking. Najmi *et al.* (2010), Sadeqi *et al.* (2011) and Chekila *et al.* (2011) all agree that much work still needs to be done on the flow of thixotropic fluids. This is perhaps why some basic flow problems, including those considered in later chapters, have yet to be considered for these complex fluids.

1.4 The Stokes problem

One of the most basic problems long solved for a Newtonian fluid, but yet to be solved for more complex fluids, is the Stokes problem (Stokes 1851). In the

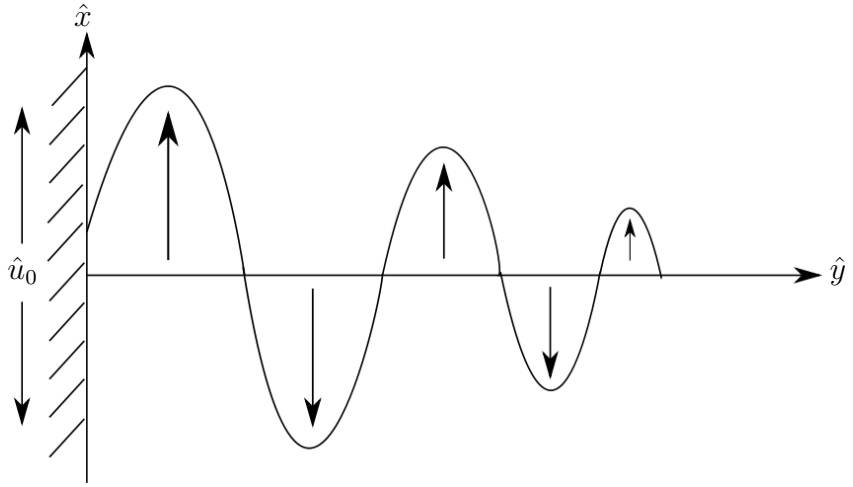

Figure 1.3: A semi-infinite fluid with a sinusoidally oscillating wall at $\hat{y} = 0$.

Stokes problem the shear varies in both time and space; it is one of the simplest non-trivial rectilinear flows in which both viscosity and inertia are important.

In the classical Stokes problem (also known as Stokes' second problem), a Newtonian fluid of constant kinematic viscosity $\hat{\nu}$ occupies a semi-infinite space $\hat{y} > 0$ bounded by a rigid impermeable wall at $\hat{y} = 0$ as seen in figure 1.3. This wall is oscillated sinusoidally so that the $\hat{x}$-velocity on the wall is given by $\hat{u}(0, \hat{t}) = \hat{u}_0 \cos(\hat{\omega}\hat{t})$, where $\hat{\omega}$ is the angular frequency of the oscillations, $\hat{t}$ is time and $\hat{u}_0$ is the magnitude of the oscillations. This unsteady flow is governed by momentum equation

$$\frac{\partial \hat{u}}{\partial \hat{t}} = \hat{\nu} \frac{\partial^2 \hat{u}}{\partial \hat{y}^2}, \tag{1.19}$$

with boundary and far-field conditions

$$\hat{u}(0, t) = \hat{u}_0 \cos(\hat{\omega}\hat{t}) \qquad \text{and} \qquad \hat{u}(\hat{y}, \hat{t}) \to 0 \quad \text{as} \quad \hat{y} \to \infty. \tag{1.20}$$

The exact solution is given (see, e.g., Drazin and Riley 2006, §4. 1) by

$$\hat{u}(\hat{y}, \hat{t}) = \hat{u}_0 \mathrm{e}^{-\hat{\gamma}\hat{y}} \cos(\hat{\omega}\hat{t} - \hat{\gamma}\hat{y}), \quad \text{where} \quad \hat{\gamma} = \sqrt{\frac{\hat{\omega}}{2\hat{\nu}}}. \tag{1.21}$$

This structure is sometimes referred to as an oscillatory boundary layer or "Stokes layer". It may be visualised as a sinusoidal travelling wave propagating into the fluid at speed $\hat{\omega}/\hat{\gamma}$ and decaying according to an exponential "envelope" with characteristic thickness $1/\hat{\gamma}$, although the dynamics are diffusive rather than wavelike.

When examining the Stokes problem, both the start-up and the periodic states can be investigated. We will be mainly interested in the periodic solutions, but there has also been work focusing on the start-up problem. For example, Ai and Vafai (2005) solved the Stokes problem numerically for generalised Newtonian rheologies, emphasising the transient adjustment from a quiescent to a periodic state; Fetecau and Fetecau (2005), in a study later corrected by Christov and Jordan (2012), examined the start-up problem for a class of second-grade fluids.

The Stokes problem is non-rheometric, because the shear varies in both time and space; it is one of the simplest non-trivial rectilinear flows in which both viscosity and inertia are important. Because the oscillation imposes a timescale on the system, the problem becomes particularly interesting when the fluid rheology is time-dependent, and its natural timescale may or may not coincide with that of the forcing. This offers opportunities to use the Stokes problem as an unconventional but revealing test for rheological models, as proposed by Balmforth *et al.* (2009). (Such a test should not be confused with the standard oscillatory shear tests used to characterise viscoelastic fluids with and without thixotropy (Mewis and Wagner 2009, §5.4), as these remain non-inertial and rheometric.)

A final motivation for studying the Stokes problems is that it provides a useful prototype for more complex flows with oscillatory forcing, such as the boundary layer beneath water waves (Lighthill 1978, §2.7). In muddy environ-

ments, water waves may propagate over shallow layers of non-Newtonian fluid mud (McAnally *et al.* 2007), and to predict the transport of mud it is important to understand how such layers respond to oscillatory forcing.

A few recent studies have investigated the Stokes problem for generalised Newtonian rheologies, including Balmforth *et al.* (2009) who conducted a detailed numerical investigation of the finite-depth Stokes problem for a viscoplastic Herschel–Bulkley fluid, and compared their results with experiments using a kaolin slurry. They suggested that some discrepancies between the numerical and experimental results might be due to thixotropic effects.

There has also been theoretical work on viscoelastic generalisations of the Stokes problem, although there is as yet no corresponding body of experimental work. In particular, analytical and approximate solutions have been presented for the second- and third-grade fluid models (Rajagopal 1982; Rajagopal and Na 1983), the Johnson–Segalman model (Hayat *et al.* 2004) and the Burgers model (Khan *et al.* 2010). Although the decay envelopes and wave propagation speeds in these solutions are somewhat modified from the Newtonian case (1.21), they do not possess qualitatively different features. There is no systematic tendency for time-dependence to increase or decrease the rate of decay of the "envelope": indeed, both Rajagopal (1982) and Khan *et al.* (2010) found that either could occur depending on the precise model used and the ratio of the elastic relaxation and forcing timescales.

1.5 Thin-film flow

Thin films of fluid appear in many diverse settings such as geophysics, biology and engineering. In geophysics, lava flowing over rocks and landslides are examples of thin-film flow. Thin films of fluid appear in biology in the tear film

(a) (b)

Figure 1.4: (a) Honey on toast, with kind permission from Erica Lea (see http://www.flickr.com/photos/elberge/5556037139/). (b) Oil in a frying pan, with kind permission from Sarah Twichell (see http://www.flickr.com/photos/38015815@N00/4343472355/).

coating the eye, known as the precorneal film, and as the thin films of synovial fluid in human joints. In engineering, thin films are found in many mechanical devices such as in the gears and pistons of car engines. Thin films of fluid can also be found in everyday life such as oil in a pan, honey on toast (see figure 1.4), icing on cakes and paint on walls.

It is important to understand that we do not use "thin" in the everyday sense, i.e. of shallow depth, but we use it to mean that the thickness of the fluid is much less than the length scale of the flow. Essentially equivalent terms include "shallow", "slender" and "slowly varying". A related term, "lubrication flow", is generally taken to imply that the flow is both thin and non-inertial. This separation of lengthscales allows the reduction of the governing equations to a simpler form, typically by an asymptotic expansion in the aspect ratio (the ratio of the cross-flow to the streamwise length-scale). We will demonstrate this in section 4.2.

1.5.1 Newtonian and generalised-Newtonian fluids

Thin-film flows have been extensively researched for Newtonian fluids but much less so for non-Newtonian fluids, in particular thixotropic and antithixotropic fluids. Therefore, as we shall see, even some of the most basic thin-film flow problems remain unsolved for complex fluids.

Two major reviews on thin-film flows are those by Oron *et al.* (1997) and Craster and Matar (2009). The review by Oron *et al.* (1997) considers many thin-film problems, including bounded films, spreading and free films. The authors determined a general evolution equation and showed that the general equation could be adapted for many different bounded film problems, including flow on a rotating disk and flow on a horizontal cylinder. They also considered falling films and sheets flowing down an inclined plane. These problems were outlined to demonstrate the large numbers of flow geometries which could be considered. The more recent review by Craster and Matar (2009) considered the dynamics and stability of thin liquid films and mainly concentrated on the progress made since the review by Oron *et al.* (1997). They described many problems including flows driven by gravity and other forces and the effects of bounding walls. One such problem was a bilayer of fluid flowing downslope and another was the interplay between a thin-film of fluid and an electric field. They showed that there has been much research in recent years on thin-film problems, however there are still many open problems to consider. Although both reviews are extensive, neither discusses non-Newtonian flows.

While relatively little has been done on complex fluids, there have been some interesting studies regarding thin films of power-law fluids, including Wilson and Burgess (1998), Wilson, Duffy, and Hunt (2002) and Yatim *et al.* (2010). All these studies consider the flow of rivulets of power-law fluids down a substrate. Wilson and Burgess (1998) found self-similar solutions to the steady flow of a

rivulet of a power-law fluid as a special case of the Herschel-Bulkley model (section 1.2.3). Wilson, Duffy, and Hunt (2002) extended and generalised this work and considered gravity-driven and shear-stress-driven rivulets of power-law fluid down an inclined plane. They found that the fluid behaved qualitatively similarly for both gravity and shear-stress-driven flow. Yatim *et al.* (2010) found solutions to the unsteady flow of rivulets of a power-law fluid. In particular, the authors considered the behaviour of the fluid in the highly shear-thinning limit, as $n \to 0^+$, and in the highly shear-thickening limit, as $n \to \infty$, and found the asymptotic solutions in both cases. In chapter 4 we will consider the highly shear-thickening limit ($n \to \infty$).

Thin-layer theory for viscoplastic fluids was first put on a rigorous basis by Balmforth and Craster (1999), and there has been subsequent work on such problems. For example, Ross *et al.* (2001) considered the two-dimensional flow of a thin film of viscoplastic material around a stationary or rotating cylinder. They started with a biviscosity fluid and considered both when the ratio of the viscosities was of order one and when it is set to zero. The asymptotic solutions in the thin-film limit revealed interesting behaviour of the fluid for both stationary and rotating cylinders. The same authors continued their investigation of thin films of viscoplastic fluids by considering a rivulet of viscoplastic fluid draining around a large cylinder (Wilson, Duffy, and Ross 2002). They again used the biviscosity model. A very interesting result was obtained in the special case when the viscosity limit approached zero, namely that the edges of the rivulet became solid and the top of the rivulet became nearly solid, but the fluid adjacent to the cylinder continued to flow.

Myers (2005) considered thin-film flow both for free surface flow and channel flow using the power-law, Carreau and Ellis models. He compared the velocity and viscosity profiles of different fluids both down an inclined plane and

in a channel (compare chapter 4, where we consider channel flow for a thixotropic or antithixotropic fluid). The main objective of the paper was to consider an alternative to the power-law model at low shear rates where the rheological model breaks down (see section 4.4.3).

Another group of studies to consider is thermal problems, that is problems in which temperature can affect the properties of a fluid. The reviews by Oron *et al.* (1997) and Craster and Matar (2009) both consider problems involving thermal effects. Recently, Leslie *et al.* (2011) considered a thin film of Newtonian fluid with temperature-dependent viscosity on a cylinder, for which the cylinder was either hotter or colder than the surrounding atmosphere. They examined the limit of large and small thermoviscosity number (strong or weak variation of viscosity with temperature) and they also examined the case when the viscosity was constant. A loose analogy can be drawn with thixotropic models in which the the structure parameter (see section 1.2.5) controls the viscosity. However, the transport of heat is dominated by diffusion, unlike that of the structure parameter which is generally taken to be advective. In chapter 4 we will see that thin-film models of thixotropic effects are therefore more complicated than those of thermal effects.

1.5.2 Thixotropic and antithixotropic fluids

There is far less published work on thin-film and shallow flows of thixotropic and antithixotropic fluids than on generalised Newtonian fluids. In particular, no systematic framework has been presented for these fluids which is equivalent to the lubrication theories for generalised Newtonian fluids reviewed above. Nevertheless, several studies have considered thin-film flows for thixotropic fluids under various simplifying assumptions, and it is useful to review these here.

The most strongly reduced models are of the kind presented by Coussot *et al.* (2002). The problem considered here was the acceleration of a uniform layer of fluid on an inclined plane. This is intrinsically a one-dimensional problem, since the velocity and structure parameter may be expected to vary across the thickness of the layer. The original model by Coussot *et al.* (2002) reduces this one-dimensional problem further to a "zero-dimensional" problem by describing the flow entirely in terms of a layer-averaged streamwise velocity and a layer-averaged structure parameter. The advantage of the zero-dimensional problem is that the dynamics can be described by ordinary differential equations. Subsequent work on this problem (Huynh *et al.* 2005; Liu and Zhu 2011) does incorporate the variation of the flow variables across the layer; since the flow is still assumed to be uniform in the streamwise direction, their model represents a limiting case of the thin-film regime. (Earlier work, for example that by Billingham and Ferguson (1993), had also explicitly considered the time-evolution of flows which were uniform in the streamwise direction.)

In rather different geometries, Chanson *et al.* (2006) and Pritchard and Pearson (2006) both presented models of shallow thixotropic flow which relied on the same *ad hoc* reduction of the equations. Chanson *et al.* (2006) considered dam-break flow on an inclined plane, while Pritchard and Pearson (2006) considered flow in a narrow fracture, taken to be equivalent to Darcy flow in a porous medium (for which the correct formulation of the governing equations is not clear: see Pearson and Tardy (2002)). Both studies reduced the governing equations on the basis that the rheological state of the fluid was uniform across the layer, so Chanson *et al.* (2006) employed a "vertically averaged" value of the structure parameter λ, while Pritchard and Pearson (2006) employed a "cross-sectionally averaged" value of the fluidity in a version of Bautista *et al.*'s (1999) model. Under such assumptions there is no need to resolve the flow structure

across the layer, and so the system becomes one- or two-dimensional, with only variations in the streamwise direction(s) considered.

The most sophisticated treatment so far of shallow thixotropic flow is that presented by Livescu *et al.* (2011) (which we mentioned briefly in section 1.3.3), who considered the levelling of a thin film of thixotropic fluid on a level substrate. They reduced the governing hydrodynamic equations using a lubrication approximation, which we will employ in chapter 4, but without making further assumptions about the variation of λ across the layer. The resulting system, including a vertically-resolved evolution equation for λ, was integrated numerically for the levelling problem under consideration. On the basis of these simulations, approximations for the vertical variation of λ were suggested, which allowed the evolution of the structure to be described solely in terms of the evolution of the values of λ at the surface and at the substrate. In a further stage of simplification, the resulting one-dimensional system was linearised assuming that the perturbations to the horizontal free surface were small, and the linearised results for the reduced system were found to agree well with the numerical calculations.

The approach by Livescu *et al.* (2011) is an advance on that of Chanson *et al.* (2006) and Pritchard and Pearson (2006), because they do not postulate in advance that the cross-stream variation of the structure is known. However, the weakness of this approach is that this variation must be obtained by numerical simulations of a non-reduced system, and there is no guarantee that the approximate profiles for λ obtained in this way will be equally applicable to different problems. With this in mind, our goal in chapter 4 will be to develop a systematic thin-film reduction of the governing equations for thixotropic and antithixotropic fluids in a slender geometry.

1.6 Outline of thesis

In this thesis we study two different fundamental problems involving the flow of thixotropic, antithixotropic and power-law fluids. Even our relatively simple model for thixotropy reveals unexpectedly complicated solutions to these problems. These solutions provide a good foundation for understanding the flow of time-dependent fluids.

In chapter 2 we investigate the Stokes problem for a power-law fluid with power-law exponent n. We obtain semi-analytical, self-similar solutions for various values of n. We demonstrate numerically that these solutions provide a good approximation to the flow driven by a sinusoidally oscillating wall.

In chapter 3 we investigate the Stokes problem for a thixotropic or antithixotropic fluid. We obtain asymptotic and numerical solutions in the limit of small-amplitude oscillations for both the velocity and the structure parameter. The model displays qualitatively different behaviour depending on the choice of parameters in our general model seen in section 1.2.5. Both thixotropic and antithixotropic fluids display fast-adjusting, slow-adjusting and marginal behaviours depending on the response time for the structure compared with the timescale over which the shear rate changes. The fast-adjusting behaviour in the antithixotropic case corresponds to the behaviour of a power-law fluid as analysed in chapter 2. We also present numerical solutions for large-amplitude oscillations.

In chapter 4 we consider flow of a thixotropic or antithixotropic fluid in a slowly-varying channel. We formulate a perturbation approach in which thixotropic effects enter at first order in the thin-film limit. We then develop asymptotic solutions to leading and first order for the velocity and the structure parameter of the fluid for a special case ($d = 0$).

Finally, in chapter 5 we summarise and discuss the key results obtained in

chapters 2 to 4. We also suggest directions for interesting further work.

1.7 Presentations and publications

Aspects of the work contained in chapter 2 have been presented at the British Applied Mathematics Colloquium at the University of Birmingham in April 2011 and at the Scottish Fluid Mechanics Meeting at the University of Strathclyde in May 2011. My supervisor also presented the work at Princeton University in June 2011 and at the American Physical Society's Division of Fluid Dynamics meeting in Baltimore in November 2011. This work has been published by the Journal of Non-Newtonian Fluid Mechanics (Pritchard *et al.* 2011).

Aspects of the work contained in chapter 3 have been presented at the British Applied Mathematics Colloquium at University College London in March 2012; at the Scottish Fluid Mechanics Meeting at Heriot-Watt University in May 2012; and at the XVIth International Conference on Rheology in Lisbon in August 2012. This work has been published by the Journal of Non-Newtonian Fluid Mechanics (McArdle *et al.* 2012).

Aspects of the work contained in chapter 4 have been presented at the Scottish Fluid Mechanics Meeting at the University of Aberdeen in May 2013, and are currently being prepared for publication.

Chapter 2

The Stokes problem for a power-law fluid

2.1 Introduction

In this chapter, we will employ a combined analytical and numerical approach to explore the structure of the Stokes boundary layer (introduced in section 1.4, see figure 1.3) for a power-law fluid. In section 2.2 we will formulate the problem for a power-law fluid and present semi-analytical, self-similar solutions for the velocity, in which the amplitude envelope and the variation of the phase of the oscillation with $\hat{y}$ are analytically determined while the waveform of the oscillation is obtained as the solution of an ordinary differential equation. In section 2.3 we will compare these solutions with numerical solutions of the governing partial differential equation. Finally, in section 2.5 we will discuss the key features of these solutions and their more general significance. In chapter 3 we will see that these solutions provide a limiting case of the antithixotropic version of the problem.

2.2 Semi-analytical solutions

2.2.1 Problem formulation

In the power-law rheological model the shear stress component $\hat{\tau}_{xy}$ in a simple shear flow of the kind described in section 1.4 is given by

$$\hat{\tau}_{xy} = \hat{\mu}_n \left| \frac{\partial \hat{u}}{\partial \hat{y}} \right|^{n-1} \frac{\partial \hat{u}}{\partial \hat{y}}. \tag{2.1}$$

Here $\hat{u}(\hat{y}, \hat{t})$ is the velocity in the $\hat{x}$-direction, parallel to the wall; $\hat{y}$ measures distance from the wall; $\hat{\mu}_n$ is a dimensional consistency parameter; and $n > 0$ is the power-law exponent. The value $n = 1$ recovers Newtonian rheology; values of $n < 1$ correspond to shear-thinning fluids, such as many colloidal dispersions, in which the effective viscosity decreases with increasing shear; and values of $n > 1$ correspond to shear-thickening fluids, such as some polymer solutions, in which the effective viscosity increases with increasing shear. The momentum equation (1.1), reduced for unsteady rectilinear flow, thus becomes a non-linear diffusion equation with the effective viscosity of the fluid acting as a momentum diffusivity,

$$\hat{\rho} \frac{\partial \hat{u}}{\partial \hat{t}} = \hat{\mu}_n \frac{\partial}{\partial \hat{y}} \left(\left| \frac{\partial \hat{u}}{\partial \hat{y}} \right|^{n-1} \frac{\partial \hat{u}}{\partial \hat{y}} \right), \tag{2.2}$$

where $\hat{\rho}$ is the fluid density.

It is assumed that the solutions are periodic with angular frequency $\hat{\omega}$, and that some characteristic amplitude $\hat{U}$ may be defined. In the numerical results presented in section 2.3, the no-slip boundary condition $\hat{u}(0, \hat{t}) = \hat{U} \cos(\hat{\omega} \hat{t})$ will be imposed at the oscillating wall, defining $\hat{U}$ directly. In our self-similar solutions we do not prescribe such a boundary condition, but we will assume that

an appropriate value of $\hat{U}$ can still be specified. This will be discussed further below.

Finally, we will require that the velocity decays to zero at large distances from the wall, $\hat{u}(\hat{y},\hat{t}) \to 0$ as $\hat{y} \to \infty$.

The problem may now be non-dimensionalised by setting

$$t = \hat{\omega}\hat{t}, \qquad y = \left(\frac{\hat{\omega}\hat{\rho}}{\hat{\mu}_n \hat{U}^{n-1}}\right)^{1/(n+1)} \hat{y} \qquad \text{and} \qquad u = \frac{\hat{u}}{\hat{U}}. \tag{2.3}$$

2.2.2 Constructing self-similar solutions

It is helpful in what follows to note that the governing equation (2.2) remains unchanged under the transformation $y \mapsto y_0 \pm y$ for any constant offset y_0. We will therefore define a new variable $Y = y_0 \pm y$ and write (2.2) as

$$\frac{\partial u}{\partial t} = \frac{\partial}{\partial Y}\left(\left|\frac{\partial u}{\partial Y}\right|^{n-1}\frac{\partial u}{\partial Y}\right). \tag{2.4}$$

If we take $Y = y_0 + y$ then the far-field boundary condition becomes $u \to 0$ as $Y \to \infty$. If we take $Y = y_0 - y$ then we must either consider solutions that are valid for negative values of Y or restrict the domain of the solution to $Y \geq 0$, (i.e. $0 \leq y \leq y_0$) and impose the condition $u = 0$ for all $y \geq y_0$. Below we will invariably follow the latter approach, so $Y \geq 0$ implicitly throughout.

Motivated by the Newtonian solution (1.21), we will seek a solution of the self-similar form

$$u(Y,t) = Y^{\alpha} f(\eta) \tag{2.5}$$

where $\eta = t - \phi(Y)$ for some function $\phi(Y)$. Note that for both definitions of Y we can interpret the offset y_0 as a boundary-layer thickness. If $Y = y_0 - y$ then y_0 represents the thickness of the (finite) layer of non-zero velocity, whereas if $Y = y_0 + y$ then y_0 characterises the distance from the wall beyond which the

algebraic decay in y asserts itself.

From (2.5) we immediately obtain

$$\frac{\partial u}{\partial t} = Y^\alpha \frac{\mathrm{d}f}{\mathrm{d}\eta} \qquad \text{and} \qquad \frac{\partial u}{\partial Y} = \alpha Y^{\alpha-1} f - Y^\alpha \frac{\mathrm{d}\phi}{\mathrm{d}Y}\frac{\mathrm{d}f}{\mathrm{d}\eta}. \tag{2.6}$$

To eliminate Y from the problem, we require that the two terms in $\partial u/\partial Y$ scale in the same way with Y. We therefore deduce that

$$\frac{\mathrm{d}\phi}{\mathrm{d}Y} = \frac{k}{Y} \quad \text{and thus} \quad \phi = k\log(Y), \tag{2.7}$$

for some constant k which will in general depend on n. (Note that there is no loss of generality in omitting the additive constant of integration, which merely affects the relative phase of the oscillation.) The magnitude of k controls the speed at which the waves propagate, while the sign of k determines the direction in which they propagate. When k is positive, waves travel in the direction of increasing Y, and when k is negative, they travel in the direction of decreasing Y. Consequently, to ensure that waves travel outwards from the oscillating wall, we will need to take $k > 0$ if $Y = y_0 + y$ and to take $k < 0$ if $Y = y_0 - y$.

Having determined $\phi(Y)$, we find

$$\frac{\partial u}{\partial Y} = Y^{\alpha-1}\left(\alpha f - k\frac{\mathrm{d}f}{\mathrm{d}\eta}\right), \tag{2.8}$$

so the governing equation (2.4) becomes

$$\begin{aligned} Y^\alpha \frac{\mathrm{d}f}{\mathrm{d}\eta} = nY^{n(\alpha-1)-1}\left|\alpha f - k\frac{\mathrm{d}f}{\mathrm{d}\eta}\right|^{n-1} \\ \times\left[(\alpha-1)\left(\alpha f - k\frac{\mathrm{d}f}{\mathrm{d}\eta}\right) - k\left(\alpha\frac{\mathrm{d}f}{\mathrm{d}\eta} - k\frac{\mathrm{d}^2 f}{\mathrm{d}\eta^2}\right)\right]. \end{aligned} \tag{2.9}$$

To eliminate Y we now require that

$$\alpha = n(\alpha - 1) - 1, \quad \text{i.e.} \quad \alpha = \frac{n+1}{n-1}. \tag{2.10}$$

Note that when $n > 1$ (a shear-thickening fluid), the exponent $\alpha > 0$: hence to satisfy the far-field condition we must take $Y = y_0 - y$ and restrict the solution to a layer of finite thickness $0 \leq y \leq y_0$. However, when $n < 1$ (a shear-thinning fluid), the exponent $\alpha < 0$ and we can take $Y = y_0 + y$ with algebraic decay as $y \to \infty$.

With this choice of α, equation (2.9) becomes a non-linear ordinary differential equation for the waveform $f(\eta)$,

$$\frac{\mathrm{d}f}{\mathrm{d}\eta} = n \left| \alpha f - k \frac{\mathrm{d}f}{\mathrm{d}\eta} \right|^{n-1} \left[(\alpha - 1) \left(\alpha f - k \frac{\mathrm{d}f}{\mathrm{d}\eta} \right) - k \left(\alpha \frac{\mathrm{d}f}{\mathrm{d}\eta} - k \frac{\mathrm{d}^2 f}{\mathrm{d}\eta^2} \right) \right], \tag{2.11}$$

which we must solve numerically, subject to the periodicity constraint $f(\eta) = f(\eta + 2\pi)$ for all η. We can further eliminate the parameter k at the expense of changing the period of the system, by defining

$$\eta = |k| \eta^* \quad \text{and} \quad f = |k|^{-1/(n-1)} f^*, \tag{2.12}$$

to obtain

$$\frac{\mathrm{d}f^*}{\mathrm{d}\eta^*} = n \left| \alpha f^* \mp \frac{\mathrm{d}f^*}{\mathrm{d}\eta^*} \right|^{n-1} \left[(\alpha - 1) \left(\alpha f^* \mp \frac{\mathrm{d}f^*}{\mathrm{d}\eta^*} \right) \mp \left(\alpha \frac{\mathrm{d}f^*}{\mathrm{d}\eta^*} \mp \frac{\mathrm{d}^2 f^*}{\mathrm{d}\eta^{*2}} \right) \right], \tag{2.13}$$

where the upper signs correspond to $k > 0$ and the lower to $k < 0$. If we can find a periodic solution for $f^*(\eta^*)$ over $0 \leq \eta^* \leq T^*$, we can obtain the corresponding periodic solution for $f(\eta)$ over $0 \leq \eta \leq 2\pi$ by setting $|k| = 2\pi / T^*$.

In summary, our self-similar solutions take the form

$$u(y,t) = \begin{cases} (y_0 - y)^{\alpha} f(t + |k| \log(y_0 - y);\ n) & \text{for} \quad n > 1, \\ (y_0 + y)^{\alpha} f(t - |k| \log(y_0 + y);\ n) & \text{for} \quad n < 1, \end{cases} \tag{2.14}$$

where the periodic functions $f(\eta; n)$ and the constants $k(n)$ are obtained numerically and where

$$\alpha = (n+1)/(n-1). \tag{2.15}$$

Some additional condition must be specified in order to select the boundary layer thickness y_0. For example, if the velocity imposed at the wall is precisely of the form $f(t)$ and has amplitude $\hat{U}$, so the oscillation has dimensionless amplitude 1 at $y = 0$, then y_0 must be given by

$$(y_0 \pm 0)^{\alpha} f_{\max} = 1, \quad \text{i.e.} \quad y_0 = f_{\max}^{-1/\alpha}, \tag{2.16}$$

where $f_{\max} = \max_{\eta} f(\eta)$. We will use this choice of y_0 for convenience when presenting our results in the following section. In general, however, when this self-similar solution acts as an asymptotic approximation to a solution with some different forcing imposed at the wall (as in the numerical integrations we will discuss in section 2.3), a more complicated matching process may be required to determine y_0. In these circumstances we will take $\hat{U}$ to be specified by the imposed forcing, noting that in this case the self-similar solution will not in general have unit amplitude at the wall.

2.2.3 Periodic solutions for shear-thickening fluids ($n > 1$)

We will first consider periodic solutions for shear-thickening fluids ($n > 1$). In this case, the exponent $\alpha > 0$: we must therefore take $Y = y_0 - y$ to satisfy the

far-field condition, and $k < 0$ so that waves propagate away from the wall.

Integrating (2.13) to obtain periodic solutions is slightly complicated by the fact that the equation becomes singular when $\partial u/\partial Y = 0$, i.e. along a 'critical line' in phase space on which $\alpha f^* + f^{*'} = 0$. This occurs twice in each period, corresponding to a corner in the solution for $f^*(\eta^*)$. The phase-space trajectories $(f^*(\eta^*), f^{*'}(\eta^*))$ cannot be integrated reliably across the critical line. It is, however, straightforward to show (see 2.6) that near to a point $(f_0^*, f_0^{*'})$ on the critical line, a trajectory behaves as

$$f^{*'} \sim f_0^{*'} + (f^* - f_0^*)^{1/n}. \tag{2.17}$$

We can then carry out numerical integrations forward in η^* from a point $(-f_0^* + \epsilon, -f_0^{*'} + \epsilon^{1/n})$ and backward in η^* from a point $(f_0^* + \epsilon, f_0^{*'} + \epsilon^{1/n})$, where $0 < \epsilon \ll 1$, and vary f_0^* until the trajectories meet at some point (e.g. $f^* = 0$); see section 2.7.1. Once these trajectories have been determined above the critical line, the part below the critical line can be completed by symmetry to create a closed trajectory. Figure 2.1 a gives examples of the resulting trajectories in phase space. If the waveform were sinusoidal the trajectories would be elliptical; in fact they become increasingly non-elliptical as n increases, so $f(\eta)$ adopts an increasingly 'saw-toothed' form (figures 2.1 b and c).

Having obtained $f^*(\eta^*)$, we can determine the period T^* from the numerical solutions and use it to deduce the parameter k using $|k| = 2\pi/T^*$ and thus, once y_0 has been determined, the 2π-periodic solution $f(\eta)$, as in figures 2.1 b and c. Note that by construction, the phase of the oscillations is chosen so that the corners in $f(\eta)$ occur at $\eta = m\pi$ for $m \in \mathbb{Z}$.

Equipped with $f(\eta)$ and the value of the parameter k, we can immediately construct solutions for $u(y, t)$ from (2.14). These are illustrated, for several val-

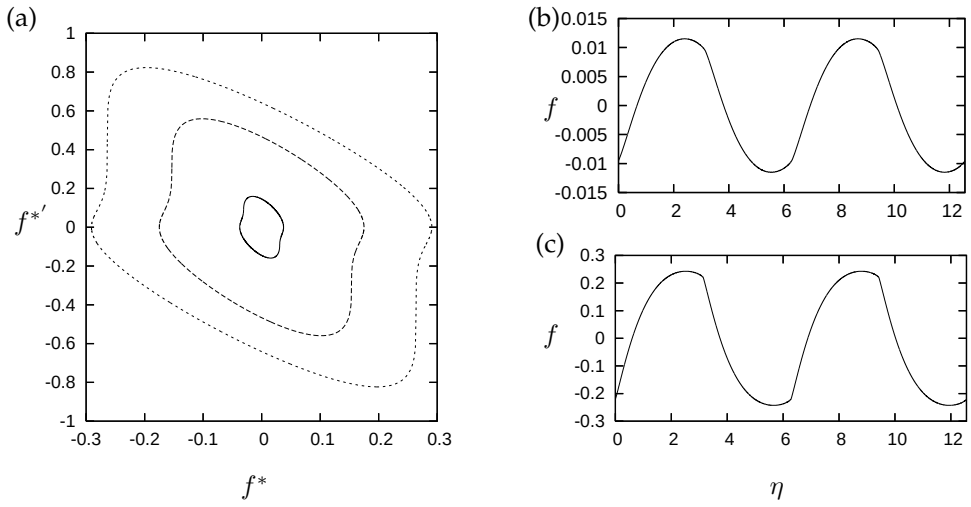

Figure 2.1: Solutions for $f(\eta)$ for $n = 2$ (solid lines), $n = 3$ (heavy dashed lines) and $n = 4$ (light dashed lines). Figure (a) shows phase-plane portraits $(f^*, f^{*'})$ while figures (b) and (c) show $f(\eta)$ over two periods for the cases (b) $n = 2$ and (c) $n = 4$.

ues of n, in figures 2.2 b–d (which show the waveform at various distances from the wall) and in figure 2.3 (which shows 'snapshots' of the velocity field at various times). In these figures, and elsewhere unless otherwise stated, the value of y_0 was determined using (2.16) so the oscillation has amplitude 1 at $y = 0$: this permits direct comparisons to be made between the solutions for different values of n.

In figures 2.2 b–d the deviation from a sinusoidal waveform with increasing n is again evident, and comparing these plots with that in the Newtonian case (figure 2.2 a), the faster decay with y is also evident. As n increases, the phase of the oscillations changes more slowly with y (i.e. the waves propagate more slowly), corresponding to the lower values of $|k|$.

The effect of changing n can also be seen in the snapshots in figure 2.3. These plots illustrate clearly both the changing envelope, with amplitude decaying more quickly away from $y = 0$ for higher n, and the increasingly non-sinusoidal

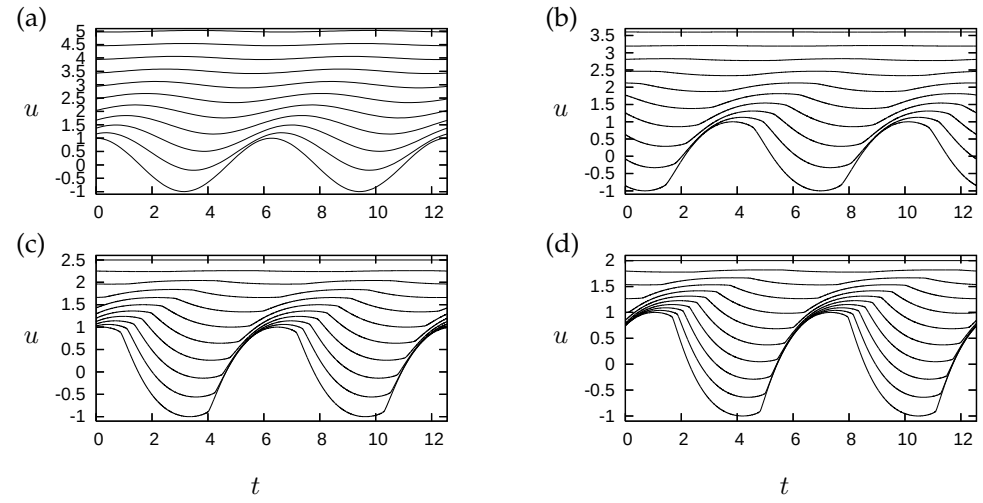

Figure 2.2: Solutions for $u(y,t)$ for (a) $n = 1$; (b) $n = 2$ ($k \approx -3.25$; $y_0 \approx 4.44$); (c) $n = 3$ ($k \approx -2.13$; $y_0 \approx 2.89$); and (d) $n = 4$ ($k \approx -1.72$; $y_0 \approx 2.34$). Plots are for $y = 0$ to y_0 in 10 equal steps (in (a), for $y = 0$ to 5 in 10 equal steps); successive lines in each plot are shifted upwards by equal but arbitrary amounts as y increases.

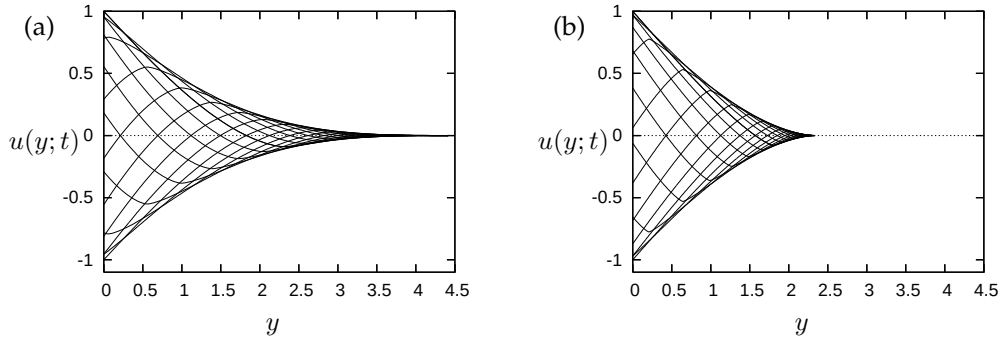

Figure 2.3: Snapshots of $u(y;t)$ at time intervals of $\pi/8$, for (a) $n = 2$ ($y_0 \approx 4.44$) and (b) $n = 4$ ($y_0 \approx 2.34$).

waveform, with profiles becoming more angular as n is increased.

2.2.4 Periodic solutions for shear-thinning fluids ($n < 1$)

We now consider shear-thinning fluids ($n < 1$), for which the exponent $\alpha < 0$. We must therefore take $Y = y + y_0$, and $k > 0$ so that waves propagate

away from the wall. As before, equation (2.13) is only formally valid away from the critical line where $\partial u/\partial Y = 0$. However, the system is not singular on the critical line, in contrast to the shear-thickening problem. This simplifies the numerical integration considerably. However, the closed trajectory which represents periodic solutions appears numerically to be an unstable limit cycle of the ODE, so to obtain it we must integrate backwards in η^*. Apart from this, the construction of the solutions proceeds as before.

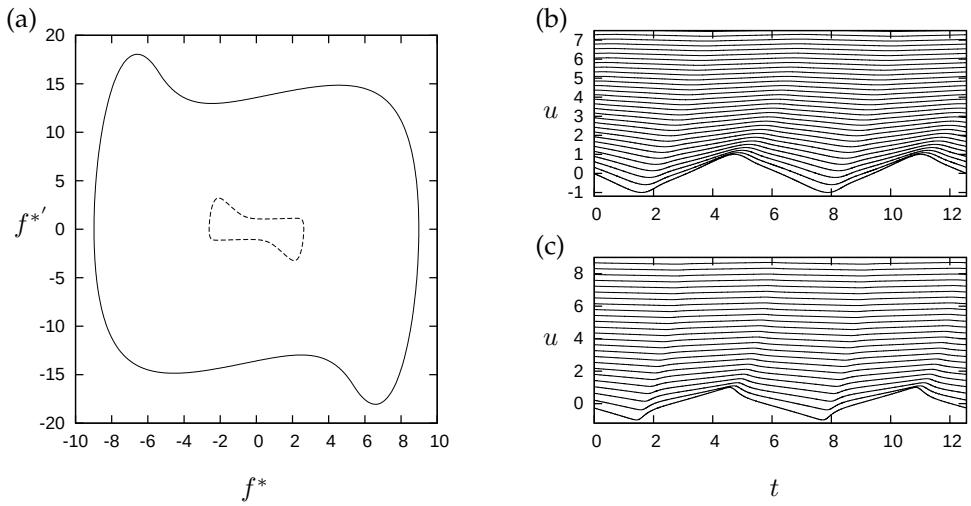

Figure 2.4: (a) Phase-plane portraits $(f^*, f^{*'})$ for $f(\eta)$ for $n = 0.5$ (solid lines) and $n = 0.25$ (dashed lines). (b, c) Solutions for $u(y,t)$ for (b) $n = 0.5$ ($k \approx 2.242$, $y_0 \approx 3.56$); (c) $n = 0.25$ ($k \approx 0.786$, $y_0 \approx 1.47$). Plots are at even increments of y starting at $y = 0$; successive lines in each plot are shifted upwards by equal but arbitrary amounts as y increases.

Figures 2.4 and 2.5 illustrate the results for the two cases $n = 0.5$ and $n = 0.25$. A conspicuous feature is that the waveforms $f(\eta)$ are no longer 'saw-toothed' as they were for shear-thickening fluids (compare figures 2.4 b and c with figures 2.1 b and c); rather, they have a nearly triangular 'shark-tooth' shape. Conversely, the nature of the snapshot profiles of $u(y;t)$ (figure 2.5) has altered: whereas the shear-thickening profiles were highly angular (figure 2.3),

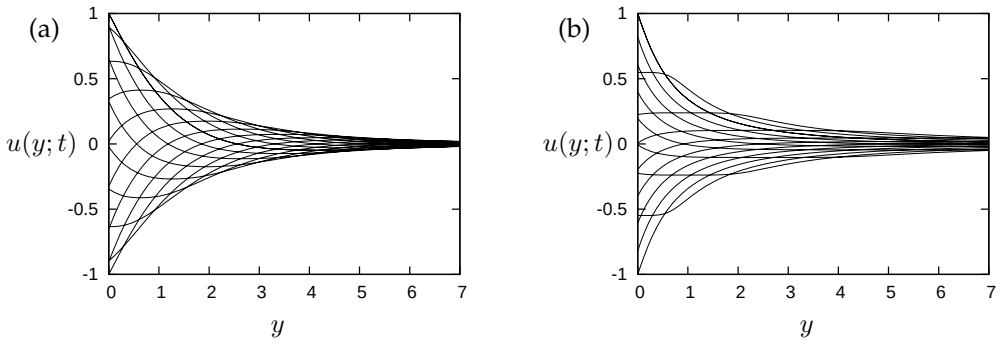

Figure 2.5: Snapshots of $u(y;t)$ at time intervals of $\pi/8$, for (a) $n = 0.75$ ($y_0 \approx 9.36$) and (b) $n = 0.25$ ($y_0 \approx 1.47$).

the shear-thinning profiles have more gentle variation and even show extensive regions of near-constant velocity during certain phases (figure 2.5 b).

Figure 2.5 also illustrates the more gentle amplitude decay for shear-thinning than for shear-thickening fluids. This decay becomes noticeable over distances of order y_0 from the wall: for $y \gtrsim y_0$ the decay becomes algebraic with exponent $\alpha < 0$. It turns out (see figure 2.6 b) that as n decreases, y_0 becomes smaller (favouring more rapid decay) but α also becomes smaller (favouring less rapid decay); consequently there is not a spectacular visual difference between the decay envelopes for $n = 0.25$ and $n = 0.75$ shown in figure 2.5.

2.2.5 Variation of the wavespeed and the boundary layer thickness with n

Figures 2.6 a and b present more systematically the variation with n of the wavespeed parameter k and of the boundary-layer thickness y_0 corresponding to unit amplitude at $y = 0$. (Figure 2.6 b also includes a comparison with the numerical results described in section 2.3.) As the fluid becomes more strongly non-Newtonian, i.e. the value of n differs more from unity, both the wavespeed parameter $|k|$ and the boundary layer thickness y_0 decrease. The limit $n \to 1$ is

singular because in this limit the definition of α breaks down.

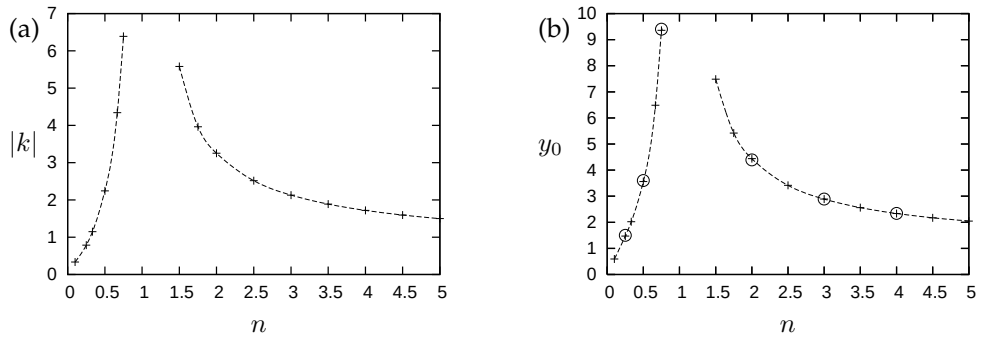

Figure 2.6: Results for (a) the wavespeed parameter $|k|$ and (b) the boundary layer thickness y_0 corresponding to unit amplitude at the wall. Pluses represent values from the semi-analytical solutions; dashed lines are a smoothed fit to these points, and circles in (b) represent the numerical fits $y_0^{(\mathrm{num})}$ reported in table 2.1.

2.2.6 Shear stress at the wall

In experiments, it may be simpler to control, or indeed to measure, the shear stress exerted by the wall on the fluid than to measure or control the velocity of the wall directly. It is therefore of interest to consider the shear stress predicted by our semi-analytical solutions.

The dimensionless shear stress at the wall is given by

$$\tau_w(t) = \left|\frac{\partial u}{\partial y}\right|^{n-1} \frac{\partial u}{\partial y}\bigg|_{y=0} = \pm y_0^{2n/(n-1)} \left|\alpha f(t) - k f'(t)\right|^{n-1} \left(\alpha f(t) - k f'(t)\right), \quad (2.18)$$

where the upper sign corresponds to $Y = y_0 + y$ (i.e. to shear-thinning cases, $n < 1$) and the lower sign to $Y = y_0 - y$ (i.e. to shear-thickening cases, $n > 1$). The corresponding expression for a Newtonian fluid is

$$\tau_w(t) = \frac{\partial u}{\partial y}\bigg|_{y=0} = \cos\left(t + \frac{5\pi}{4}\right), \quad (2.19)$$

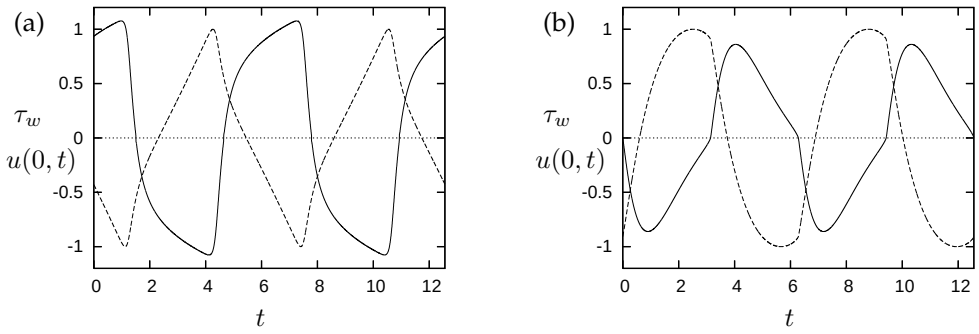

Figure 2.7: The wall shear stress (solid lines) and wall velocity (dashed lines) for (a) $n = 0.25$ and (b) $n = 4$.

so for a Newtonian fluid the shear stress also varies sinusoidally and its phase leads that of the velocity by $5\pi/4$ (see, e.g., Drazin and Riley 2006, §4. 1).

Figure 2.7 shows typical wall shear stress histories over two periods for a shear-thinning fluid ($n = 0.25$) and a shear-thickening fluid ($n = 4$). Since the shear stress does not vary with the same waveform as the velocity, a phase difference cannot be defined. However, it is apparent from figure 2.7 that in both shear-thinning and shear-thickening cases the stress and velocity are roughly in antiphase, with minima of τ_w roughly coinciding with maxima of $u(0,t)$ and vice versa. For shear-thinning fluids (figure 2.7(a)), a gradual increase in the magnitude of shear stress is followed by a rapid decrease; conversely, for shear-thickening fluids (figure 2.7 b), the magnitude of shear stress builds up rapidly and then more gradually diminishes. This qualitative difference may be useful as a means of distinguishing experimentally between shear-thinning and shear-thickening behaviour.

2.3 Numerical integration of the full problem

2.3.1 Numerical implementation

The dimensionless form of the governing equation (2.4), with $Y \equiv y$, was integrated numerically using the finite-element package Comsol 3.5a (Comsol 2009). A finite numerical domain $0 \leq y \leq y_{\max}$ was used, with the boundary conditions $u(0,t) = \cos(t)$ and $u(y_{\max},t) = 0$; the value of $y_{\max}$ was 10 unless otherwise stated. Integrations were started from the initial condition $u(y,0) = 0$ and run for several hundred time units until an effectively periodic state had been attained throughout the domain. The spatial resolution was 121 grid points, and the numerical relative tolerance was 10^{-4}; the results were robust to further refinement of these parameters. Run-times ranged from tens of minutes to several hours on a desktop PC.

The numerical and semi-analytical approaches cannot be expected to yield identical results, both because the numerical method solves an initial value problem rather than seeking perfectly time-periodic solutions, and because the numerical approach imposes a sinusoidal variation at the wall rather than the non-sinusoidal waveforms obtained in section 2.2. These differences provide a tough test of the semi-analytical solutions, which will be recovered only if they represent the attracting behaviour of the system when it is forced with a 'non-ideal' boundary velocity which is not proportional to the semi-analytical waveform $f(\eta)$. If the semi-analytical solutions are attractive then we should expect them to approximate the numerical results best at long times and some distance from the wall.

The two key features predicted by the semi-analytical solutions are the decay envelope of the oscillations and the non-sinusoidal form of the travelling wave. We now consider these features in turn, first for shear-thickening fluids with

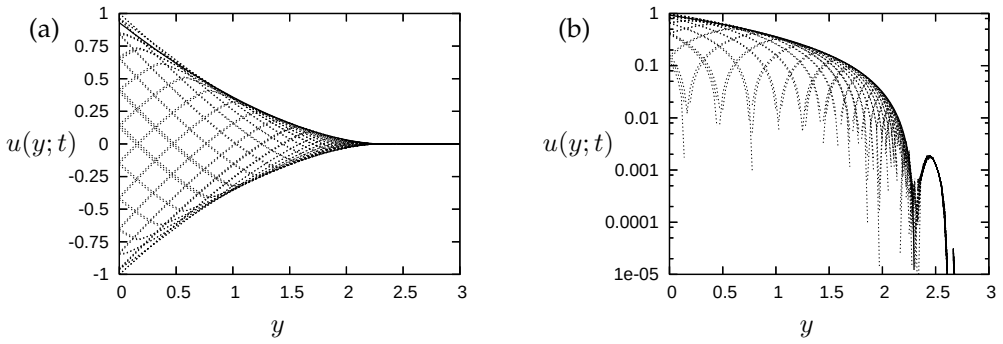

Figure 2.8: Fitting the envelope to numerical results for $n = 4$. Dotted lines are snapshots of $u(y;t)$ at frequent time intervals; the solid line is the envelope $u_{\max}(y) = a(1 - y/y_0^{(\mathrm{num})})^\alpha$ with fitted parameters $a = 0.93$ and $y_0^{(\mathrm{num})} = 2.3$. The two figures show the same data; note the logarithmic scale in (b).

$n > 1$, and then more briefly for shear-thinning fluids with $n < 1$.

2.3.2 Decay envelope for shear-thickening cases

Figure 2.8 a shows snapshots of the numerical velocity field at large times, for the shear-thickening case $n = 4$. The velocity field has become periodic in time almost everywhere, and decays rapidly with distance from the wall. (Note the strong resemblance to figure 2.3 b, which shows the corresponding semi-analytical results.) This behaviour can be seen more clearly in figure 2.8 b, where the same data are plotted on a logarithmic scale. In this figure, it is clear that the region of periodic oscillation extends up to $y \approx 2.3$, and beyond this there is a region of small but non-zero velocity which is changing only extremely slowly in time.

The region beyond $y \approx 2.3$ is a relic of the adjustment from the initial condition. Once a finite-thickness boundary layer has formed, the edge of this boundary layer (where the shear rate and thus the effective viscosity vanishes) acts as a barrier to the propagation of further information outward from the wall, and any non-zero flow beyond this point is effectively cut off from the periodic so-

n	α (exact)	y_0 (from (2.16))	$y_0^{(\mathrm{num})}$ (fitted)	a (fitted)
0.25	$-5/3$	1.47	1.5	1.15
0.5	-3	3.56	3.6	1.10
0.75	-7	9.36	9.4	1.02
2	3	4.44	4.39	0.93
3	2	2.89	2.84	0.92
4	$5/3$	2.34	2.30	0.93

Table 2.1: Fitted envelope parameters for various shear-thickening and shear-thinning cases. Note that the envelopes were fitted by eye so the fitted parameters may not be optimal.

lution. In practice, the numerical method cannot perfectly represent this barrier and a small amount of numerical noise is able to penetrate beyond the boundary layer, but with extremely low amplitudes visible only in figure 2.8 b.

It is easy to fit an envelope of the form $u_{\max}(y) = a(1 \mp y/y_0^{(\mathrm{num})})^\alpha$ to the numerical results. The fitting parameters are tabulated in table 2.1, while the fitted values of $y_0^{(\mathrm{num})}$ are also marked in figure 2.6 b. The fitting was carried out by eye: for shear-thickening cases, the region of steep decay in plots such as figure 2.8 b unambiguously determines $y_0^{(\mathrm{num})}$, and a was then adjusted so that the envelope matched the snapshots as closely as possible. Note that the value of α is determined by the semi-analytical solution and was not used as a fitting parameter; it is included in table 2.1 for completeness.

The numerical boundary layer thickness $y_0^{(\mathrm{num})}$ is not necessarily identical to that required for the semi-analytical solution to have unit amplitude at the wall, because the numerically imposed boundary condition is sinusoidal rather than having the form $u(0,t) \propto f(t)$. Despite this, the results in table 2.1 show that in practice $y_0^{(\mathrm{num})}$ is rather close to the value of y_0 given by (2.16). Similarly, the amplitude a of the fitted envelope at the wall is not necessarily equal to 1, because the adjustment from sinusoidal to non-sinusoidal waves does not necessarily preserve amplitude. The value of a relative to unity can be used as a

crude measure of how much this adjustment influences the solution. The values of a in table 2.1 are reasonably close to unity and, taken in conjunction with figure 2.8, provide convincing evidence that the semi-analytical solution provides a good description of the numerically calculated solution despite the issues involved in the adjustment from a sinusoidal to a non-sinusoidal waveform.

2.3.3 Waveform for shear-thickening cases

Figure 2.9 illustrates the adjustment of the waveform $f(\eta)$ as it propagates away from the wall. At the wall, the imposed numerical waveform is sinusoidal. By $y = 0.5$ (figure 2.9 a) this has already become distorted, and by $y = 1$ (figure 2.9 b) the 'saw-tooth' pattern is clear, with gradual increase to a maximum followed by a more rapid decrease. Subsequently the waveform adjusts more gradually towards the semi-analytical prediction (figures 2.9 c and d), with the cusp becoming more pronounced; by $y = 2$ (figure 2.9 d) there is a fairly good match between the numerically calculated and semi-analytical waveforms.

Unfortunately, because the waveform changes as it propagates away from the wall, it is not possible to define unambiguously a local propagation rate and thus to obtain numerical values of k to compare with the semi-analytical results.

2.3.4 Decay envelope and waveform for shear-thinning cases

Similar numerical integrations and fits to the semi-analytical solutions were carried out for a number of shear-thinning cases (see table 2.1). The adjustment to approximate periodicity was rather more rapid than in the shear-thickening cases: figures 2.10 and 2.11 illustrate typical results once periodicity had been attained.

In shear-thinning fluids, because the envelope decays rather slowly with y,

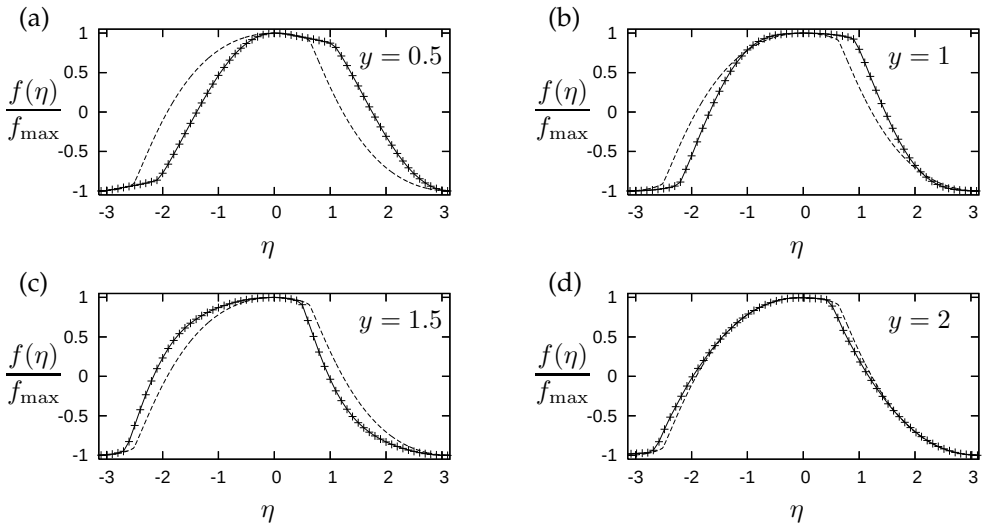

Figure 2.9: Normalised waveforms $f(\eta)/f_{\max}$ for $n = 4$: crosses are numerical results while dashed lines are the semi-analytical prediction. Numerical data were sampled starting at $t = 350$ for values of y as stated in the figures. Phases have been chosen in each case so that the maximum over a period occurs at $\eta = 0$.

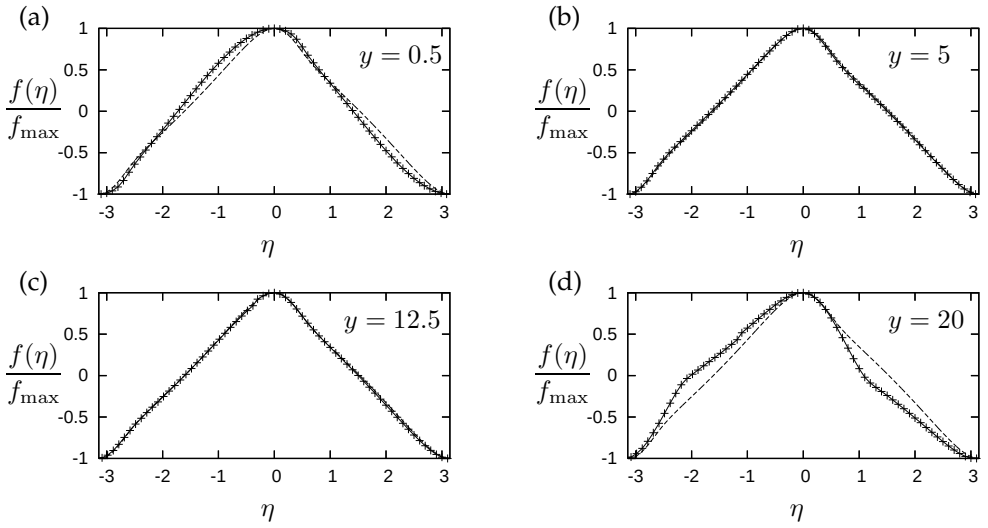

Figure 2.10: Normalised waveforms $f(\eta)/f_{\max}$ for $n = 0.5$, computed on the domain $0 \leq y \leq 25$: crosses are numerical data while dashed lines are the semi-analytical prediction. Numerical data were sampled starting at $t = 30$ for values of y as stated in the figures. Phases have been chosen in each case so that the maximum over a period occurs at $\eta = 0$.

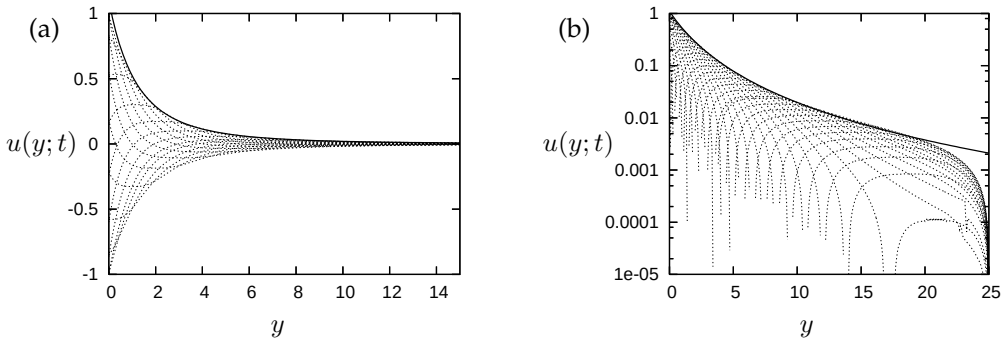

Figure 2.11: Fitting the decay envelope to numerical results for $n = 0.5$, computed on the domain $0 \leq y \leq 25$. Dotted lines are snapshots of $u(y;t)$ at frequent time intervals; the solid line is the envelope $u_{\max}(y) = a(1+y/y_0^{(\mathrm{num})})^{\alpha}$ with fitted parameters $a = 1.10$ and $y_0^{(\mathrm{num})} = 3.6$. The two figures show the same data set, although more frequent snapshots are shown in (b); also note the logarithmic scale in (b).

the boundary condition imposed at $y = y_{\max}$ can have an appreciable effect on the solutions. Indeed, because for low shear stresses the effective viscosity (i.e. the momentum diffusivity) is high, the influence of this boundary extends for a considerable distance. The results plotted were obtained for $y_{\max} = 25$, compared with $y_{\max} = 10$ in figure 2.9. When $y_{\max} = 10$ was used, the effect of the boundary was noticeable for $y \gtrsim 6.5$.

The waveforms shown in figure 2.10 (compare figure 2.9) illustrate the competing effects of the boundary condition at the wall, the boundary condition at $y = y_{\max}$ and the attracting semi-analytical solution. Close to the wall (figure 2.10 a) the imposed sinusoidal waveform can still be felt, although it has already become more angular. As y increases, the waveform adjusts to its semi-analytical 'shark-tooth' form (figure 2.10 b), and remains fairly close to this for some distance (figure 2.10 c). Eventually, the waveform starts to deviate as the effect of the boundary at $y_{\max}$ is felt, until by $y = 20$ (figure 2.10 d) it is significantly different from the semi-analytical prediction.

A similar improvement and then deterioration in agreement between the

numerical and semi-analytical solutions can be seen in figure 2.11, where the semi-analytical envelope is fitted to the snapshot data (compare figure 2.8). In contrast to the shear-thickening case, the fitting here is relatively insensitive to the boundary-layer thickness $y_0^{(\mathrm{num})}$, and the region of steep decay is due to the presence of the end wall at $y = 25$. There is also some evidence in figure 2.11 b of numerical error affecting very low values of u. The fit to the analytical envelope is best for the middle part of the domain where the waveforms also agree most closely with the semi-analytical solution, and the amplitude parameter a is now a little greater than unity. These issues notwithstanding, the semi-analytical solution again captures the greater part of the decay reasonably well.

2.4 Dimensional formulation

It is useful to consider the solutions in dimensional form, this will allow us to see how the width of the finite width boundary layer depends on the amplitude of oscillation. Starting with equation (2.14) we see that

$$\hat{u}(\hat{y},\hat{t}) = \begin{cases} \hat{U}\left(y_0 - \left(\frac{\hat{\omega}\hat{\rho}}{\hat{\mu}_n \hat{U}^{n-1}}\right)^{1/(n+1)} \hat{y}\right)^{\alpha} f\left(\hat{\omega}\hat{t} + |k| \log\left(y_0 - \left(\frac{\hat{\omega}\hat{\rho}}{\hat{\mu}_n \hat{U}^{n-1}}\right)^{1/(n+1)} \hat{y}\right);\ n\right) \\ \text{for} \quad n > 1, \\ \hat{U}\left(y_0 + \left(\frac{\hat{\omega}\hat{\rho}}{\hat{\mu}_n \hat{U}^{n-1}}\right)^{1/(n+1)} \hat{y}\right)^{\alpha} f\left(\hat{\omega}\hat{t} - |k| \log\left(y_0 + \left(\frac{\hat{\omega}\hat{\rho}}{\hat{\mu}_n \hat{U}^{n-1}}\right)^{1/(n+1)} \hat{y}\right);\ n\right) \\ \text{for} \quad n < 1 \end{cases} \tag{2.20}$$

in dimensional form. We can now obtain a formula for y_0 equivalent to equation (2.16)

$$y_0 = \left(\frac{\hat{u}}{\hat{U}} f_{max}\right)^{-1/\alpha}. \tag{2.21}$$

We can see that as the amplitude of oscillation, $\hat{U}$, increases, y_0 will decrease for shear-thickening ($n > 1$) fluids and increase for shear-thinning ($n < 1$) fluids.

2.5 Summary

We have presented semi-analytical, self-similar solutions for the temporally periodic rectilinear flow of a power-law fluid driven by an oscillating wall. In non-dimensional form, these solutions may be written as

$$u(y,t) = \begin{cases} (y_0 - y)^{\alpha} f(t + |k| \log(y_0 - y);\ n) & \text{for} \quad n > 1, \\ (y_0 + y)^{\alpha} f(t - |k| \log(y_0 + y);\ n) & \text{for} \quad n < 1, \end{cases} \tag{2.22}$$

where the periodic functions $f(\eta; n)$ and the constants $k(n)$ are obtained numerically; where $\alpha = (n+1)/(n-1)$; and where y_0 is determined by matching to the flow driven by the boundary condition at the wall.

The most interesting feature of these solutions is that for shear-thickening fluids ($n > 1$), they predict a boundary layer of finite thickness, with the motion dying out completely beyond a certain distance from the wall. This is reminiscent of the behaviour in the Rayleigh problem for power-law fluids studied by Pascal (1992). It is also reminiscent of the finite thickness of the oscillatory shear layer in the viscoplastic Stokes problem (Balmforth, Forterre, and Pouliquen 2009). However, it arises for almost exactly the opposite reason: because the viscosity of a shear-thickening fluid decreases as the shear rate decreases, the viscosity at the edge of the boundary layer is zero and the diffusing signal cannot penetrate further into the fluid. A consequence of this is that in a shear-thickening fluid the flow outwith the boundary layer can remain unaffected by the motion of the wall: essentially the fluid has developed an internal slip

surface separating non-communicating regions. In a less idealised rheological model with a small but non-zero effective viscosity at zero shear rate, some communication between these regions would be possible. However, the ability of the numerical approach to replicate the slip surface, despite the inevitable presence of numerical diffusion, suggests that 'pseudo-slip' behaviour might still be possible.

Conversely, for shear-thinning fluid the influence of the wall extends much further into the fluid than in the Newtonian case, decaying algebraically rather than exponentially with distance from the wall. In the context of fluid mud mobilisation and transport, this behaviour implies that shear-thinning muds may be mobilised to substantially greater depths than a crude estimate based on a Newtonian boundary layer thickness would suggest.

Another clear qualitative indicator of shear-thickening or shear-thinning behaviour is the non-sinusoidal waveform of the velocity oscillations. For shear-thickening fluids the oscillations adopt a 'saw-tooth' form, with a rapid decrease in absolute velocity after each minimum or maximum; shear-thinning fluids prefer a 'shark-tooth' waveform which is nearly triangular with rapid reversal at each maximum. The histories of shear stress on the oscillating wall also differ: shear-thinning cases are characterised by gradual increases in stress followed by rapid decreases, whereas shear-thickening cases are characterised by rapid increases in stress followed by more gradual decreases.

These results are not of interest solely as the solutions to a very specific boundary-value problem. Numerical integration of the governing equation with sinusoidal forcing at the wall demonstrates that the self-similar solutions represent attracting states for the system, and so provide a good approximation of the solution even when the forcing is not specifically designed to produce them. For shear-thinning fluids, the influence of the zero-velocity condition

at the non-oscillating end wall means that the self-similar solutions are only a good approximation in the middle part of the domain; nevertheless they capture the propagating waveform and the decay envelope reasonably well.

2.6 Appendix: trajectories near the critical line when $n > 1$

For values of $n > 1$, the second derivative of f^* in equation (2.13) must become unbounded on the critical line $\alpha f^* + f^{*'} = 0$. (Recall that $k < 0$ whenever $n > 1$.) We may use the chain rule to write $\mathrm{d}^2 f^*/\mathrm{d}\eta^{*2} = \mathrm{d}f^{*'}/\mathrm{d}\eta^* = (\mathrm{d}f^{*'}/\mathrm{d}f^*)f^{*'}$ so that equation (2.13) becomes

$$f^{*'} = n\left|\alpha f^* + f^{*'}\right|^{n-1}\left[(\alpha-1)\left(\alpha f^* + f^{*'}\right) + \alpha f^{*'} + f^{*'}\frac{\mathrm{d}f^{*'}}{\mathrm{d}f^*}\right]. \tag{2.23}$$

Setting $f^* = f_0^* + \epsilon$ and taking the Ansatz $f^{*'} = f_0^{*'} + \delta_0\epsilon^\beta$ for some $\beta > 0$, where $\alpha f_0^* + f_0^{*'} = 0$, we obtain

$$f_0^{*'} + \delta_0\epsilon^\beta \sim n\left|\alpha\epsilon + \delta_0\epsilon^\beta\right|^{n-1} \times\left[(\alpha-1)\left(\alpha\epsilon + \delta_0\epsilon^\beta\right) + \left(f_0^{*'} + \delta_0\epsilon^\beta\right)\left(\alpha + \delta_0\beta\epsilon^{\beta-1}\right)\right]. \tag{2.24}$$

Keeping only possible leading-order terms and assuming $f_0^{*'} \neq 0$, this reduces to

$$1 \sim n\left|\alpha\epsilon + \delta_0\epsilon^\beta\right|^{n-1}\left[\alpha + \delta_0\beta\epsilon^{\beta-1}\right]. \tag{2.25}$$

We now need to consider the size of β. If $\beta > 1$ then the leading-order balance reduces to

$$1 \sim n\left|\alpha\epsilon\right|^{n-1}\alpha, \tag{2.26}$$

which is inadmissible because the powers of ϵ do not balance. On the other hand, if $\beta < 1$ then the leading-order balance becomes

$$1 \sim n \left|\delta_0 \epsilon^\beta\right|^{n-1} \delta_0 \beta \epsilon^{\beta-1}, \tag{2.27}$$

which is valid as long as $\beta(n-1)+\beta-1=0$, i.e. $\beta = 1/n < 1$. This is consistent; the constant $\delta_0 = 1$ follows immediately, and we have leading-order behaviour of the form

$$f^* = f_0^* + \epsilon, \qquad f^{*'} \sim f_0^{*'} + \epsilon^{1/n} \tag{2.28}$$

given in (2.17).

2.7 Appendix: Maple code

2.7.1 Code for obtaining $f(\eta)$

```
>restart;with(plots):
```

Define α from equation (2.15).

```
>alpha:= (n+1)/(n-1):
```

Set up governing equation (2.11).

```
>feq:= diff(f(eta),eta)=abs(alpha*f(eta)+diff(f(eta),eta))
∧(n-1)*(n*(alpha-1)*(alpha*f(eta)+diff(f(eta),eta))+n*
(alpha *diff(f(eta),eta)+diff(f(eta),eta$2)));
```

Critical f at which solution blows up.

```
>dfcrit(f0):= -alpha*f0;
```

Shooting problem: shoot away from the critical line and match on $f = 0$.

```
>ic1:= f(0)=f0+epsilon, D(f)(0)=dfcrit(f0)+epsilon∧n;
>ic2:= f(0)=-f0+epsilon, D(f)(0)=subs(f0=-f0,dfcrit(f0))+
```

```
epsilon^n;
```

Set parameter values.

```
>parvals:= f0=-0.2638,epsilon=0.000001,n=4;
>sol1:= dsolve(subs(parvals,feq,ic1),f(eta),numeric):
>sol2:= dsolve(subs(parvals,feq,ic2),f(eta),numeric):
```

Plot f and change `f0` value until the lines match up.

```
>display([odeplot(sol1,[f(eta),diff(f(eta),eta)],0..1,
numpoints=2000,color=blue), odeplot(sol2,[f(eta),diff
(f(eta),eta)],-1..0,numpoints=2000,color=black), plot(
-5/3*x,x=-0.3..0.3,color=gray)]);
```

We use this plot to determine T^* and hence allow us to determine k.

```
>display([ odeplot(sol1,[f(eta),diff(f(eta),eta)],0..
1.8266914, numpoints=2000,color=blue), plot(-5/3*x,x=-0.3
..0.3,color=gray)]);
>odeplot(sol1,[[eta,f(eta)],[eta+1.8266914,f(eta)]],0..
1.8266914,numpoints=1000);
```

This procedure builds up an array of data for $f^*(\eta)$ and $f^{*'}(\eta)$.

```
>fstararray:= proc(npts,T) global farr; local i, etai;
for i from 0 to npts do etai:= evalf(T*i/npts);
farr[i,0]:= etai;
farr[i,1]:= subs(sol1(etai),f(eta));
farr[i,2]:= subs(sol1(etai),diff(f(eta),eta));
farr[i+npts,0]:= etai+T;
farr[i+npts,1]:= subs(sol1(etai),-f(eta));
farr[i+npts,2]:= subs(sol1(etai),-diff(f(eta),eta)) od;
end;
```

This procedure takes an (arbitrary) value of η^* and returns the correspond-

ing values of f^* and $f^{*'}$.

```
>fstarout:= proc(eta,npts,T) global farr; local i, eta0,
fstari, dfstari;
eta0:= eta-2*T*floor(eta/(2*T));
for i from 0 to 2*npts-1 do
if (farr[i,0]-eta0)*(farr[i+1,0]-eta0)<=0 then fstari:=
farr[i,1]+(farr[i+1,1]-farr[i,1])/(farr[i+1,0]-farr[i,0])*
(eta0-farr[i,0]);
dfstari:= farr[i,2]+(farr[i+1,2]-
farr[i,2])/(farr[i+1,0]-farr[i,0])*
(eta0-farr[i,0]) fi od;
return(fstari,dfstari);
end;
```

This procedure evaluates (approximately) the maximum value of f^* and the corresponding value of η^*.

```
>fstarmaxout:= proc(npts,T) global farr; local i, fstari,
fstarip1, fstarim1, fmax, imax;
fmax:= farr[0,1];
for i from 1 to 2*npts do if(farr[i,1]>fmax) then fmax:=
farr[i,1];
imax:= i fi od; return(fmax,evalf(imax*T/npts));
end;
```

This procedure writes out four data sets to the file: the first is a couple of periods of $f^*(\eta)$; the second is a couple of periods of $f(\eta)$; the third is the phase plane portrait (f^*,$f^{*'}$); the fourth is the rescaled phase plane portrait (f,f').

```
>fplotsout:= proc(npts,T,filout) global parvals, farr;
local n0, k, i, etai, fd;
```

```
fd:= open(filout,WRITE);
n0:= subs(parvals,n);
fprintf(fd,"# n = % f;
f0 = %f\n",n0,subs(parvals,f0));
fprintf(fd,"# Half-period = %f\n",T);
k:= evalf(Pi/T);
fprintf(fd,"# Scale factor |k| = %f\n",k);
fprintf(fd,"# Scale factor |k|^(-1/(n-1))=%f\n",k^(-1/
(n0-1)));
fprintf(fd,"\n\n# f^*(eta^*) over two periods\n");
for i from 0 to 2*npts do fprintf(fd,"%f %f\n",farr[i,0],
farr[i,1]) od;
for i from 0 to 2*npts do fprintf(fd,"%f %f\n", farr[i,0]
+2*T,farr[i,1]) od;
fprintf(fd,"\n\n# f(eta) over two periods\n");
for i from 0 to 2*npts do fprintf(fd,"%f %f\n",k*farr[i,0],
k^(-1/(n0-1))*farr[i,1]) od;
for i from 0 to 2*npts do fprintf(fd,"%f %f\n", k*farr[i,0]
+2*Pi,k^(-1/(n0-1))*farr[i,1]) od;
fprintf(fd,"\n\n# (f^*,f^*') over a period\n");
for i from 0 to 2*npts do fprintf(fd,"%f %f\n",farr[i,1],
farr[i,2]) od;
fprintf(fd,"\n\n# (f,f') over a period\n");
for i from 0 to 2*npts do fprintf(fd,"%f %f\n",k^(-1/(n0
-1))*farr[i,1],k^(-1/(n0-1)-1)*farr[i,2]) od;
close(fd);
end;
```

This procedure calculates y_0 such that the amplitude at the wall is 1; it then outputs ny evenly spaced "cross-section" plots between $y = 0$ and $y = y_0$.

```
xsecout:= proc(npts,T,ny,nperiods,ushift,filout) global
parvals, farr;
local n0, k, fmax, y0, m, j, yj, phij, tij, i, etai, fd;
n0:= subs(parvals):
k:= evalf(Pi/T);
fmax:= k∧(-1/(n0-1))*op(1,[fstarmaxout(npts,T)]);
y0:= 1/fmax∧((n0-1)/(n0+1));
fd:= open(filout,WRITE);
for j from 0 to ny-1 do yj:= evalf(y0*j/ny);
phij:= -k*log(y0-yj);
for m from -2 to nperiods-2 do
for i from 0 to 2*npts do tij:= m*2*Pi+k*farr[i,0]+phij;
fprintf(fd,"%f %f\n",tij,(y0-yj)∧((n0+1)/(n0-1))*k∧(-1/
(n0-1)) *farr[i,1]+j*ushift) od;
fprintf(fd,"\n\n") od;
od;
close(fd);
end;
```

This procedure calculates y_0 as above and then outputs n snapshots between $y = 0$ and $y = y_0$, phase shifted so the first snapshot occurs when the amplitude is maximum at the wall.

```
snapout:= proc(npts,T,ny,nsnap,filout) global parvals,
farr;
local n0, k, fmax, etamax, tmax, y0, m, j, yj, phij, ti,
i, etaij, fstarij, fd;
```

```
n0:= subs(parvals,n);
k:= evalf(Pi/T);
fmax:= k^(-1/(n0-1))*op(1,[fstarmaxout(npts,T)]);
etamax:= k*op(2,[fstarmaxout(npts,T)]);
y0:= 1/fmax^((n0-1)/(n0+1));
tmax:= etamax-k*log(y0);
fd:= open(filout,WRITE);
for i from 0 to nsnap do ti:= tmax+evalf(2*Pi*i/nsnap);
for j from 0 to ny-1 do yj:= evalf(y0*j/ny);
phij:= -k*log(y0-yj);
etaij:= ti-phij;
fstarij:= op(1,[fstarout(etaij/k,npts,T)]);
fprintf(fd,"%f %f\n",yj,0*ti+(y0-yj)^((n0+1)/(n0-1))*k^
(-1/(n0-1))*fstarij) od;
fprintf(fd,"\n\n") od;
close(fd);
end;
```

Chapter 3

The Stokes problem for thixotropic and antithixotropic fluids

In this chapter, we will employ a combined asymptotic and numerical approach to explore the structure of the Stokes layer for both thixotropic and antithixotropic fluids. We will develop asymptotic solutions in the limit of small-amplitude oscillations, which reveal three essentially different ways in which the fluid structure can evolve while satisfying periodicity. We will then verify and extend these asymptotic results through direct numerical integration of the governing equations. Our aim throughout is to explore the full range of possible behaviours that the model can exhibit, rather than to produce a single set of detailed results for validation against particular laboratory data.

In section 3.1 we describe the rheological model and the governing equations for the problem. We then investigate the two main rheological regimes represented by our model: thixotropic behaviour (section 3.2) and antithixotropic behaviour (section 3.3); an intermediate pseudo-Newtonian regime is dealt with in an appendix section 3.6. In section 3.4 we examine 'rheogram' plots of shear stress against shear rate for these solutions, and discuss the information that

these plots yield. Finally, in section 3.5 we summarise our results and comment on the general conclusions that may be drawn from them.

3.1 Mathematical model

3.1.1 Rheological model and governing equations

Recall that the general model by Mewis and Wagner (2009) for thixotropic and antithixotropic fluids comprises an evolution equation for the scalar structure parameter λ together with a constitutive relation giving the shear stress tensor $\hat{\tau}_{ij}$ in terms of the shear rate tensor $\hat{e}_{ij}$ and the local value of λ.

The structure equation (1.16) is

$$\frac{\mathrm{D}\lambda}{\mathrm{D}\hat{t}} = -\hat{k}_1\dot{\gamma}^a\lambda^b + \hat{k}_2\dot{\gamma}^c(1-\lambda)^d, \tag{3.1}$$

where the shear rate $\dot{\gamma}$ is defined by equation (1.2). Here $\hat{k}_1$ and $\hat{k}_2$ are the rate constants for structural breakdown and build-up respectively, while a, b, c and d are non-negative dimensionless exponents. We will show in section 3.1.4 that values $a > c$ correspond to thixotropic behaviour and values $c > a$ to antithixotropic behaviour. We will also show that in the present problem the exponents in (3.1) determine the regime of behaviour in an unexpectedly subtle manner. This suggests that it may be necessary to pay more attention to the formulation of structure evolution equations than they have tended to receive. Note that the structure parameter λ is dimensionless and takes values between 0 (a fully unstructured fluid) and 1 (a fully structured fluid).

We complete the rheological model by specifying the constitutive law

$$\hat{\tau}_{ij} = \hat{\eta}_0\lambda\hat{e}_{ij}, \quad \text{where} \quad \hat{e}_{ij} = \frac{\partial\hat{u}_i}{\partial\hat{x}_j} + \frac{\partial\hat{u}_j}{\partial\hat{x}_i}, \tag{3.2}$$

which as noted in section 1.2.4 is a version of the model originally proposed by Moore (1959).

3.1.2 Problem formulation and governing equations

The flow is governed by the mass conservation and Navier–Stokes equations

$$\hat{\nabla} \cdot \hat{\mathbf{u}} = 0 \quad \text{and} \quad \hat{\rho}\frac{\mathrm{D}\hat{\mathbf{u}}}{\mathrm{D}\hat{t}} = -\hat{\nabla}\hat{p} + \hat{\nabla} \cdot \underline{\underline{\hat{\tau}}}, \tag{3.3}$$

where the velocity $\hat{\mathbf{u}} = \hat{u}(\hat{y}, \hat{t})\mathbf{e}_x$, pressure $\hat{p} = \hat{p}(\hat{y}, \hat{t})$ and structure parameter $\lambda = \lambda(\hat{y}, \hat{t})$ are all assumed to be independent of the wall-parallel co-ordinate $\hat{x}$.

From equation (1.2), the shear rate is given by $\dot{\gamma} = |\partial\hat{u}/\partial\hat{y}|$. The momentum balance in the $\hat{y}$-direction yields $\hat{p} = \hat{p}(\hat{t})$ only so pressure need not be considered, while in the $\hat{x}$-direction combining equation (3.3) with the constitutive equation (3.2) yields

$$\frac{\partial\hat{u}}{\partial\hat{t}} = \hat{\nu}_0\frac{\partial}{\partial\hat{y}}\left(\lambda\frac{\partial\hat{u}}{\partial\hat{y}}\right), \tag{3.4}$$

where $\hat{\nu}_0 = \hat{\eta}_0/\hat{\rho}$.

Since λ is independent of $\hat{x}$, the convective derivative in the structure equation (3.1) reduces to $\partial\lambda/\partial\hat{t}$ and hence λ satisfies

$$\frac{\partial\lambda}{\partial\hat{t}} = -\hat{k}_1\left|\frac{\partial\hat{u}}{\partial\hat{y}}\right|^a\lambda^b + \hat{k}_2\left|\frac{\partial\hat{u}}{\partial\hat{y}}\right|^c(1-\lambda)^d. \tag{3.5}$$

To solve this system of equations we must specify a boundary condition at the oscillating wall $\hat{y} = 0$ and a far-field condition as $\hat{y} \to \infty$. For simplicity and consistency with the standard Newtonian problem, (1.21), we assume that the wall oscillates sinusoidally with amplitude $\hat{u}_0$, so the no-slip condition yields $\hat{u}(0, \hat{t}) = \hat{u}_0\cos(\hat{\omega}\hat{t})$, and that the velocity decays to zero from the wall so $\hat{u} \to 0$

as $\hat{y} \to \infty$.

3.1.3 Non-dimensionalisation

Before proceeding further we non-dimensionalise the problem. We set $\hat{u} = \hat{U}_0 u$, $\hat{y} = \hat{Y}_0 y$ and $\hat{t} = \hat{T}_0 t$, where the characteristic velocity, length and time scales $\hat{U}_0$, $\hat{Y}_0$ and $\hat{T}_0$ are given by

$$\hat{U}_0 = \hat{\nu}_0^{1/2} \left(\frac{\hat{k}_1^{c-2}}{\hat{k}_2^{a-2}} \right)^{1/(2(a-c))}, \quad \hat{Y}_0 = \hat{\nu}_0^{1/2} \left(\frac{\hat{k}_1^{c}}{\hat{k}_2^{a}} \right)^{1/(2(a-c))}, \quad \hat{T}_0 = \left(\frac{\hat{k}_1^{c}}{\hat{k}_2^{a}} \right)^{1/(a-c)}. \tag{3.6}$$

Note that these scales apply only when $a \neq c$. The special case $a = c$, in which the behaviour is 'pseudo-Newtonian', is treated in section 3.6.

The dimensionless problem is therefore given by

$$\frac{\partial u}{\partial t} = \frac{\partial}{\partial y} \left(\lambda \frac{\partial u}{\partial y} \right) \tag{3.7}$$

and

$$\frac{\partial \lambda}{\partial t} = - \left| \frac{\partial u}{\partial y} \right|^a \lambda^b + \left| \frac{\partial u}{\partial y} \right|^c (1 - \lambda)^d, \tag{3.8}$$

subject to the boundary condition $u(0,t) = \epsilon \cos(\omega t)$, where $\epsilon = \hat{u}_0 / \hat{U}_0$ is the non-dimensional amplitude and $\omega = \hat{\omega} \hat{T}_0$ the non-dimensionless frequency of the wall oscillations, and subject also to the far-field condition $u \to 0$ as $y \to \infty$. Note that since $\hat{T}_0$ is defined in terms of the structure response timescales, ω may be interpreted as a Deborah number for the problem (section 1.2.5).

When carrying out numerical integrations, we will also specify the initial conditions $u(y,0) = 0$ and $\lambda(y,0) =$ constant. However, our main interest is in the behaviour at large times. We will show that, as might be expected, transients

that depend on the precise initial condition die away and the system adjusts to a periodic state in this limit. When seeking periodic solutions we will impose the periodicity conditions

$$\lambda(x, t + 2\pi/\omega) = \lambda(x, t) \qquad \text{and} \qquad u(x, t + 2\pi/\omega) = u(x, t) \tag{3.9}$$

for all x and t, instead of specifying initial conditions.

Solving equations (3.7) and (3.8) is a difficult problem which must, in general, be tackled numerically. However, analytical progress can also be made in the asymptotic limit $\epsilon \to 0$ corresponding to small amplitude oscillations of the wall. This asymptotic limit is especially informative because it allows us to distinguish different regimes of rheological behaviour, characterised by different responses of the structure to the oscillating shear rate. We will now discuss these possible responses.

3.1.4 Instantaneous and time-averaged rheological equilibrium

It will be useful to distinguish two qualitatively different ways in which the fluid structure may reach an 'equilibrium' with the local shear rate. These represent different limiting behaviours of the structure, and will emerge in our asymptotic analysis from different dominant balances in equation (3.8).

When the response time for the structure is very short compared with the timescale over which the shear rate changes, i.e. in the limit of small Deborah number, $\omega \to 0$, we may expect the value of λ to be instantaneously determined by the shear rate. In this limit, the time derivative in (3.8) is negligible, and $\lambda = \lambda_{\text{eq}}$, where

$$\frac{\lambda_{\text{eq}}^b}{(1 - \lambda_{\text{eq}})^d} = \left|\frac{\partial u}{\partial y}\right|^{c-a}. \tag{3.10}$$

We shall refer to this as 'fast-adjusting' behaviour. The resulting equilibrium stress-shear curve allows us to distinguish between the rheological regimes represented by our model. Since the left-hand side of (3.10) is a monotonically increasing function of λ_{eq}, we see that λ_{eq} increases with increasing shear rate for $a < c$, giving shear-thickening (antithixotropic) behaviour, while λ_{eq} decreases with increasing shear rate for $a > c$, giving shear-thinning (thixotropic) behaviour.

In antithixotropic cases, $a < c$, it is simple to show that the equilibrium shear stress, $\tau_{\mathrm{eq}} = \lambda \partial u/\partial y$, is an increasing function of $\partial u/\partial y$. In thixotropic cases, $a > c$, it is less simple: τ_{eq} is an increasing function of $\partial u/\partial y$ for small shear rates, but at large shear rates we obtain the asymptotic result $|\tau_{\mathrm{eq}}| \sim |\partial u/\partial y|^{(b+c-a)/b}$. Thus, if the shear-thinning effect is strong enough at large shear rates, i.e. if $b + c - a < 0$, the model allows τ_{eq} to decrease with increasing shear. Since this appears physically unrealistic, we will not consider this parameter range in our study.

When the response time for the structure is very long compared with the timescale over which the shear rate changes, i.e. in the limit of large Deborah number, $\omega \to \infty$, the response is more subtle. Over a period of oscillation the local value of λ must remain almost constant and there is no reason in general for it to be in equilibrium with the local shear rate. However, if periodicity is required then there must be rheological equilibrium in a period-averaged sense. Integrating (3.8) and imposing periodicity gives

$$0 = -\int_0^{2\pi/\omega} \left|\frac{\partial u}{\partial y}\right|^a \lambda^b \mathrm{d}t + \int_0^{2\pi/\omega} \left|\frac{\partial u}{\partial y}\right|^c (1-\lambda)^d \mathrm{d}t, \tag{3.11}$$

and since in this limit λ is independent of time, we may rearrange equation

(3.11) to yield $\lambda = \lambda_{\text{av}}$, where

$$\frac{\lambda_{\text{av}}^b}{(1-\lambda_{\text{av}})^d} = \frac{\displaystyle\int_0^{2\pi/\omega} \left|\frac{\partial u}{\partial y}\right|^c \mathrm{d}t}{\displaystyle\int_0^{2\pi/\omega} \left|\frac{\partial u}{\partial y}\right|^a \mathrm{d}t}. \tag{3.12}$$

We shall refer to this as 'slowly-adjusting' behaviour. Again, the criteria $a \gtrless c$ correspond to thixotropic and antithixotropic behaviour, but now defined in terms of averages of the shear rate of the fluid.

3.2 Thixotropic behaviour, $a > c$

We first consider the case in which the rheology is thixotropic, $a > c$. In order to make analytical progress we will first develop asymptotic solutions in the limit of small-amplitude wall oscillations, $\epsilon \to 0$; we will then extend these solutions numerically to larger values of ϵ.

3.2.1 Asymptotic solutions for small-amplitude wall oscillations

For the rates of structural build-up and breakdown to be comparable in magnitude in the limit $\epsilon \to 0$, the fluid must be highly structured, with λ close to unity everywhere. We therefore seek asymptotic solutions of the form

$$u(y,t) = \epsilon u_1(y,t) + o(\epsilon) \qquad \text{and} \qquad \lambda(y,t) = 1 - \epsilon^h \lambda_1(y,t) + o(\epsilon^h), \tag{3.13}$$

where the exponent $h > 0$ remains to be determined. The boundary conditions are $u_1(0,t) = \cos(\omega t)$ and $u_1 \to 0$ as $y \to 0$. Note that because of the thixotropic rheology we may also expect λ_1 to be largest close to the wall where shear rates

are highest, and to tend to zero as $y \to \infty$.

Substituting the expansion (3.13) into equation (3.7) and retaining only leading-order terms yields

$$\frac{\partial u_1}{\partial t} = \frac{\partial^2 u_1}{\partial y^2}. \tag{3.14}$$

Solving (3.14) subject to the boundary and far-field conditions yields

$$u(y,t) \sim \epsilon u_1(y,t) = \epsilon \mathrm{e}^{-\gamma y} \cos(\gamma y - \omega t) \quad \text{with} \quad \gamma = \sqrt{\frac{\omega}{2}}, \tag{3.15}$$

so at first order we recover the Newtonian solution (1.21).

Substituting (3.13) into equation (3.8) yields

$$-\epsilon^h \frac{\partial \lambda_1}{\partial t} = -\epsilon^a \left| \frac{\partial u_1}{\partial y} \right|^a + \epsilon^{c+hd} \left| \frac{\partial u_1}{\partial y} \right|^c \lambda_1^d + \text{higher order terms.} \tag{3.16}$$

Integrating (3.16) over a period and applying the periodicity condition (3.9) then yields

$$0 = -\epsilon^a \int_0^{2\pi/\omega} \left| \frac{\partial u_1}{\partial y} \right|^a \mathrm{d}t + \epsilon^{c+hd} \int_0^{2\pi/\omega} \lambda_1^d \left| \frac{\partial u_1}{\partial y} \right|^c \mathrm{d}t + \text{higher order terms.} \tag{3.17}$$

Since the two terms in (3.17) must be of the same order in ϵ, we deduce that $a = c + hd$, i.e.

$$h = \frac{a-c}{d} > 0. \tag{3.18}$$

The dominant balance in equation (3.16) now depends on the relative sizes of the exponents a and h, and so three cases must be considered. When $h > a$, the right-hand side of (3.16) is dominant and so the leading-order behaviour must be an instantaneous balance between the build-up and breakdown terms. This is the 'fast-adjusting' behaviour described in section 3.1.4, and to leading order

the structure parameter must be given by $\lambda \sim \lambda_{\mathrm{eq}}(y,t)$, where λ_{eq} is defined by (3.10). Conversely, when $h < a$, the left-hand side of (3.16) is dominant and so the leading-order behaviour must be $\partial\lambda_1/\partial t = 0$. This is the 'slowly-adjusting' behaviour also described in section 3.1.4, and to leading order the structure parameter must be given by $\lambda \sim \lambda_{\mathrm{av}}(y)$, where λ_{av} is defined by (3.12). Between these two regimes of behaviour is a marginal case, $h = a$, in which all three terms in (3.16) are of comparable magnitude and we may expect the behaviour to be intermediate between fast- and slowly- adjusting behaviour. We shall consider each case in turn.

3.2.1.1 Fast-adjusting behaviour when $h > a$

The first case we consider is $h > a$, when, as we have seen, the structure parameter adjusts rapidly to the local conditions. In this case, λ_1 may be obtained from (3.16) as

$$\lambda_1(y,t) = \left|\frac{\partial u_1}{\partial y}\right|^h \tag{3.19}$$

and thus

$$\lambda(y,t) \sim 1 - \epsilon^h\lambda_1 = 1 - \epsilon^h\omega^{h/2}\left|\cos\left(\gamma y - \omega t - \frac{\pi}{4}\right)\right|^h \mathrm{e}^{-\gamma h y}. \tag{3.20}$$

As expected, the structure parameter approaches unity far from the wall but deviates from unity near the wall. Specifically, the first order deviation of λ from unity in (3.20) is proportional to $\mathrm{e}^{-\gamma h y}$, and so the characteristic width of the boundary layer is $1/(\gamma h)$. Within this exponential envelope, there is an oscillatory variation reflecting the wave-like behaviour of the underlying velocity field.

Also of interest is the shear stress at the wall, τ_{w}, given by

$$\tau_{\mathrm{w}} = \lambda \left.\frac{\partial u}{\partial y}\right|_{y=0} \sim -\epsilon\sqrt{\omega}\cos\left(\omega t + \frac{\pi}{4}\right). \tag{3.21}$$

At first order this is identical to the result for a Newtonian fluid.

3.2.1.2 Slowly-adjusting behaviour when $h < a$

The second case we consider is $h < a$, when, as we have seen, the structure parameter adjusts slowly to the local conditions. In this case, λ_1 may be obtained from (3.17) to give

$$\lambda \sim 1 - \epsilon^h \lambda_1(y) = 1 - \epsilon^h \omega^{h/2} \left[\frac{\Gamma\left(\frac{a}{2}+\frac{1}{2}\right)\Gamma\left(\frac{c}{2}+1\right)}{\Gamma\left(\frac{a}{2}+1\right)\Gamma\left(\frac{c}{2}+\frac{1}{2}\right)}\right]^{1/d} \mathrm{e}^{-\gamma h y}, \tag{3.22}$$

where Γ is the usual gamma function (Rile *et al.* 1998). As in the fast-adjusting case, equation (3.20), the deviation of λ from unity decays exponentially with distance from the wall, and the boundary layer has characteristic width $1/(\gamma h)$. However, in this case there is no oscillation superimposed on the envelope. Also as in the fast-adjusting case, the shear stress at the wall is given to first order by (3.21).

It can be shown that if the asymptotic expansion is carried to the next order then the structure parameter must be given by $\lambda \sim 1 - \epsilon^h \lambda_1(y) + \epsilon^a \lambda_2(y,t)$, where

$$\frac{\partial \lambda_2}{\partial t} = -\left|\frac{\partial u_1}{\partial y}\right|^a + \left|\frac{\partial u_1}{\partial y}\right|^c \lambda_1^d. \tag{3.23}$$

This result will be of use when we check the validity of these solutions in section 3.2.1.4.

3.2.1.3 Marginal behaviour when $h = a$

The third and final case we consider is the marginal case $h = a$, i.e. $(a-c)/d = a$, in which all terms in (3.8) are of comparable magnitude. Now, at leading order (3.16) becomes

$$-\frac{\partial \lambda_1}{\partial t} = -\left|\frac{\partial u_1}{\partial y}\right|^a + \left|\frac{\partial u_1}{\partial y}\right|^c \lambda_1^d, \tag{3.24}$$

where $u_1(y,t)$ is as before given by (3.15). Physically, we may expect this case to display behaviour intermediate between fast and slow adjustment.

We seek a solution to (3.24) that reflects the wavelike structure of the velocity field. Employing the Ansatz $\lambda_1 = f(y)l(\gamma y - \omega t)$, where the functions f and l are to be determined, equation (3.24) becomes

$$f\frac{\partial l}{\partial t} = (\mathrm{e}^{-\gamma y}\gamma\sqrt{2})^a \left|\cos(\gamma y - \omega t - \pi/4)\right|^a - f^d(\mathrm{e}^{-\gamma y}\gamma\sqrt{2})^c l^d \left|\cos(\gamma y - \omega t - \pi/4)\right|^c \tag{3.25}$$

and so

$$\frac{\partial l}{\partial t} = \frac{(\mathrm{e}^{-\gamma y}\gamma\sqrt{2})^a}{f}\left|\cos(\gamma y - \omega t - \pi/4)\right|^a - f^{d-1}(\mathrm{e}^{-\gamma y}\gamma\sqrt{2})^c l^d \left|\cos(\gamma y - \omega t - \pi/4)\right|^c. \tag{3.26}$$

We separate variables by requiring that the factors involving $f(y)$ in (3.26) cancel; thus

$$1 = \frac{\mathrm{e}^{-\gamma a y}(\gamma\sqrt{2})^a}{f} = f^{d-1}\mathrm{e}^{-\gamma c y}(\gamma\sqrt{2})^c \tag{3.27}$$

and so

$$f = \omega^{a/2}\mathrm{e}^{-\gamma a y}. \tag{3.28}$$

This reduces equation (3.25) to a nonlinear ODE for l, which may be written in terms of a new variable $\tau = \omega t - \gamma y + \pi/4$ as

$$\omega\frac{\mathrm{d}l}{\mathrm{d}\tau} + l^d \left|\cos(\tau)\right|^c = \left|\cos(\tau)\right|^a. \tag{3.29}$$

Equation (3.29) can easily be integrated numerically (see section 3.7.1) to obtain the waveform $l(\tau)$; periodicity typically becomes established after only a few periods, although the time taken to reach periodicity increases with ω. The asymptotic solution of λ then takes the form

$$\lambda(y,t) \sim 1 - \epsilon^h \lambda_1(y,t) = 1 - \epsilon^h \omega^{h/2} \mathrm{e}^{-\gamma h y} l(\omega t - \gamma y). \tag{3.30}$$

Note that, once again, the deviation of λ from unity is contained within an exponential envelope representing a boundary layer with characteristic width $1/(\gamma h) = 1/(\gamma a)$, and that once again the shear stress at the wall is given to first order by (3.21).

The solutions to (3.29) are interesting because they illustrate how the behaviour in this marginal case mediates between slowly- and fast-adjusting as ω is varied. In the limit $\omega \to 0$, equation (3.29) is satisfied by the instantaneous equilibrium

$$l(\tau) = |\cos(\tau)|^a \tag{3.31}$$

which corresponds to $\lambda \sim \lambda_{\mathrm{eq}}$. Meanwhile, in the limit $\omega \to \infty$, l must become a constant and we recover $\lambda \sim \lambda_{\mathrm{av}}$. Figure 3.1 illustrates the solutions for $l(\tau)$ for several values of ω. As ω is increased from zero, the variation of $l(\tau)$ is increasingly attenuated relative to (3.31), while it also displays an increasing phase lag and an increasingly non-sinusoidal waveform. Closely analogous behaviour can be seen in figure 2 of Shadrina (1978).

3.2.1.4 *A posteriori* estimate of the validity of the asymptotic solutions

The asymptotic solutions described in the preceding subsections have been obtained in the limit of small-amplitude oscillations, $\epsilon \to 0$. However, they also depend on the additional independent parameter ω, which represents the di-

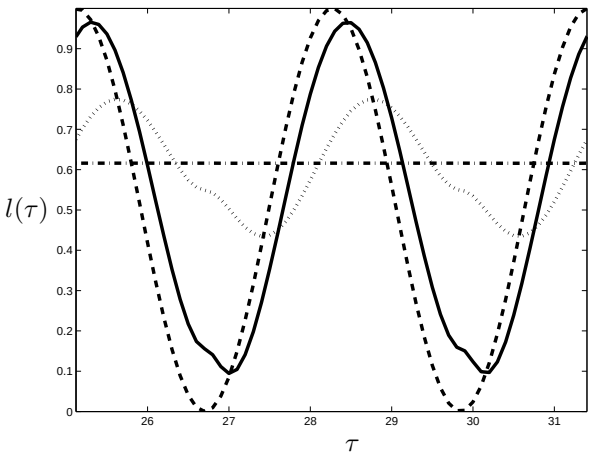

Figure 3.1: Periodic solutions to (3.29) for the structure waveform $l(\tau)$ with $a = 2$, $b = 1$, $c = 1$, $d = 1/2$ and $\omega = 0$ (dashed; equation (3.31)); $\omega = 0.1$ (solid); $\omega = 0.5$ (dotted); $\omega = 1000$ (dot-dashed).

mensionless frequency or Deborah number. It is therefore useful to obtain *a posteriori* estimates of the validity of these solutions when ω is not necessarily of order unity.

It can be shown from (3.15) that $|\partial u/\partial y| = O(\omega^{1/2}\epsilon)$. In the fast-adjusting regime, (3.20) yields the scalings $\lambda = O(1)$, $1 - \lambda = O(\omega^{h/2}\epsilon^h)$ and $\partial\lambda/\partial t = O(\omega^{1+h/2}\epsilon^h)$. From these, the validity condition for fast adjustment,

$$\left|\frac{\partial \lambda}{\partial t}\right| \ll \left|\frac{\partial u}{\partial y}\right|^a \lambda^b \sim \left|\frac{\partial u}{\partial y}\right|^c (1-\lambda)^d, \tag{3.32}$$

corresponds to

$$\epsilon^h \omega^{1+h/2} \ll \epsilon^a \omega^{a/2}, \qquad \text{i.e.} \qquad \epsilon^{h-a}\omega^{1+(h-a)/2} \ll 1. \tag{3.33}$$

Fast-adjusting behaviour can therefore be expected in the asymptotic limits of either small oscillations, $\epsilon \to 0$, or slow oscillations, $\omega \to 0$.

In the slowly-adjusting regime, equation (3.22) yields the scalings $\lambda = O(1)$ and $1 - \lambda = O(\omega^{h/2}\epsilon^h)$. To estimate the magnitude of $\partial\lambda/\partial t$ we need to consider

the next order in ϵ. Integrating equation (3.23) with respect to ωt implies that $\omega\lambda_2 = O(\omega^{a/2})$; thus the validity condition for the asymptotic solution in the slowly-adjusting case, namely

$$\epsilon^h \lambda_1 \gg \epsilon^a \lambda_2 \tag{3.34}$$

corresponds to

$$\epsilon^h \omega^{h/2} \gg \epsilon^a \omega^{a/2-1}, \qquad \text{i.e.} \qquad \epsilon^{h-a} \omega^{1+(h-a)/2} \gg 1, \tag{3.35}$$

which is exactly the complement of the condition (3.33) for fast adjustment. Since $h - a < 0$ in this regime, this condition always corresponds to small oscillations, $\epsilon \to 0$, but depending on the relative sizes of a and h it may be obtained when the oscillations are fast or when they are slow.

Figure 3.2 illustrates the parameter regimes in which the present asymptotic analysis suggests fast-adjusting, slowly-adjusting and hysteretic behaviour. To avoid ambiguity, we will henceforth refer to the parameter regime $a > c$, $h > a$ as regime T1 and to the parameter regime $a > c$, $h < a$ as regime T2; we will reserve the terms 'fast-adjusting' and 'slowly-adjusting' for the regimes, depending also on ϵ and ω, in which the solutions display these behaviours. (The fast-adjusting regime is a subset of T1 and the slowly-adjusting regime is a subset of T2.) When the system is neither fast- nor slowly-adjusting, we may expect its behaviour in general to be hysteretic, as shown in figure 3.2.

3.2.2 Numerical results for finite-amplitude wall oscillations

We now compare the asymptotic solutions for velocity, structure parameter and shear stress at the wall with numerical solutions obtained using the finite-

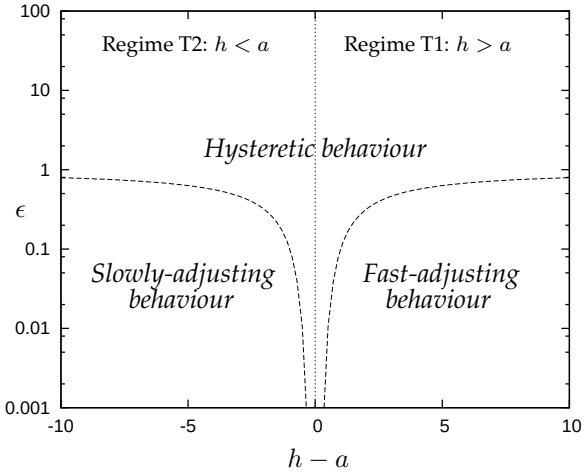

Figure 3.2: Outline of regimes of validity for the asymptotic solutions for a thixotropic fluid. The dashed lines represent indicative regime boundaries for $\omega = 1$: $\epsilon^{h-a} = 10$ for $h - a < 0$ and $\epsilon^{h-a} = 0.1$ for $h - a > 0$, where $h = (a - c)/d$. The dotted line represents the marginal regime $h = a$.

element package Comsol 3.5a. A finite numerical domain $0 \leq y \leq y_{\max}$ was used, with a domain length of $y_{\max} = 10$ unless otherwise stated. The initial conditions were $u(y, 0) = 0$ and $\lambda(y, 0) = 1$ unless otherwise stated. A zero-velocity condition was applied at $y = y_{\max}$; in general this had a negligible effect on the solution. The mesh comprised 240 equally-spaced grid points (except in the calculations with $\epsilon = 10$, where 960 grid points were employed to resolve the behaviour close to the wall), and the numerical relative tolerance was 10^{-6}. The results reported here were robust to further refinement of these parameters. Run-times ranged from tens of minutes to several hours on a desktop PC.

3.2.2.1 Regime T1: $h > a$

To illustrate the behaviour in regime T1, in which the structure parameter is fast-adjusting for small ϵ, we take $a = 2$, $b = 1$, $c = 1$ and $d = 1/3$, giving $h = 3$. We also set $\omega = 1$ so that the condition (3.33) is easily satisfied.

We first consider small-amplitude oscillations, $\epsilon = 0.01$. Figures 3.3 a and 3.3 b show snapshots of the velocity $u(y, t)$ and structure parameter $\lambda(y, t)$ at equally spaced times during a period. (Note that since the evolution of λ is

driven by $|\partial u/\partial y|$, it has period π/ω in contrast to the period $2\pi/\omega$ for u; we have therefore plotted λ at more frequent intervals than u.) The first snapshot is taken at $t = 100$, by which time the system has adjusted to an essentially periodic state. The numerical solution (solid lines) and the asymptotic solution (dashed lines) are almost indistinguishable for all values of y. As the structure parameter deviates only very weakly from unity (figure 3.3 b), the velocity field is essentially identical to the Newtonian solution (1.21), and decays exponentially away from the wall, over a characteristic distance $\gamma^{-1} = \sqrt{2}$. It is clear that the perturbations to the structure parameter decay away from the wall over a shorter distance than the velocity, in accordance with the prediction of equation (3.20) that they should decay over a characteristic distance $(\gamma h)^{-1} = \sqrt{2}/3$. There is also evidence in figure 3.3 b that the structure parameter λ lags slightly behind λ_{eq} at some stages of the oscillation.

To investigate the behaviour for larger oscillations, the amplitude was increased to $\epsilon = 1$. Figures 3.3 c and 3.3 d show snapshots of the velocity $u(y,t)$ and structure parameter $\lambda(y,t)$. Some deviation can now be seen from the fast-adjusting asymptotic solution, as the response time of the structure is no longer negligible. The variation of the structure parameter λ (figure 3.3 d) is significantly attenuated relative to the instantaneous equilibrium λ_{eq} predicted by the asymptotic solution, and may be described as oscillation around an average equilibrium value. Since λ is significantly lower than unity, the velocity (figure 3.3 c) decays more rapidly with distance from the wall than is predicted by the asymptotic solution (3.15), in which $\lambda \sim 1$. However, the deviation of the structure parameter from unity is significantly overestimated by the asymptotic solution (3.20), because shear rates, and thus structure breakdown rates, are generally lower than predicted by the asymptotic solution (3.15).

When the amplitude is increased further to $\epsilon = 10$ (figures 3.3 e and f), these

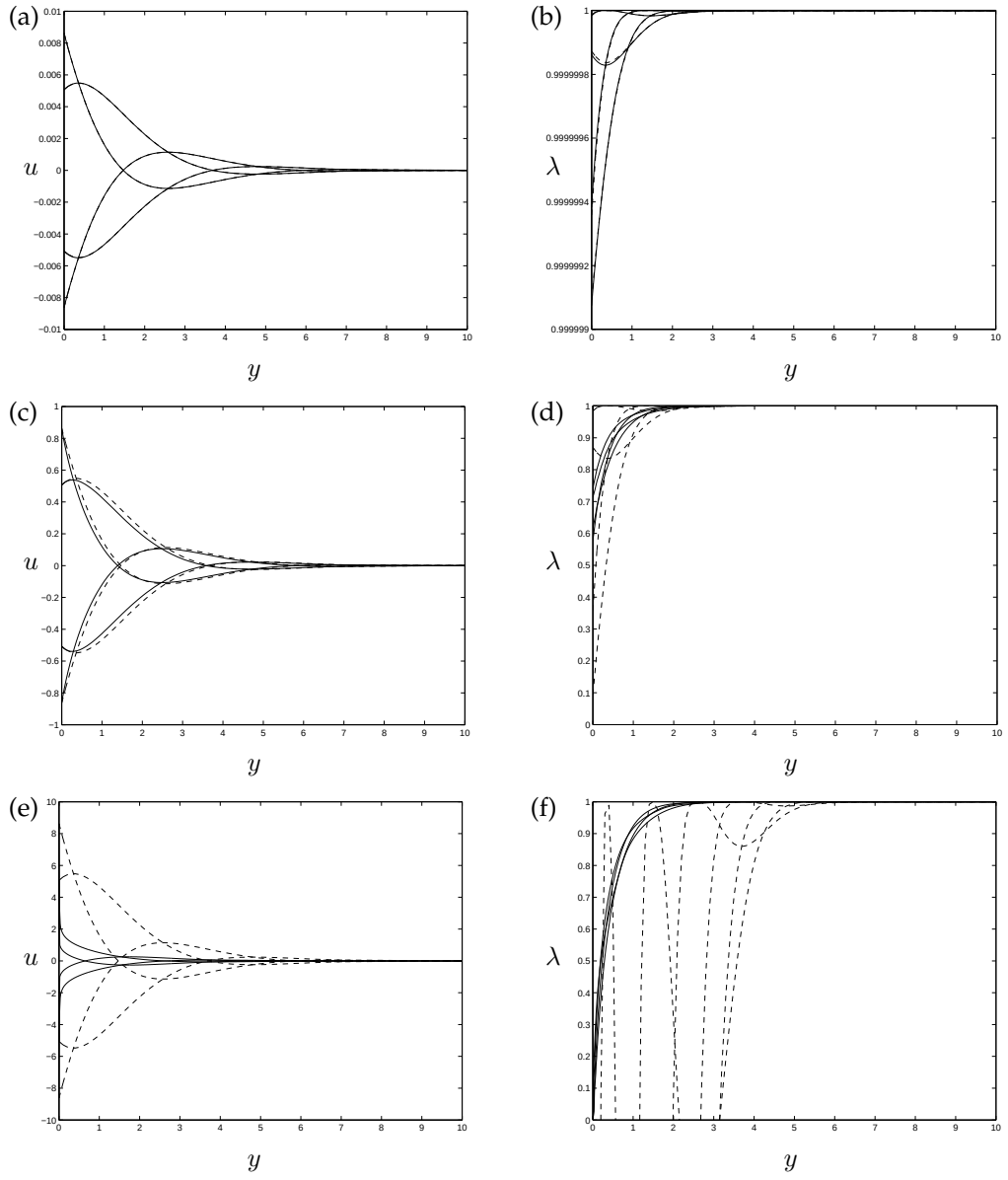

Figure 3.3: Thixotropic regime T1 ($h > a$): snapshots of the numerical solutions (solid lines) and fast-adjusting asymptotic solutions (dashed lines) with $a = 2$, $b = 1$, $c = 1$, $d = 1/3$, $\omega = 1$ and (a, b) $\epsilon = 0.01$; (c, d) $\epsilon = 1$; (e, f) $\epsilon = 10$. Plots (a), (c) and (e) show the velocity $u(y, t)$ at $t = 100 + n\pi/2$ for $n = 0$, 1, 2 and 3; the asymptotic solution is given by (3.15). Plots (b), (d) and (f) show the structure parameter $\lambda(y, t)$ at $t = 100 + n\pi/4$ for $n = 0$, 1, 2, 3; the asymptotic solution is given by (3.20).

trends are still more strongly pronounced, and the asymptotic description for small ϵ is clearly no longer valid. The structure has almost completely broken down near the wall (figure 3.3 f), and the result of this very low viscosity is that the oscillations in u die out very rapidly (figure 3.3 e). The effect of this on the shear stress at the wall will be discussed in section 3.2.2.3.

3.2.2.2 Regime T2: $h < a$

To illustrate the behaviour in regime T2, in which the structure parameter is slowly-adjusting for small ϵ, we take $a = 2$, $b = 1$, $c = 1$ and $d = 1$, giving $h = 1$. We again set $\omega = 1$ so that the condition (3.35) is easily satisfied.

We first consider small-amplitude oscillations, $\epsilon = 0.01$. Figure 3.4 a shows snapshots of the velocity $u(y, t)$ at equally spaced times during a period. The first snapshot is taken at $t = 100$, by which time the velocity has adjusted to an essentially periodic state. The numerical solution (solid lines) and the asymptotic solution (dashed lines) are indistinguishable for all values of y. As the structure parameter again deviates only very weakly from unity (figure 3.4 b), the velocity field is again essentially identical to the Newtonian solution (1.21).

Although the velocity adjusts rapidly to an effectively periodic state, the structure parameter takes longer to adjust. Figure 3.4 b shows plots of $\lambda(y, t)$ at times ranging from $t = 100$ to $t = 500$. Because the structure parameter varies slowly, it not only remains approximately constant throughout a period but also takes many periods to adjust towards its eventual asymptotic state (the dashed line in figure 3.4 b). The adjustment towards this asymptotic state is fastest close to the wall where shear rates are highest, and is correspondingly slower as shear rates decay exponentially away from the wall.

To investigate the behaviour for larger oscillations, the amplitude was again increased to $\epsilon = 1$. Figures 3.4 c and d show snapshots of the velocity $u(y, t)$

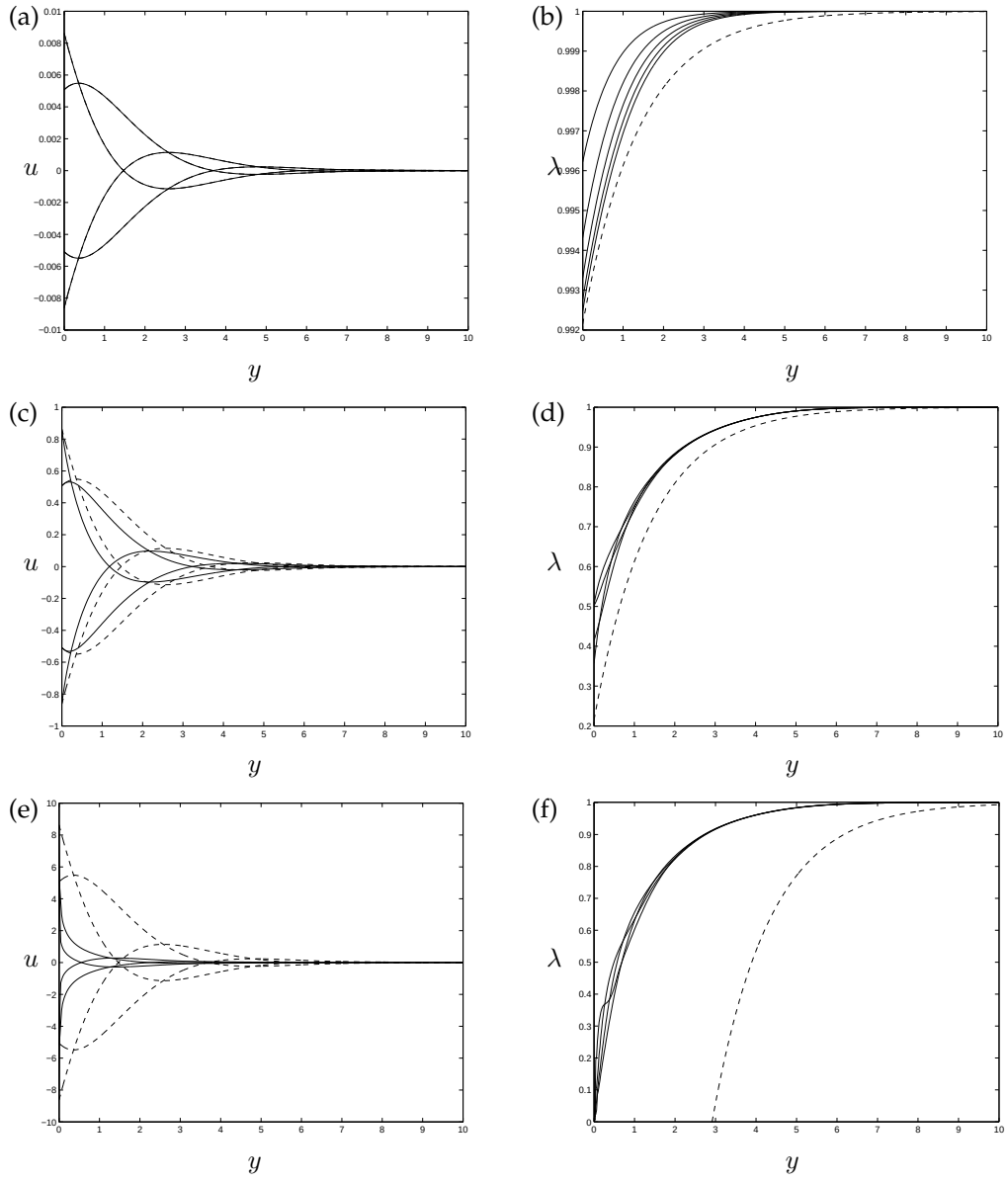

Figure 3.4: Thixotropic regime T2 ($h < a$): snapshots of the numerical solutions (solid lines) and slowly-adjusting asymptotic solutions (dashed lines) with $a = 2$, $b = 1$, $c = 1$, $d = 1$, $\omega = 1$ and (a, b) $\epsilon = 0.01$; (c, d) $\epsilon = 1$; (e, f) $\epsilon = 10$. Plots (a), (c) and (e) show the velocity $u(y, t)$ at $t = 100 + n\pi/2$ for $n = 0$, 1, 2 and 3; the asymptotic solution is given by (3.15). Plot (b) shows the structure parameter $\lambda(y, t)$ at $t = 100$, 200, 300, 400 and 500, while plots (d) and (f) show the structure parameter $\lambda(y, t)$ at $t = 100 + n\pi/4$ for $n = 0$, 1, 2, 3; the asymptotic solution is given by (3.22).

and structure parameter $\lambda(y,t)$, after the system has adjusted to an essentially periodic state. Some deviation from the asymptotic solution can now be seen. The structure parameter λ (figure 3.4 d) is nearly independent of t but strongly dependent on y, and oscillates slightly around an average equilibrium value. As in the regime T1 (figures 3.3 c and d), $\lambda(y,t)$ is significantly lower than unity, so the velocity (figure 3.4 c) decays more rapidly with distance from the wall than is predicted by the asymptotic solution (3.15), in which $\lambda \sim 1$. However, the deviation of the structure parameter from unity is again significantly overestimated by the asymptotic solution (3.22).

When the amplitude is increased further to $\epsilon = 10$ (figures 3.4 e and f), the asymptotic description for small ϵ is clearly no longer valid. Except near the wall, however, the structure parameter still varies only weakly throughout a period (figure 3.4 f) so the system still shows essentially slowly-adjusting behaviour. What is now conspicuous is that the structure has almost completely broken down near the wall, and the result of this very low viscosity is that the oscillations in u die out very rapidly (figure 3.4 e). This is again rather similar to the behaviour in regime T1: indeed, with increasing ϵ the distinction between these regimes becomes increasingly blurred.

3.2.2.3 Shear stress at the wall

It is also of interest to examine the shear stress at the wall, as this is one of the most readily measured quantities in most experimental configurations. Figures 3.5 a and 3.5 b show the shear stress $\tau_{\mathrm{w}}(t)$, normalised by the asymptotic scaling factor ϵ, for regimes T1 and T2 respectively.

In each case, the variation for small ϵ is sinusoidal as predicted by the asymptotic solution (3.21). As ϵ is increased, the variation becomes slightly less sinusoidal, and the scaling of τ_{w} with ϵ also departs from strict proportionality. There

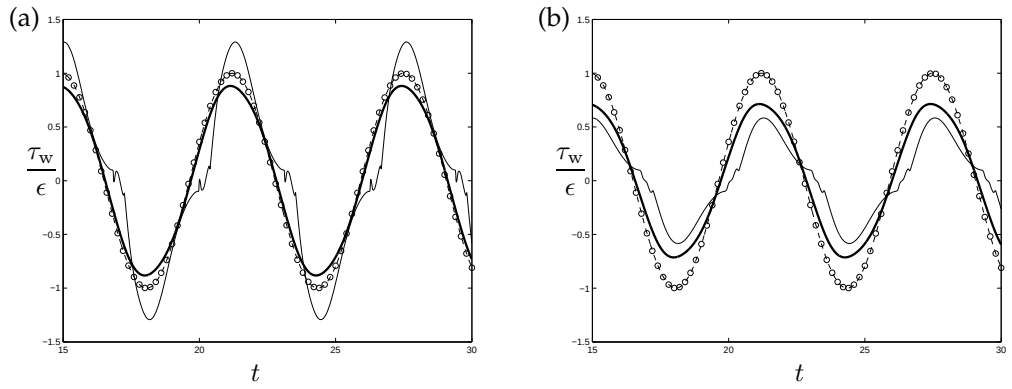

Figure 3.5: Normalised shear stress at the wall, $\tau_w(t)/\epsilon$, with $a = 2$, $b = 1$, $c = 1$ and $\omega = 1$ and (a) $d = 1/3$, (b) $d = 1$. Figure (a) is the shear stress for regime T1 ($h > a$) and figure (b) is the shear stress for regime T2 ($h < a$). The circles represent the asymptotic solution; lines represent the numerical solutions for $\epsilon = 0.01$ (dashed); $\epsilon = 1$ (thick solid); $\epsilon = 10$ (thin solid).

is a competition between the decreasing values of λ at the wall and the increasing shear rates, both of which contribute to τ_w. In regime T2 (figure 3.5 b) the former dominates and the rescaled shear stress τ_w/ϵ decreases with increasing ϵ. In regime T1 (figure 3.5 a) the competition is less straightforward: at first the rescaled shear stress decreases with increasing ϵ, but as ϵ is increased further the high shear rates near the wall come to dominate and τ_w/ϵ increases again. In all these cases, however, the amplitude of τ_w remains of order ϵ, despite the very strong deviation of both u and λ from the asymptotic solution.

When ϵ is increased to 10, rapid variations of τ_w occur at times when the shear rate is close to zero (figures 3.5 a and b). In order to explore this behaviour, in figure 3.6 we plot τ_w/ϵ along with the structure parameter λ and the shear rate, also evaluated at the wall. Note that a normalised shear rate $\dot{\gamma}^* = (\partial u/\partial y)/\max(\partial u/\partial y)$ has been plotted to allow all three quantities to appear on the same axes.

In general, the strong oscillation means that λ is very low near to the wall.

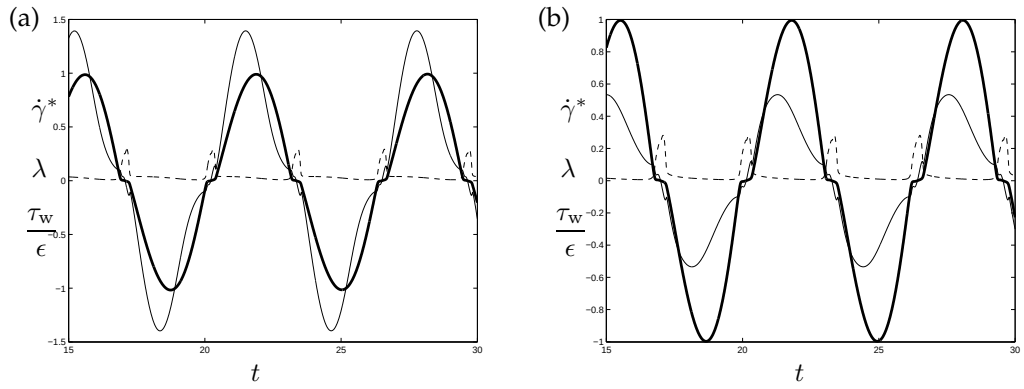

Figure 3.6: Normalised shear stress, normalised shear rate and structure parameter evaluated at the wall with $a = 2$, $b = 1$, $c = 1$ and $\omega = 1$ and (a) $d = 1/3$, (b) $d = 1$. Figure (a) shows regime T1 ($h > a$) and figure (b) shows regime T2 ($h < a$). Lines represent the numerical solutions for τ_w/ϵ (thin solid); $\dot{\gamma}^* = (\partial u/\partial y)/\max(\partial u/\partial y)$ (thick solid); λ (dashed).

Since λ also sets the momentum diffusivity, this means that there is generally a high-shear region near the wall. Throughout most of a period, then, λ is low and thus $\partial u/\partial y$ is large; in fact throughout this phase of the oscillation λ is gradually decaying. However, because the wall oscillates, there must come a point in the cycle when $\partial u/\partial y$ becomes close to zero. At this point, a feedback process occurs: λ increases, thus increasing the momentum diffusivity and further reducing the shear rate. The result of this is that λ grows rapidly, while $\partial u/\partial y$ is held close to zero for an extended period (the 'plateau' which can be seen every time the dashed line in figures 3.5 a and b crosses the axis). Eventually, though, the continued increase of u at the wall causes the shear rate to increase again; increasing shear decreases λ, which in turn further increases shear. Thus λ decreases rapidly until the phase of low λ and high shear resumes. From figures 3.5 a and b it is apparent that the rapid variations in τ_w are the signature of this rather complicated interaction between structure and shear rate. We will see this signature in a different form in section 3.4.

A tentative connection may be made here with the work of Balmforth *et al.* (2009), who attributed to thixotropy some of the discrepancies between their experimental and theoretical results. Specifically, they found that the surface and wall velocities were less closely coupled than predicted, and suggested that this might be due to thixotropic effects occurring at critical points in the oscillation. In figure 3.5 a it is apparent that during the periods of rapid variation the magnitude of τ_{w} is reduced relative to the fast-adjusting solution, and this suggests that thixotropic effects can indeed weaken the coupling between the fluid and the wall as suggested by Balmforth *et al.* (2009).

3.2.2.4 Marginal regime $h = a$

Finally, to illustrate the behaviour in the marginal regime $h = a$ we take $a = 2$, $b = 1$, $c = 1$ and $d = 1/2$, giving $h = a = 2$. As in the two previously considered regimes, we set $\omega = 1$.

We first consider small-amplitude oscillations with $\epsilon = 0.01$. The velocity $u(y, t)$ (figure 3.7 a) behaves qualitatively in the same way as in regimes T1 and T2 (figures 3.3 a and 3.4 a). Although the structure parameter $\lambda(y, t)$ (figure 3.7 b) varies throughout a period, its variation is relatively weak, and qualitatively resembles that in regime T2 for larger values of ϵ (e.g. figure 3.4 d).

Increasing ϵ further, first to $\epsilon = 1$ (figures 3.7 c and d) and then to $\epsilon = 10$ (figures 3.7 e and f) changes the behaviour quantitatively rather than qualitatively. As in both the previously-considered regimes, the structure breaks down substantially at the wall, with a corresponding very rapid decrease in the amplitude of the velocity variation with distance from the wall.

The shear stress at the wall τ_{w} (figure 3.8) is also similar to that in the other two regimes: as in the 'fast-adjusting' regime (figure 3.5 a) the competition between decreasing structure and increasing shear rates at the wall is rather

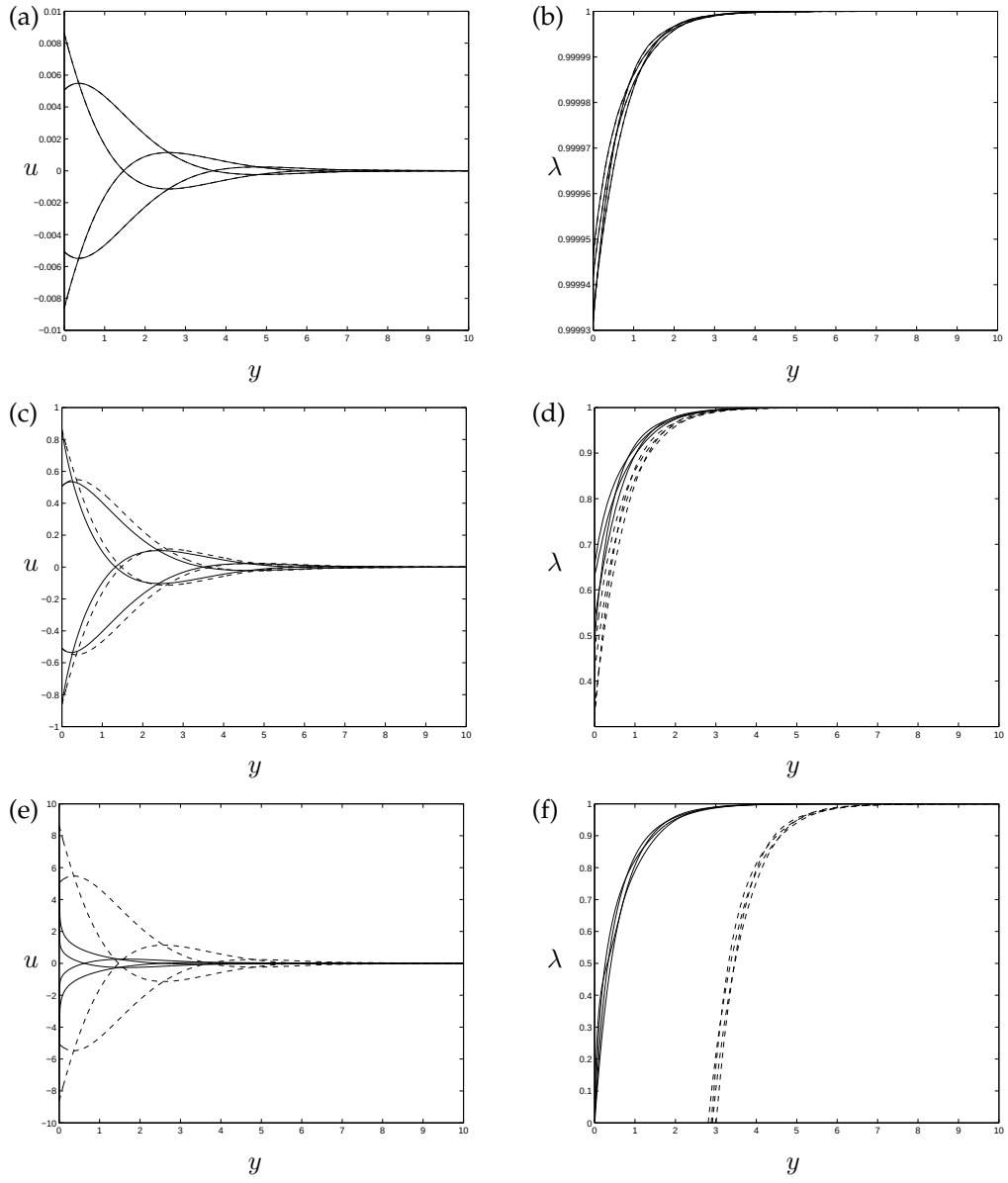

Figure 3.7: Thixotropic marginal regime ($h = a$): snapshots of the numerical solutions (solid lines) and marginal asymptotic solutions (dashed lines) with with $a = 2$, $b = 1$, $c = 1$, $d = 1/2$, $\omega = 1$ and (a, b) $\epsilon = 0.01$; (c, d) $\epsilon = 1$; (e, f) $\epsilon = 10$. Plots (a), (c) and (e) show the velocity $u(y,t)$ at $t = 100 + n\pi/2$ for $n = 0$, 1, 2 and 3; the asymptotic solution is given by (3.15). Plots (b), (d) and (f) show the structure parameter $\lambda(y,t)$ at $t = 100 + n\pi/4$ for $n = 0$, 1, 2, 3; the asymptotic solution is given by (3.30).

finely balanced, so that although the variation of $\tau_{\mathrm{w}}(t)$ deviates from the sinusoidal asymptotic solution (3.21) its amplitude continues to scale roughly with ϵ. Again, when $\epsilon = 10$ we see rapid variations as the shear rate approaches zero. The reasons for these are the same as in regimes T1 and T2 (figure 3.5).

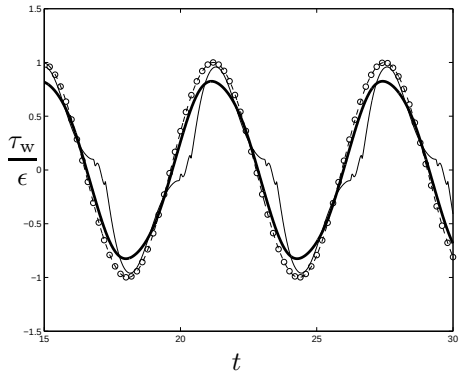

Figure 3.8: Thixotropic marginal regime: normalised shear stress at the wall, $\tau_{\mathrm{w}}(t)/\epsilon$, with $a = 2$, $b = 1$, $c = 1$, $d = 1/2$ and $\omega = 1$. The circles represent the asymptotic solution (3.21); lines represent the numerical solutions for $\epsilon = 0.01$ (dashed); $\epsilon = 1$ (thick solid); $\epsilon = 10$ (thin solid).

3.3 Antithixotropic behaviour, $a < c$

We now consider the case in which the rheology is antithixotropic, $a < c$. As in the thixotropic case, we will first develop asymptotic solutions in the limit of small-amplitude wall oscillations, $\epsilon \to 0$, and then extend these numerically to larger values of ϵ.

3.3.1 Asymptotic solutions for small-amplitude wall oscillations

For the rates of structural buildup and breakdown to be comparable in magnitude in the limit $\epsilon \to 0$, the fluid must be highly unstructured, with λ close to

zero everywhere. We therefore seek asymptotic solutions of the form

$$u(y,t) = \epsilon u_1(y,t) + o(\epsilon) \qquad \text{and} \qquad \lambda(y,t) = \epsilon^\beta \Lambda_1(y,t) + o(\epsilon^\beta), \tag{3.36}$$

where the exponent $\beta > 0$ remains to be determined. The boundary conditions are the same as in the thixotropic case, $u_1(0,t) = \cos(\omega t)$ and $u_1 \to 0$ as $y \to 0$. Note that because of the antithixotropic rheology we may also expect Λ_1 to be largest close to the wall where shear rates are highest, and to tend to zero as $y \to \infty$.

Substituting the expansion (3.36) into equation (3.7) and retaining only leading-order terms yields

$$\frac{\partial u_1}{\partial t} = \epsilon^\beta \frac{\partial}{\partial y}\left(\Lambda_1 \frac{\partial u_1}{\partial y}\right). \tag{3.37}$$

To eliminate ϵ from this equation we rescale using $y = \epsilon^{\beta/2}\hat{y}$, where $\hat{y}$ is of order unity [1], yielding

$$\frac{\partial u_1}{\partial t} = \frac{\partial}{\partial \hat{y}}\left(\Lambda_1 \frac{\partial u_1}{\partial \hat{y}}\right). \tag{3.38}$$

Substituting the expansion (3.36) into equation (3.8) yields

$$\epsilon^\beta \frac{\partial \Lambda_1}{\partial t} = -\epsilon^{a(1-\beta/2)+b\beta}\left|\frac{\partial u_1}{\partial \hat{y}}\right|^a \Lambda_1^b + \epsilon^{c(1-\beta/2)}\left|\frac{\partial u_1}{\partial \hat{y}}\right|^c + \text{higher order terms.} \tag{3.39}$$

Balancing powers of ϵ on the right hand side yields

$$\beta = \frac{2(c-a)}{2b + (c-a)} > 0. \tag{3.40}$$

[1] Note that in this section only, the caret does not signify a dimensional quantity.

This simplifies equation (3.39) to

$$\epsilon^{\nu}\frac{\partial \Lambda_1}{\partial t} = -\left|\frac{\partial u_1}{\partial \hat{y}}\right|^a \Lambda_1^b + \left|\frac{\partial u_1}{\partial \hat{y}}\right|^c + \text{higher order terms}, \tag{3.41}$$

where

$$\nu = \frac{2(c-a-bc)}{2b+c-a}. \tag{3.42}$$

Integrating (3.39) over a period and applying the periodicity condition (3.9) then yields

$$0 = -\int_0^{2\pi/\omega} \Lambda_1^b \left|\frac{\partial u_1}{\partial \hat{y}}\right|^a \mathrm{d}t + \int_0^{2\pi/\omega} \left|\frac{\partial u_1}{\partial \hat{y}}\right|^c \mathrm{d}t + \text{higher order terms}. \tag{3.43}$$

The dominant balance in equation (3.41) now depends on the sign of the exponent ν, and so three cases must be considered. When $\nu > 0$, the right-hand side of (3.41) is dominant and so the leading-order behaviour must be an instantaneous balance between the build-up and breakdown terms. This is the 'fast-adjusting' regime described in section 3.1.4, and to leading order the structure parameter must be given by $\lambda \sim \lambda_{\mathrm{eq}}(y,t)$, where λ_{eq} is defined by (3.10). Conversely, when $\nu < 0$, the left-hand side of (3.41) is dominant and so the leading-order behaviour must be $\partial\Lambda_1/\partial t = 0$. This is the 'slowly-adjusting' regime also described in section 3.1.4, and to leading order the structure parameter must be given by $\lambda \sim \lambda_{\mathrm{av}}(y)$, where λ_{av} is defined by (3.12). Between these two regimes is a marginal case, $\nu = 0$, in which all three terms in (3.41) are of comparable magnitude and we may expect the behaviour to be intermediate between fast- and slowly- adjusting behaviour. We shall consider each case in turn.

3.3.1.1 Fast-adjusting behaviour when $\nu > 0$

The first case we consider is $\nu > 0$, when, as we have seen, the structure parameter adjusts rapidly to the local conditions. In this case, Λ_1 may be obtained from (3.41) as

$$\Lambda_1(y,t) = \left|\frac{\partial u_1}{\partial \hat{y}}\right|^{(c-a)/b} \tag{3.44}$$

and thus from (3.38)

$$\frac{\partial u_1}{\partial t} = \frac{\partial}{\partial \hat{y}}\left(\left|\frac{\partial u_1}{\partial \hat{y}}\right|^{(c-a)/b}\frac{\partial u_1}{\partial \hat{y}}\right). \tag{3.45}$$

Equation (3.45) is exactly the governing equation for a power-law fluid with power-law index $n = (b + c - a)/b > 1$ and so the solution for u_1 is identical to that for a shear-thickening power-law fluid seen in section 2.2.2.

Recall from section 2.2.2 that the most distinctive feature of the Stokes problem in a shear-thickening power-law fluid is that the boundary layer is of finite width. Also, even in the limit $\epsilon \to 0$, the waveforms of the velocity are non-sinusoidal, unlike those for Newtonian and thixotropic fluids, and so the boundary condition at $y = 0$ is not satisfied precisely by the asymptotic solution. The velocity decays algebraically towards the edge of the boundary layer, with exponent $\alpha = (2b + c - a)/(c - a)$.

Also of interest is the shear stress at the wall, τ_{w}, given, to first order, by

$$\tau_{\mathrm{w}} \sim \epsilon^{1+\beta/2}\left|\frac{\partial u_1}{\partial y}\right|^{(c-a)/b}\frac{\partial u_1}{\partial y}. \tag{3.46}$$

We will plot this quantity in section 3.3.2.3.

3.3.1.2 Slowly-adjusting behaviour when $\nu < 0$

The second case we consider is $\nu < 0$, when, as we have seen, the structure parameter adjusts slowly to the local conditions. In this case, Λ_1 may be obtained from (3.43) as

$$\Lambda_1^b = \frac{\displaystyle\int_0^{2\pi/\omega} \left|\frac{\partial u_1}{\partial \hat{y}}\right|^c \mathrm{d}t}{\displaystyle\int_0^{2\pi/\omega} \left|\frac{\partial u_1}{\partial \hat{y}}\right|^a \mathrm{d}t}. \tag{3.47}$$

In order to solve equations (3.38) and (3.47), we introduce an Ansatz motivated by the algebraic decay of velocity seen in the power-law case, namely

$$u_1 = c_0 Y^\alpha \cos(\phi_0 \log(Y/\hat{y}_0) - \omega t), \tag{3.48}$$

where $Y = \hat{y}_0 - \hat{y}$ for some $\hat{y}_0$ and where $c_0 = \hat{y}_0^{-\alpha}$ to satisfy the boundary condition at $\hat{y} = 0$. This solution is valid for $Y > 0$, i.e. in the finite interval $0 < \hat{y} < \hat{y}_0$.

Substituting the Ansatz (3.48) into equation (3.47) yields an expression for Λ_1,

$$\Lambda_1^b = \left(c_0 Y^{\alpha-1}(\alpha^2 + \phi_0^2)^{1/2}\right)^{c-a} D_0, \tag{3.49}$$

where

$$D_0 = \frac{\displaystyle\int_0^{2\pi/\omega} |\cos(\omega t)|^c \,\mathrm{d}t}{\displaystyle\int_0^{2\pi/\omega} |\cos(\omega t)|^a \,\mathrm{d}t} = \frac{\displaystyle\int_0^{2\pi} |\cos(\tau)|^c \,\mathrm{d}\tau}{\displaystyle\int_0^{2\pi} |\cos(\tau)|^a \,\mathrm{d}\tau}, \tag{3.50}$$

and so

$$\Lambda_1 = \left[D_0 \left(c_0(\alpha^2 + \phi_0^2)^{1/2}\right)^{c-a}\right]^{1/b} Y^2. \tag{3.51}$$

To find the constants α, ϕ_0 and c_0, equation (3.48) is substituted into (3.38) and

$$\alpha = \frac{2b + c - a}{c - a} \tag{3.52}$$

is found by balancing the powers of Y, while ϕ_0 and c_0 are found by balancing the coefficients of the $\sin$ and $\cos$ terms, ϕ_0 and c_0 are omitted for brevity. The decay rate α is the same as for the fast-adjusting antithixotropic fluid.

The shear stress at the wall is given, to leading order, by

$$\tau_{\mathrm{w}} \sim -\epsilon^{1+\beta/2} D_0^{1/b} \left(c_0 \hat{y}_0^{\alpha-1}\right)^{(c-a+b)/b} (\alpha^2+\phi_0^2)^{(c-a)/2b} \left[\alpha\cos(\omega t)+\phi_0\sin(\omega t)\right]. \tag{3.53}$$

It is straightforward to demonstrate that if the asymptotic expansion is carried to the next order then the structure parameter must be given by $\lambda \sim \epsilon^{\beta}\Lambda_1(y) + \epsilon^{2bc/(2b+c-a)}\Lambda_2(y,t)$, where

$$\frac{\partial \Lambda_2}{\partial t} = -\left|\frac{\partial u_1}{\partial \hat{y}}\right|^a \Lambda_1^b + \left|\frac{\partial u_1}{\partial \hat{y}}\right|^c. \tag{3.54}$$

This result will be of use when we check the validity of these solutions in section 3.3.1.4.

3.3.1.3 Marginal behaviour when $\nu = 0$

The third and final case we consider is the marginal case $\nu = 0$, in which all three terms in (3.8) are of comparable magnitude. Now, at leading order (3.39) becomes

$$\frac{\partial \Lambda_1}{\partial t} = -\left|\frac{\partial u_1}{\partial \hat{y}}\right|^a \Lambda_1^b + \left|\frac{\partial u_1}{\partial \hat{y}}\right|^c. \tag{3.55}$$

Physically, we may expect the behaviour to be intermediate between fast and slow adjustment. In order to solve equations (3.38) and (3.55), two Ansätze are introduced, motivated by the behaviour of the fast- and slowly-adjusting cases,

$$u_1 = Y^{\alpha} f(\tau) \quad \text{and} \quad \Lambda_1 = Y^2 g(\tau), \tag{3.56}$$

where $Y = \hat{y}_0 - \hat{y}$ with $0 \leq \hat{y} \leq \hat{y}_0$, $\tau = \phi_0 \log(Y) + \omega t + \tau_0$, τ_0 is a phase difference, and the functions $f(\tau)$ and $g(\tau)$, as well as the constant ϕ_0, are to be determined. Substituting equations (3.56) into the governing equations and balancing the powers of y yields $\alpha = 1 + 2/c$, which in this case is identical to (3.52), together with the coupled equations

$$\omega \frac{\mathrm{d}g}{\mathrm{d}\tau} = -\left|\alpha f + \phi_0 \frac{\mathrm{d}f}{\mathrm{d}\tau}\right|^a g^b + \left|\alpha f + \phi_0 \frac{\mathrm{d}f}{\mathrm{d}\tau}\right|^c \tag{3.57}$$

and

$$\omega \frac{\mathrm{d}f}{\mathrm{d}\tau} = \left(2g + \phi_0 \frac{\mathrm{d}g}{\mathrm{d}\tau}\right)\left(\alpha f + \phi_0 \frac{\mathrm{d}f}{\mathrm{d}\tau}\right) + g\left[\alpha(\alpha-1)f + \phi_0(2\alpha-1)\frac{\mathrm{d}f}{\mathrm{d}\tau} + \phi_0^2 \frac{\mathrm{d}^2 f}{\mathrm{d}\tau^2}\right]. \tag{3.58}$$

These ordinary differential equations must be integrated numerically, subject to the periodicity constraint $f(\tau) = f(\tau + 2\pi)$ and $g(\tau) = g(\tau + 2\pi)$ for all τ.

If the velocity imposed at the wall is precisely of the form $f(\tau)$ and has amplitude ϵ, so the oscillation has dimensionless amplitude 1 at $y = 0$, then $\hat{y}_0$ must be given by

$$(\hat{y}_0 - 0)^\alpha f_{\max} = 1, \quad \text{i.e.} \quad \hat{y}_0 = f_{\max}^{-1/\alpha}, \tag{3.59}$$

where $f_{\max} = \max_\tau f(\tau)$. We carry out numerical integrations to find f and g (see section 3.7.2). These functions always converge to a periodic solution, and the parameter ϕ_0 is determined by a shooting method in order to set the period to be 2π as required.

The shear stress at the wall is given, to leading order, by

$$\tau_{\mathrm{w}} \sim -\epsilon^{1+\beta/2} \hat{y}_0^{2\alpha-1} g(\tau)\left(\alpha f(\tau) + \phi_0 f'(\tau)\right). \tag{3.60}$$

3.3.1.4 *A posteriori* estimate of the validity of the asymptotic solutions

As in the case of a thixotropic fluid, the asymptotic solutions described in the preceding subsections have been obtained in the limit of small-amplitude oscillations, $\epsilon \to 0$ and depend on the additional independent parameter ω. It is therefore useful to obtain *a posteriori* estimates of the validity of these solutions when ω is not necessarily of order unity.

From (2.3) in section 2.2.1 we know that in the fast-adjusting regime $\hat{y} = O(\omega^{-1/(n+1)})$, and so $\partial u/\partial \hat{y} = O(\omega^{1/(n+1)})$. From equation (3.44), $\partial \Lambda_1/\partial t = O(\omega^{2(b+c-a)/(2b+c-a)})$ and $\Lambda_1 = O(\omega^{(c-a)/(2b+c-a)})$, and hence, the validity condition for the asymptotic solution in the fast-adjusting case, namely

$$\left| \epsilon^{\nu} \frac{\partial \Lambda_1}{\partial t} \right| \ll \left| \frac{\partial u_1}{\partial \hat{y}} \right|^c , \tag{3.61}$$

corresponds to

$$\epsilon^{\nu} \omega^{2(b+c-a)/(2b+c-a)} \ll \omega^{bc/(2b+c-a)}, \quad \text{i.e.} \quad \epsilon^{\nu} \omega^{1+\nu/2} \ll 1. \tag{3.62}$$

Fast-adjusting behaviour can therefore be expected in the asymptotic limits of either small oscillations, $\epsilon \to 0$, or slow oscillations, $\omega \to 0$.

In the slowly-adjusting regime, equation (3.51) yields $\Lambda_1 = O(\omega^{(c-a)/(2b+c-a)})$. To estimate the magnitude of $\partial \lambda/\partial t$ we need to consider the next order in ϵ. Integrating equation (3.54) with respect to ωt implies that $\omega \Lambda_2 = O(\omega^{bc/(2b+c-a)})$; thus the validity condition for the asymptotic solution in the slowly-adjusting case, namely

$$\epsilon^{\beta} \Lambda_1 \gg \epsilon^{2bc/(2b+c-a)} \Lambda_2, \tag{3.63}$$

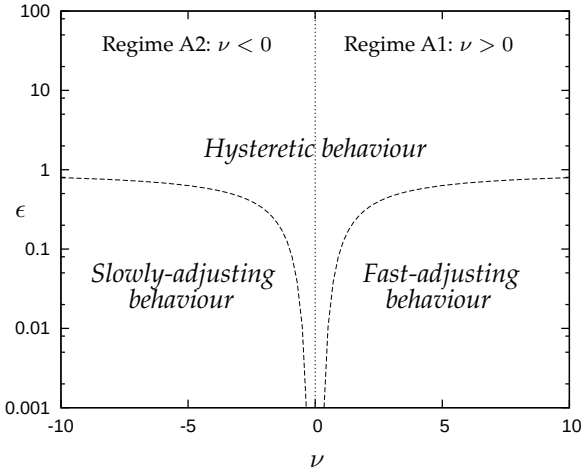

Figure 3.9: Outline of regimes of validity for the asymptotic solutions for an anti-thixotropic fluid. The dashed lines represent indicative regime boundaries for $\omega = 1$: $\epsilon^\nu = 10$ for $\nu < 0$ and $\epsilon^\nu = 0.1$ for $\nu > 0$. The dotted line represents the marginal regime $\nu = 0$.

corresponds to

$$\epsilon^\nu \omega^{(c-a)/(2b+c-a)} \gg \omega^{(bc-2b-c+a)/(2b+c-a)}, \quad \text{i.e.} \quad \epsilon^\nu \omega^{1+\nu/2} \gg 1, \tag{3.64}$$

which is exactly the complement of the condition (3.62) for fast adjustment

Figure 3.9 illustrates the parameter regimes in which the present asymptotic analysis suggests fast-adjusting, slowly-adjusting and hysteretic behaviour. To avoid ambiguity, we will henceforth refer to the parameter regime $a < c$, $\nu > 0$ as regime A1 and to the parameter regime $a < c$, $\nu < 0$ as regime A2; we will reserve the terms 'fast-adjusting' and 'slowly-adjusting' for the regimes, depending also on ϵ and ω, in which the solutions display these behaviours. When the system is neither fast- nor slowly-adjusting, we may expect its behaviour in general to be hysteretic, as shown in figure 3.9.

3.3.2 Numerical results for finite amplitude wall oscillations

We now compare the asymptotic solutions for velocity, structure parameter and shear stress at the wall with numerical solutions calculated using the finite-

element package Comsol 3.5a. As before, a finite numerical domain $0 \leq y \leq y_{\max}$ was used, with a domain length of $y_{\max} = 10$ unless otherwise stated. The initial conditions were $u(y,0) = 0$ and $\lambda(y,0) = 0$ unless otherwise stated and all other technical details were as in section 3.2.2.

3.3.2.1 Regime A1: $\nu > 0$

To illustrate the behaviour in regime A1, in which the structure parameter is fast-adjusting for small ϵ, we take $a = 1$, $b = 3/10$, $c = 2$ and $d = 1$, giving $\nu = 1/2$. We also set $\omega = 1$ so that the condition (3.62) is easily satisfied.

We first consider small-amplitude oscillations with $\epsilon = 0.01$. Figures 3.10 a and 3.10 b show snapshots of the velocity $u(y,t)$ and structure parameter $\lambda(y,t)$ at equally spaced times during a period. The first snapshot in each figure is taken at $t = 100$, by which time the system has adjusted to an essentially periodic state. The full numerical solution (solid lines) and the asymptotic solution (dashed lines) agree well for all values of y. In contrast to the corresponding thixotropic case, the antithixotropic velocity snapshots are very angular with 'corners' corresponding to the minima of λ where the structure parameter, and thus the viscosity, is nearly zero. Also, as predicted by the asymptotic solution, the antithixotropic fluid displays a finite-thickness boundary layer beyond which the fluid remains at rest, unaffected by the oscillating wall. When the viscosity has reached zero there is no diffusivity and there is effectively a slip layer at the edge of this boundary, across which no signal propagates, see section 2.3.2.

To investigate the behaviour for larger oscillations, the amplitude was increased to $\epsilon = 1$. Figures 3.10 c and 3.10 d show snapshots of the velocity $u(y,t)$ and structure parameter $\lambda(y,t)$. There are no longer pronounced 'corners' in the velocity snapshots (figure 3.10 c), as the structure parameter no longer re-

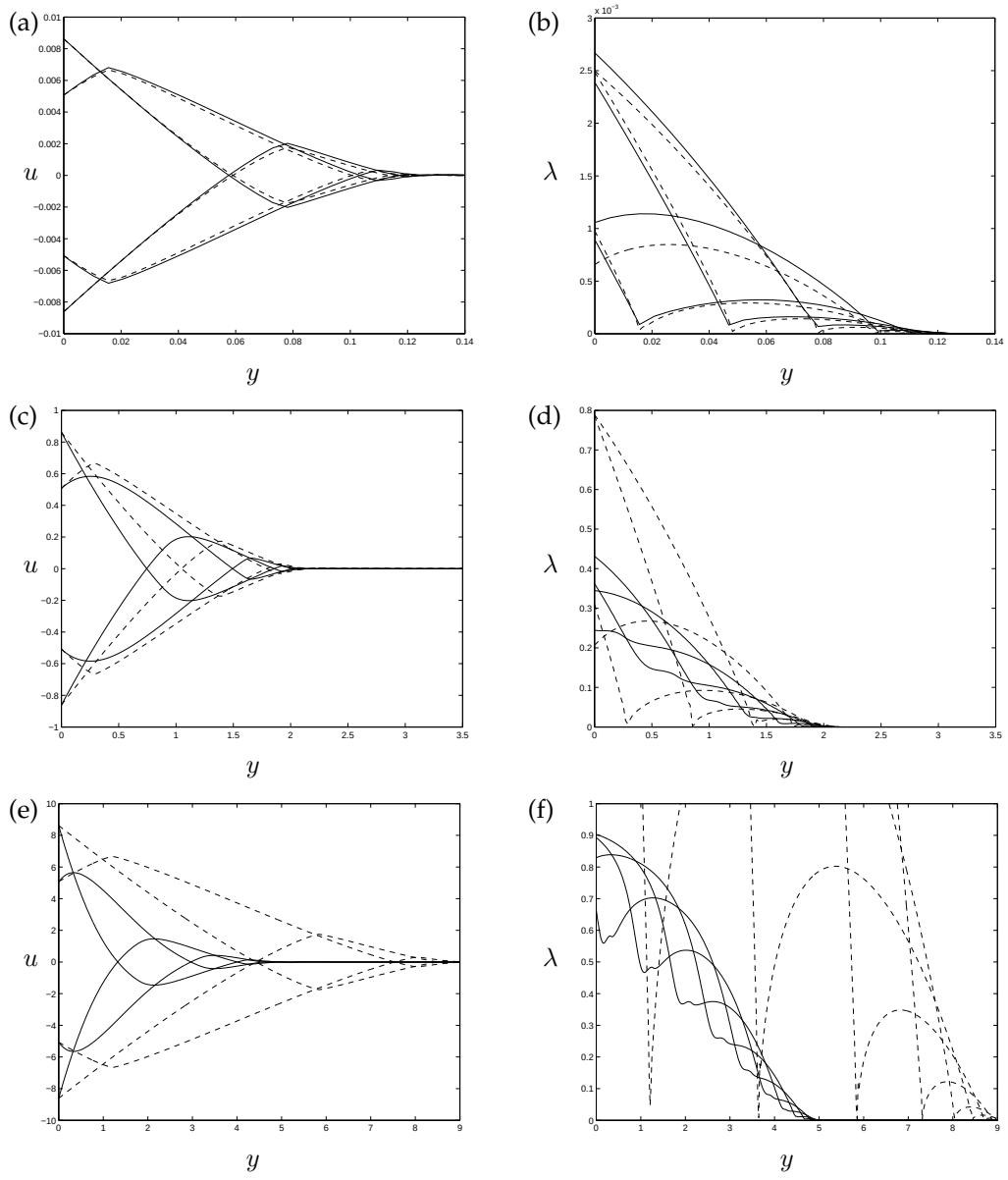

Figure 3.10: Antithixotropic regime A1 ($\nu > 0$): snapshots of the numerical solutions (solid lines) and fast-adjusting asymptotic solutions (dashed lines) with $a = 1$, $b = 3/10$, $c = 2$, $d = 1$, $\omega = 1$ and (a, b) $\epsilon = 0.01$; (c, d) $\epsilon = 1$; (e, f) $\epsilon = 10$. Plots (a), (c) and (e) show the velocity $u(y, t)$ at $t = 100 + n\pi/2$ for $n = 0$, 1, 2 and 3; and plots (b), (d) and (f) show the structure parameter $\lambda(y, t)$ at $t = 100 + n\pi/4$ for $n = 0$, 1, 2, 3.

duces to near zero at its minima (figure 3.10 d). The velocity also decays more rapidly with distance from the wall than is predicted by the asymptotic solution.

The magnitude of the structure parameter is significantly overestimated by the asymptotic solution because shear rates, and thus structure build-up rates, are generally lower than predicted by the asymptotic solution.

When the amplitude is increased further to $\epsilon = 10$ (figures 3.10 e and f), these trends are still more strongly pronounced, and the asymptotic solution for small ϵ is clearly no longer valid. The structure now has almost completely built up near the wall (figure 3.10 f); however, it does not build up to the levels predicted by the asymptotic solution, and so the oscillations in the velocity die out more quickly than the asymptotic solution predicts (figure 3.10 e). Rather than having sharp spatial minima, the snapshots of λ are now characterised by small oscillations around each minimum: these oscillations are the signature of hysteresis as the structure is unable to break down to zero as required by the instantaneous solution λ_{av}.

3.3.2.2 Regime A2: $\nu < 0$

To illustrate the behaviour in regime A2, in which the structure parameter is slowly-adjusting for small ϵ, we take $a = 1$, $b = 3/4$, $c = 2$ and $d = 1$, giving $\nu = -2/5$. We again set $\omega = 1$ so that the condition (3.64) is easily satisfied.

We first consider small-amplitude oscillations with $\epsilon = 0.01$. Figures 3.11 a and 3.11 b show snapshots of the velocity $u(y,t)$ and structure parameter $\lambda(y,t)$ at equally spaced times during a period. The first snapshot is taken at $t = 100$, by which time the velocity has adjusted to an essentially periodic state. The numerical solution (solid lines) and the asymptotic solution (dashed lines) agree well for all values of y. The velocity solution is not angular as in the fast-adjusting case. However, there is still a finite-thickness boundary layer, at $0 \leq y \leq y_0 = \epsilon^{2/5}\hat{y}_0 \approx 0.586$. In figure 3.11 b the numerical solution (solid lines) for the structure parameter oscillates weakly over a period, around the

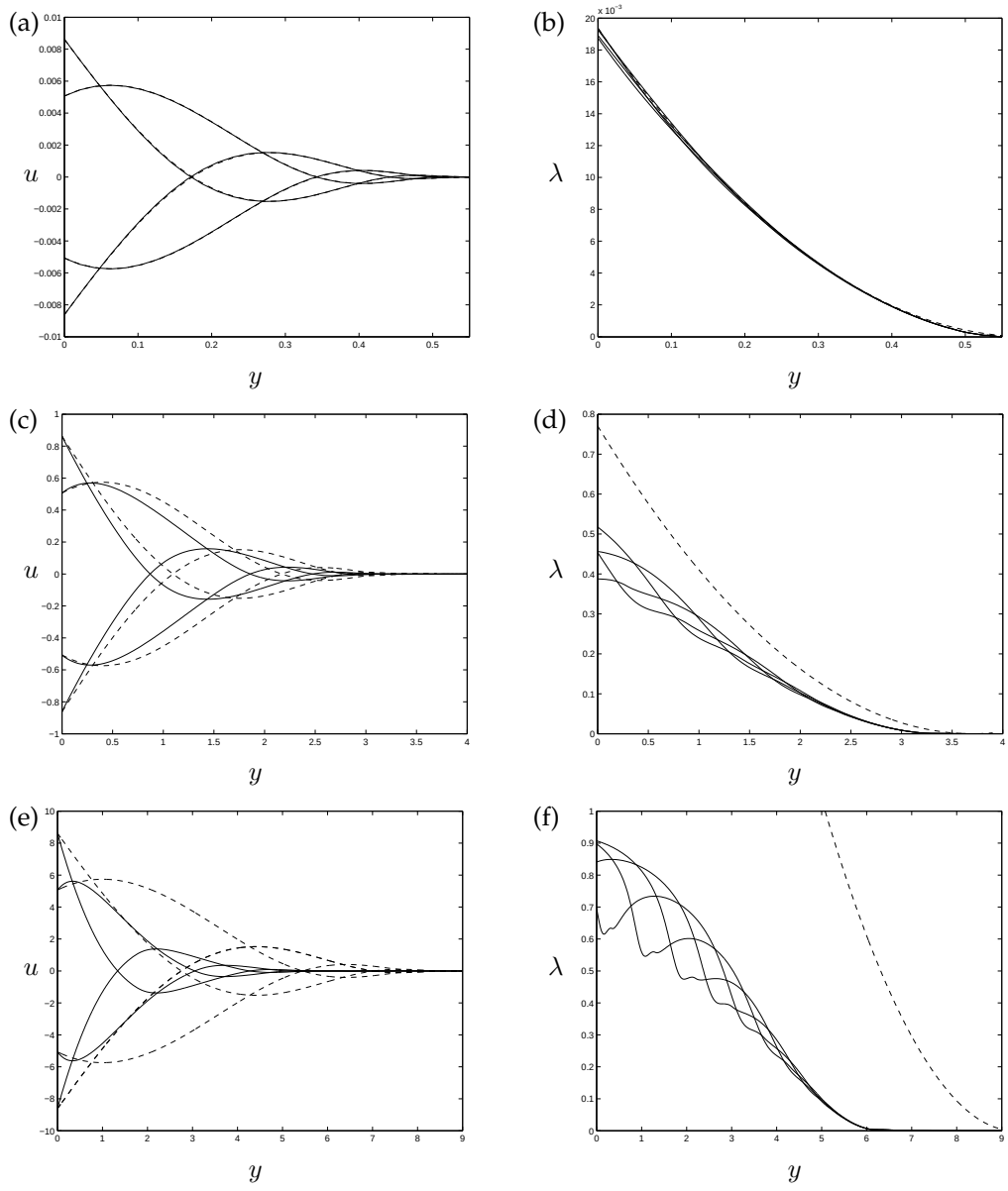

Figure 3.11: Antithixotropic regime A2 ($\nu < 0$): snapshots of the numerical solutions (solid lines) and slowly-adjusting asymptotic solutions (dashed lines) with $a = 1$, $b = 3/4$, $c = 2$, $d = 1$, $\omega = 1$ and (a, b) $\epsilon = 0.01$; (c, d) $\epsilon = 1$; (e, f) $\epsilon = 10$. Plots (a), (c) and (e) show the velocity $u(y,t)$ at $t = 100 + n\pi/2$ for $n = 0$, 1, 2 and 3; and plots (b), (d) and (f) show the structure parameter $\lambda(y,t)$ at $t = 100 + n\pi/4$ for $n = 0$, 1, 2, 3.

asymptotic value (3.51).

To investigate the behaviour for larger oscillations, the amplitude was again

increased to $\epsilon = 1$. Figures 3.11 c and d show snapshots of the velocity $u(y,t)$ and structure parameter $\lambda(y,t)$. The deviation from the asymptotic solution is now more apparent. The structure parameter now oscillates around an average equilibrium value, and the asymptotic solution overestimates this. Figure 3.11 c shows the velocity decaying faster than the asymptotic solution predicts, as the viscosity is lower than predicted.

When the amplitude is increased further to $\epsilon = 10$ (figure 3.11 e and f), the asymptotic solution for small ϵ is clearly no longer valid. The behaviour for $\epsilon = 10$ is very different from that in the limit $\epsilon \to 0$. However, the structure parameter still varies only weakly throughout a period (figure 3.11 f) so the system still shows essentially slowly-adjusting behaviour. The velocity now decays much faster than the asymptotic solution predicts. As ϵ increases, figures 3.11 b, d and e tell a similar story to that seen in figure 3.10. As ϵ increases, first oscillations and then small double oscillations appear: the numerical solution in figure 3.11 f is very similar to that in figure 3.10 f. As in the thixotropic case, with increasing ϵ the distinction between the regimes becomes increasingly blurred.

3.3.2.3 Shear stress at the wall

It is also of interest to examine the shear stress at the wall. Figures 3.12 a and b show the shear stress $\tau_{\mathrm{w}}(t)$, normalised by $\epsilon^{1+\beta/2}$, for regimes A1 and A2 respectively. (In figure 3.12 a for $\epsilon = 10$ only, the mesh comprised 1920 equally-spaced grid points to resolve the small-scale oscillations seen in figure 3.11 f properly.)

In each case, the variation of $\tau_{\mathrm{w}}(t)$ for small ϵ is nearly sinusoidal, and, in contrast to the thixotropic case, as ϵ is increased, the variation remains nearly sinusoidal. In both figures, the rescaled shear stress $\tau_{\mathrm{w}}/\epsilon^{1+\beta/2}$ decreases with increasing ϵ, although it decreases more gradually in regime A2 as shown in figure 3.12 b.

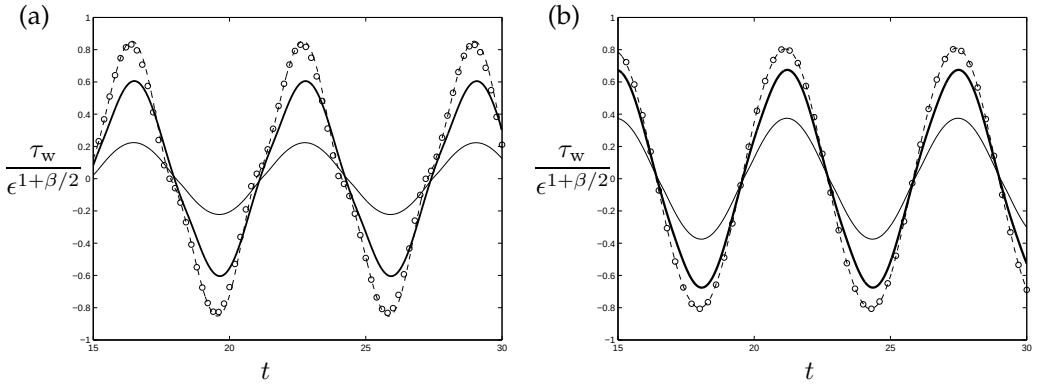

Figure 3.12: Normalised shear stress at the wall, $\tau_w(t)/\epsilon^{1+\beta/2}$, with $a = 1$, $c = 2$, $d = 1$ and $\omega = 1$ and (a) $b = 3/10$, (b) $b = 3/4$. Figure (a) is the shear stress for regime A1 ($\nu > 0$) and figure (b) is the shear stress for regime A2 ($\nu < 0$). The circles represent the asymptotic solution; lines represent the numerical solutions for $\epsilon = 0.01$ (dashed); $\epsilon = 1$ (thick solid); $\epsilon = 10$ (thin solid).

It is interesting to note that the rapid variations of τ_w seen for thixotropic fluids (figure 3.6) are absent for antithixotropic cases, because there is no longer a positive feedback between λ and $\partial u/\partial y$ at the wall.

3.3.2.4 Marginal regime $\nu = 0$

Finally, to illustrate the behaviour in the marginal regime $\nu = 0$ we take $a = 1$, $b = 1/2$, $c = 2$ and $d = 1$, giving $\nu = 0$, $\alpha = 2$ and the numerically determined asymptotic parameters $\hat{y}_0 = 3.15$ and $\phi_0 = 2.591$. As in all the previously considered regimes, we set $\omega = 1$.

We first consider small-amplitude oscillations with $\epsilon = 0.01$. Figures 3.13 a and 3.13 b show snapshots of the velocity $u(y,t)$ and structure parameter $\lambda(y,t)$ at equally spaced times during a period. The first snapshot in each figure is taken at $t = 100$, by which time the system has adjusted to an essentially periodic state. Although the asymptotic solutions capture the overall decay of the velocity and structure parameter, they deviate from the numerical solu-

tions close to the wall $y = 0$; this reflects the inconsistency between the non-sinusoidal velocity variation in the asymptotic solution and the sinusoidal variation imposed on the numerical solution, compare with section 2.3.3.

To investigate the behaviour for larger oscillations, the amplitude was again increased first to $\epsilon = 1$ (figures 3.13 c and d) and then to $\epsilon = 10$ (figure 3.13 e and f). As ϵ is increased, the asymptotic solutions come to severely overestimate the numerical solutions for both the velocity and structure parameter, and by $\epsilon = 10$, double oscillations of the structure parameter have again appeared (figure 3.13 f). Figures 3.10 f, 3.11 f and 3.13 f all show the same hysteretic behaviour: distinctive fast and slow behaviour is no longer apparent.

The shear stress in the marginal regime (figure 3.14) is also similar to that in the other two regimes and the variation is nearly sinusoidal for all values of ϵ examined. The rescaled shear stress $\tau_{\mathrm{w}}/\epsilon^{1+\beta/2}$ decreases weakly with increasing ϵ. The agreement between numerical and asymptotic solutions for $\epsilon = 0.01$ is poorer than before, reflecting the poorer agreement for u and λ (figures 3.13 a and b).

3.4 Rheograms for thixotropic and antithixotropic fluids

A standard form in which to present rheometric data is a plot of the shear stress at the wall against the shear rate in the rheometer, often called a rheogram (section 1.2.6). Although the Stokes flows analysed in this paper are non-rheometric, because the shear rate is not spatially constant, it is interesting to construct equivalent rheograms in order to identify key features of the flow. In particular, hysteresis loops in a rheogram are the signature of lag effects (Mewis and Wagner 2009).

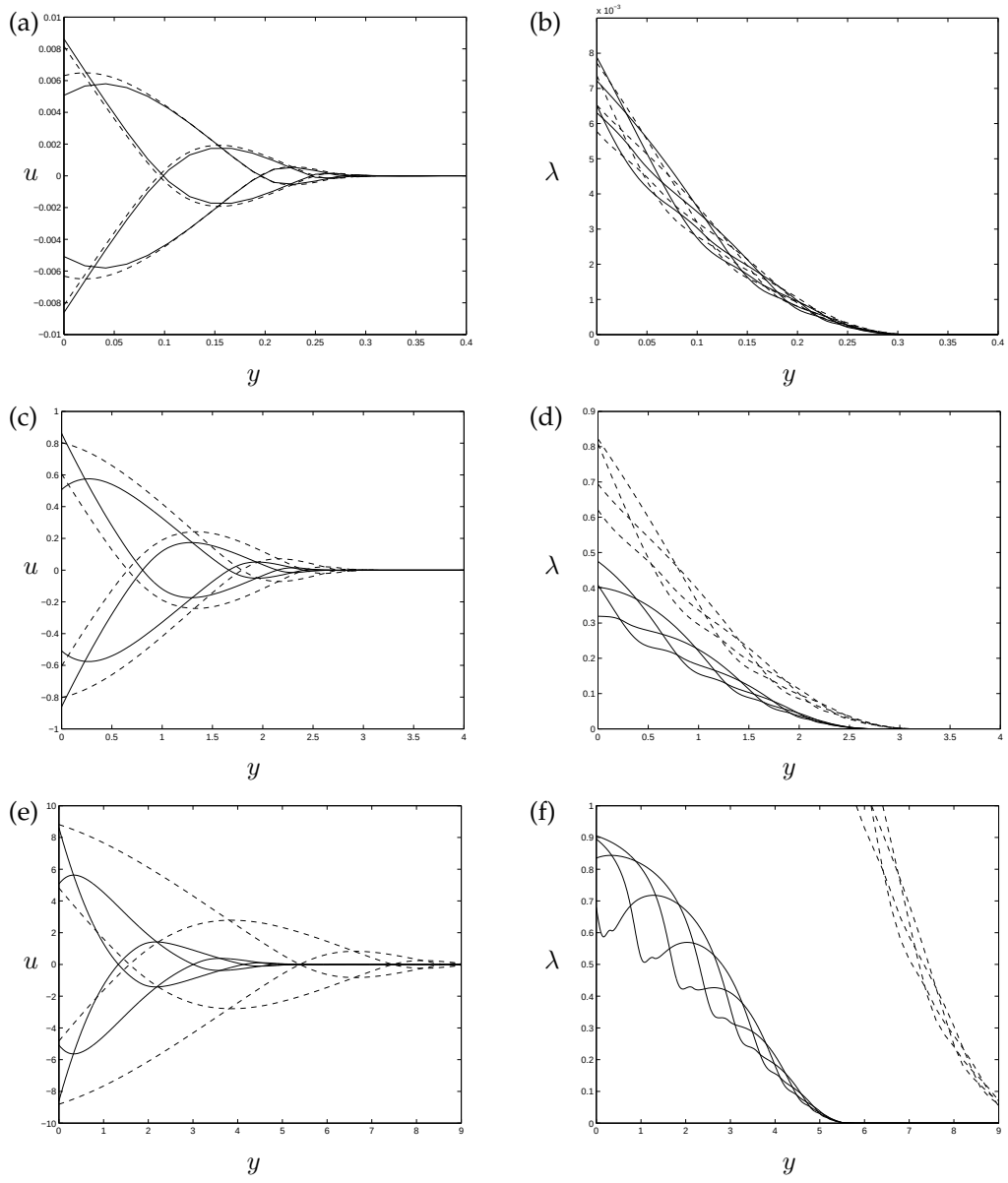

Figure 3.13: Antithixotropic marginal regime ($\nu = 0$): snapshots of the numerical solutions (solid lines) and marginal asymptotic solutions (dashed lines) with $a = 1$, $b = 1/2$, $c = 2$, $d = 1$, $\omega = 1$ and (a, b) $\epsilon = 0.01$; (c, d) $\epsilon = 1$; (e, f) $\epsilon = 10$. Plots (a), (c) and (e) show the velocity $u(y,t)$ at $t = 100 + n\pi/2$ for $n = 0, 1, 2$ and 3; and plots (b), (d) and (f) show the structure parameter $\lambda(y,t)$ at $t = 100 + n\pi/4$ for $n = 0, 1, 2, 3$.

In this section, we present the results of the numerical integrations presented in sections 3.2 and 3.3 in this form. In each case, the shear stress τ_{w} is plotted

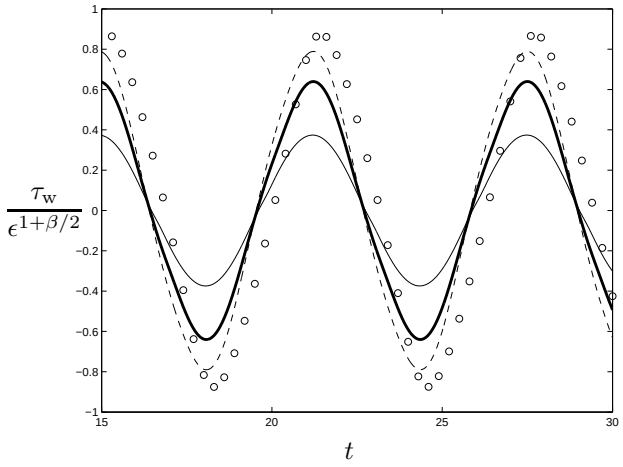

Figure 3.14: Antithixotropic marginal regime: normalised shear stress at the wall, $\tau_w(t)/\epsilon^{1+\beta/2}$, with $a = 1$, $b = 1/2$, $c = 2$, $d = 1$ and $\omega = 1$. The circles represent the asymptotic solution; lines represent the numerical solutions for $\epsilon = 0.01$ (dashed); $\epsilon = 1$ (thick solid); $\epsilon = 10$ (thin solid).

against the instantaneous shear rate $\partial u/\partial y$ evaluated at the wall, $y = 0$. In each plot, an initial transient can be seen followed by adjustment to an effectively periodic state: we focus our discussion on these periodic states. The rheograms also plot the instantaneous equilibrium shear stress $\tau_{eq} = \lambda_{eq}\partial u/\partial y$, where λ_{eq} is calculated from equation (3.10).

3.4.1 Rheograms for thixotropic fluids

Figure 3.15 shows rheograms for the three thixotropic regimes: regime T1 (figures 3.15 a and b, which correspond to the snapshots in figure 3.3); the marginal regime (figures 3.15 c and d, which correspond to the snapshots in figure 3.7); and regime T2 (figures 3.15 e and f, which correspond to the snapshots in figure 3.4). The corresponding plots of $\tau_w(t)$ are shown in figures 3.6 and 3.8. In each case the equilibrium behaviour is shear-thinning, and $c - a + b = 0$ so $\tau_{eq} \to 1$ as $|\partial u/\partial y| \to \infty$ (section 3.1.4).

For small values of ϵ (figures 3.15 a, c and e), the fluid is nearly fully structured, with $\lambda \approx 1$. The rheograms are therefore indistinguishable from those for

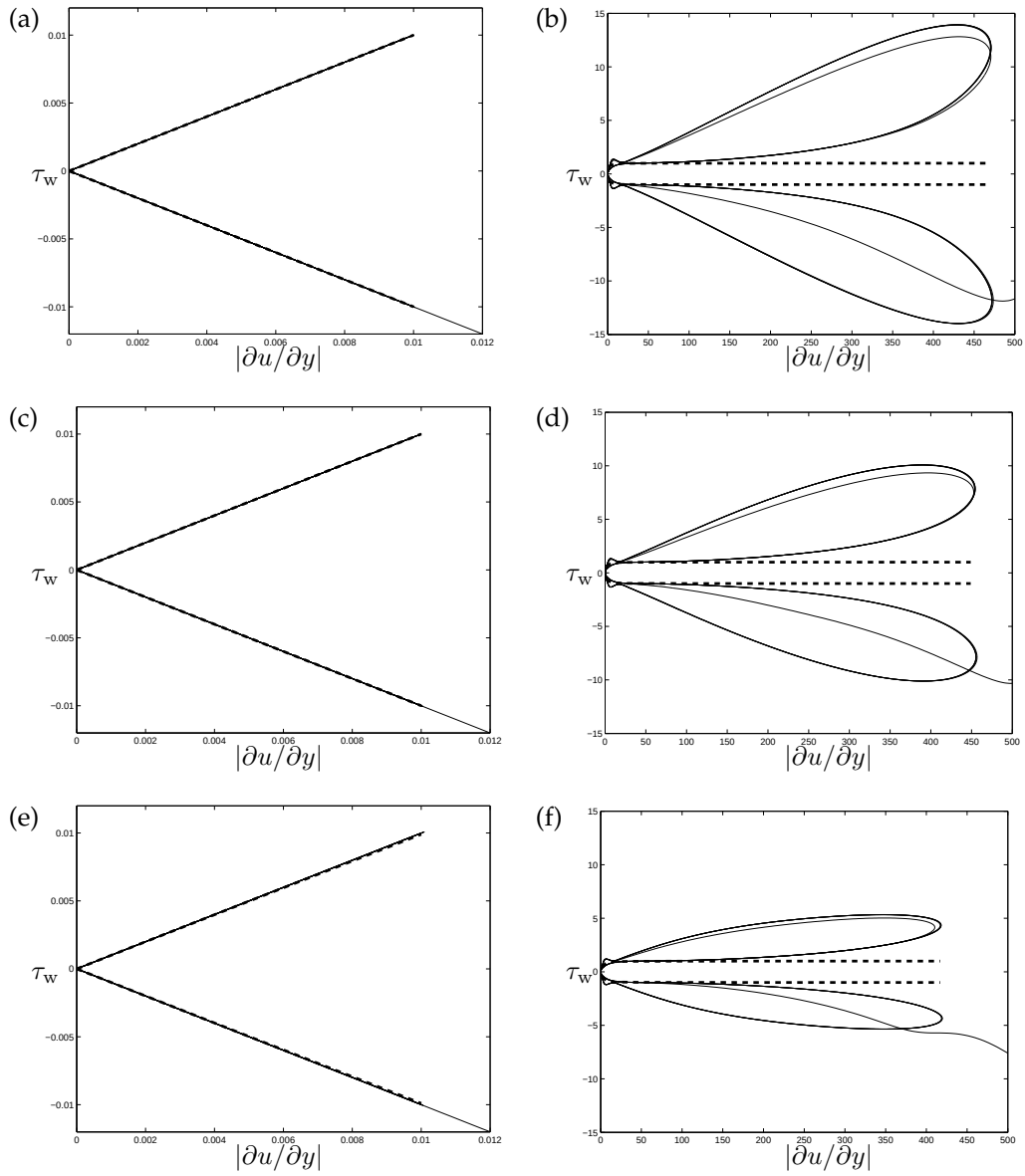

Figure 3.15: Rheograms for thixotropic fluids with $a = 2$, $b = 1$, $c = 1$, $\omega = 1$ and (a, b) $d = 1/3$; (c, d) $d = 1/2$; (e, f) $d = 1$. Plots (a), (c) and (e) show the numerical results for $\epsilon = 0.01$ (solid lines) and plots (b), (d) and (f) show the numerical results for $\epsilon = 10$ (solid lines); dashed lines in each case represent the instantaneous equilibrium shear stress $\tau_{\rm eq}$.

a Newtonian fluid, $\tau_{\rm w} = \pm|\partial u/\partial y|$. Note also that since $\lambda_{\rm eq} \approx \lambda_{\rm av} \approx 1$, there is no visible difference between the fast- and slowly-adjusting regimes.

As ϵ increases, hysteresis loops appear, as shown for $\epsilon = 10$ (figures 3.15 b, d and f). The rapid variation of τ_{w} at small shear rates, commented on in section 3.2.2.2, manifests itself as a small secondary loop close to the origin in these plots; note that the curve does not intersect itself so this secondary loop is not completely closed. The overall behaviour is reminiscent of the stress overshoot due to the breakdown of an initial structure (Mewis and Wagner 2009, figure 2(b)). Indeed, τ_{w} is everywhere higher than or equal to its 'equilibrium' value τ_{eq}, so we may think of these hysteresis loops as representing the signature of a persistent stress overshoot.

For the large value of ϵ employed in figures 3.15 b, d and f, some systematic differences are apparent between the three regimes: as d increases from regime T1 through to regime T2, the amplitude of variation of τ_{w} decreases, so the hysteresis loops become narrower. It is slightly surprising that the deviation of τ_{w} from τ_{eq} is greatest in the 'fast' regime T1 and least in the 'slow' regime T2.

3.4.2 Rheograms for antithixotropic fluids

Figure 3.16 shows rheograms for the three antithixotropic regimes: regime A1 (figures 3.16 a and b, which correspond to the snapshots in figure 3.10); the marginal regime (figures 3.16 c and d, which correspond to the snapshots in figure 3.13); and regime A2 (figures 3.16 e and f, which correspond to the snapshots in figure 3.11). The corresponding plots of $\tau_{\mathrm{w}}(t)$ are shown in figures 3.12 and 3.14.

In contrast to the thixotropic case, the three regimes behave differently even for $\epsilon = 0.01$. Hysteresis loops are present in all three regimes; in regime A2 (figure 3.16 e) we see an additional consequence of slow adjustment, which is that the amount of hysteresis decays over many cycles, with the loops gradually moving outwards and becoming narrower as the system approaches its peri-

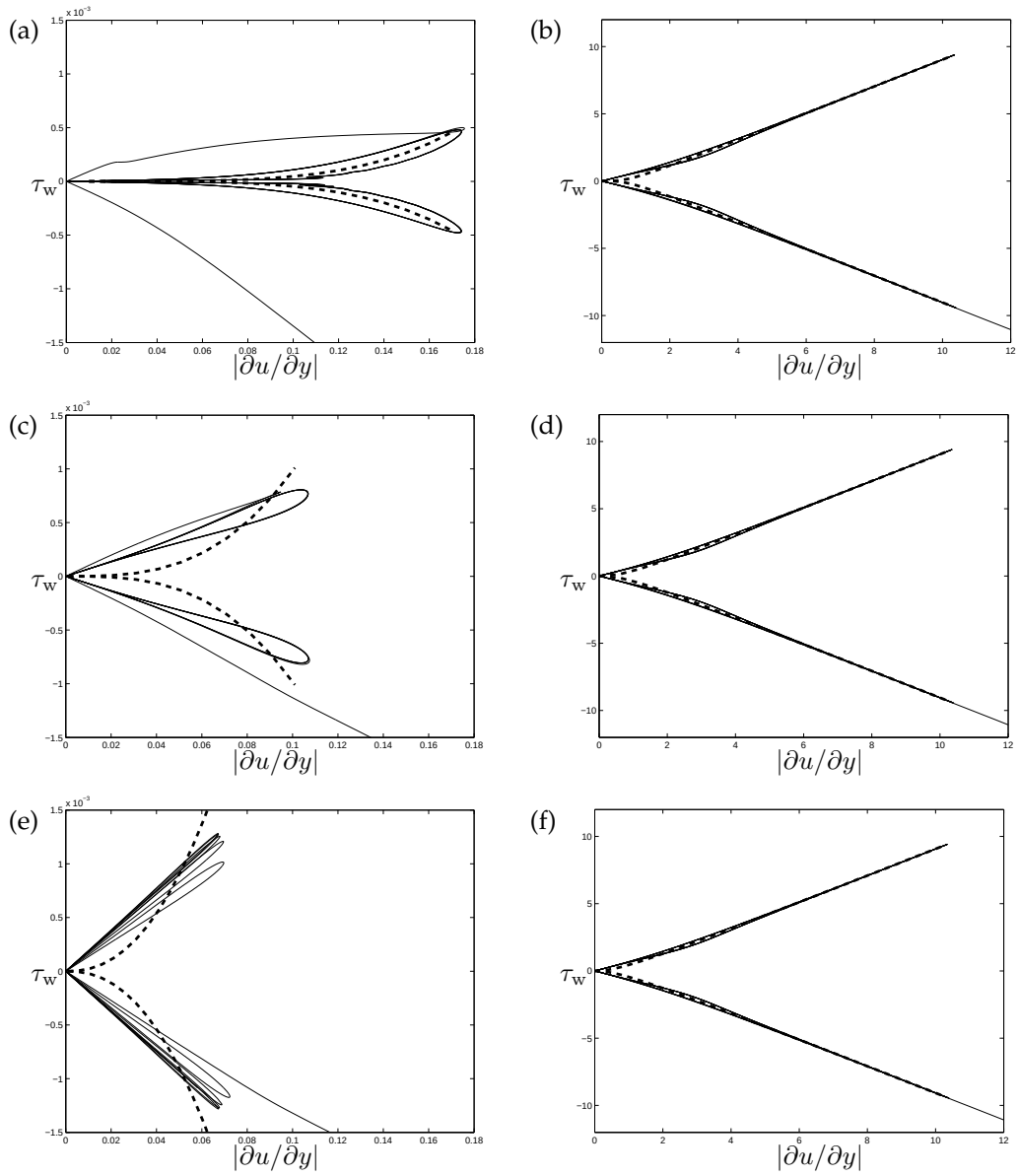

Figure 3.16: Rheograms for antithixotropic fluids with $a = 1$, $c = 2$, $d = 1$, $\omega = 1$ and (a, b) $b = 3/10$; (c, d) $b = 1/2$; (e, f) $b = 3/4$. Plots (a), (c) and (e) show the numerical results for $\epsilon = 0.01$ (solid lines) and plots (b), (d) and (f) show the numerical results for $\epsilon = 10$ (solid lines); dashed lines in each case represent the instantaneous equilibrium shear stress τ_{eq}.

odic state. In the fast-adjusting regime only (figure 3.16 a), the hysteresis loops are centred on the equilibrium curve τ_{eq}; in the slowly-adjusting regime (fig-

ure 3.16 e) the equilibrium solution is clearly irrelevant, whereas the marginal regime (figure 3.16 c) may be affected by the competition between the sinusoidal forcing at the wall and the 'natural' non-sinusoidal waveform of oscillation (cf. figure 3.13 a). As b is increased from regime A1 through to regime A2, it is also noticeable that the range of shear rates decreases somewhat while the range of shear stresses increases.

Again in contrast to the thixotropic case, the rheograms for large ϵ (figure 3.16 b, d and f) are almost indistinguishable in the three antithixotropic regimes, which is consistent with the general similarity of the solutions (section 3.3.2.4). Although some hysteresis is apparent, these plots in fact closely resemble those that would be expected for a Newtonian fluid with a constant value of $\lambda = 1$, reflecting the fact that the structure is nearly completely built up at the wall. As for a thixotropic fluid under small oscillations, $\lambda_{\mathrm{eq}} \approx \lambda_{\mathrm{av}} \approx 1$ and so the equilibrium shear stress τ_{eq} agrees rather closely with the numerically calculated stress; there are, however, still some under- and overshoots at lower shear rates.

In summary, although the rheograms reveal interesting patterns in the behaviour of the solutions, it is not straightforward to extract distinctive signatures of thixotropic or antithixotropic behaviour from them. This sounds a cautionary note for future attempts to use Stokes flow as a non-rheometric rheological device (Balmforth *et al.* 2009).

3.5 Summary

We have described a combined asymptotic and numerical investigation of the Stokes problem for a general model of thixotropic and antithixotropic fluids. The emphasis of our investigation has been on the periodic oscillatory behaviour of the system, rather than on the transient initial phase in which the system ad-

justs to the attracting periodic solution.

The asymptotic analysis in the limit of small-amplitude oscillations revealed distinct regimes of fast and slow structural response for both thixotropic and antithixotropic fluids. In the fast-adjusting regimes, the structure is an instantaneous function of the shear, and so the fluid acts like a generalised Newtonian fluid. In the slowly-adjusting regimes, the local structure is determined by a long-term average of build-up and breakdown rates. In the marginal regimes between the limits of fast and slow adjustment, the variation of the structure parameter is lagged and attenuated relative to its instantaneous equilibrium value. This hysteretic response becomes increasingly dominant in all regimes as the amplitude of oscillation increases. When this amplitude is large enough, the distinction between the fast- and slowly-adjusting regimes disappears entirely.

The boundaries of the fast- and slowly-adjusting regimes depend on the relative magnitudes of the dimensionless amplitude of oscillation ϵ and the dimensionless frequency of oscillation ω. They also depend, in a rather subtle manner, on the build-up and breakdown exponents a, b, c and d that appear in the evolution equation (3.5) for the structure parameter. This subtlety suggests that it may be necessary when employing structure evolution equations, or when fitting the parameters of such equations using conventional rheometric data, to pay careful attention to these exponents. Such attention would contrast with the prevailing approach of choosing these exponents for simplicity and devoting more attention to identifying and calibrating a constitutive equation. The distinct regimes that emerge in the Stokes problem at low amplitudes of oscillation could perhaps provide a useful tool for discrimination when assigning values to the build-up and breakdown exponents.

The most interesting deviations from Newtonian behaviour come for anti-

thixotropic fluids, which, like shear-thickening power-law fluids, as seen in section 2.3.2, develop a boundary layer of finite thickness beyond which the fluid is unaffected by the oscillating wall. The thickness of this layer scales with $\epsilon^{\beta/2}$, where the parameter β is defined by (3.40) in terms of the exponents in the structure evolution equation; the velocity amplitude decays algebraically and the structure parameter decays quadratically towards the edge of the layer.

In contrast to the internal behaviour of the fluid, the shear stress at the wall, $\tau_{\mathrm{w}}(t)$, shows surprisingly weak deviations from Newtonian behaviour. In particular, changes in the structure and the shear rate close to the wall counteract each other so that for thixotropic fluids the shear stress scales roughly with ϵ even when ϵ is significantly larger than unity; similarly, for antithixotropic fluids the shear stress scales roughly with $\epsilon^{1+\beta/2}$ well beyond the regime in which this scaling is formally valid. Thixotropy affects the shear stress most conspicuously for large amplitudes of oscillation, when it leads to rapid variations of $\tau_{\mathrm{w}}(t)$ shortly before and after the wall shear rate changes sign. The feedback between increasing structure and decreasing shear that leads to these variations shows up as a characteristic 'secondary loop' when the stress and shear at the wall are plotted as rheograms. The rheograms also reveal hysteresis clearly in many cases; however, it is not in general straightforward to identify the rheological characteristics of the fluid from them.

3.6 Appendix: pseudo-Newtonian behaviour when $a = c$

In this Appendix we consider the special case $a = c$ in which the equilibrium value of the structure parameter λ is independent of the shear rate. In this special case, the characteristic scales (3.6) are undefined and we instead non-

dimensionalise using the frequency of oscillation $\hat{\omega}$, obtaining

$$\hat{U}_0 = \hat{\nu}_0^{1/2} \left(\frac{\hat{\omega}^{2-a}}{\hat{k}_1^2} \right)^{1/(2a)}, \quad \hat{Y}_0 = \left(\frac{\hat{\nu}_0}{\hat{\omega}} \right)^{1/2} \quad \text{and} \quad \hat{T}_0 = \frac{1}{\hat{\omega}}. \tag{3.65}$$

Equation (3.7) is unchanged, while equation (3.5) becomes

$$\frac{\partial \lambda}{\partial t} = - \left| \frac{\partial u}{\partial y} \right|^a \left[\lambda^b - \kappa_2 (1-\lambda)^d \right], \tag{3.66}$$

where $\kappa_2 = \hat{k}_2/\hat{k}_1$ is the ratio of the structural build-up and breakdown rates. Since the frequency of oscillation has been scaled out, the wall boundary condition becomes $u(0,t) = \epsilon \cos(t)$.

Equations (3.7) and (3.66) admit a periodic exact solution for all values of ϵ,

$$u = \epsilon \mathrm{e}^{-\gamma y} \cos(\gamma y - t) \quad \text{where} \quad \gamma = \sqrt{\frac{1}{2\lambda}}, \tag{3.67}$$

and where the constant value of λ satisfies

$$\frac{\lambda^b}{(1-\lambda)^d} = \kappa_2. \tag{3.68}$$

The periodic behaviour of the system is therefore identical to that of a Newtonian fluid, but with a viscosity that is self-selected via the equilibrium value of the structure parameter rather than being independently imposed.

Although the local shear rate does not control the eventual value of λ, the shear rate determines how rapidly the pseudo-Newtonian solution is reached from a given initial condition. Figure 3.17 illustrates the adjustment of $\lambda(y,t)$ from the initial condition $\lambda(y,0) = 1$. Since $\partial\lambda/\partial t \propto |\partial u/\partial y|^a$, adjustment is most rapid close to the wall, where the pseudo-Newtonian solution becomes established within a few periods; beyond a distance of order $1/\gamma$, however, ad-

justment is far slower, and at the right-hand end of the computational domain the pseudo-Newtonian solution is attained only at extremely large times.

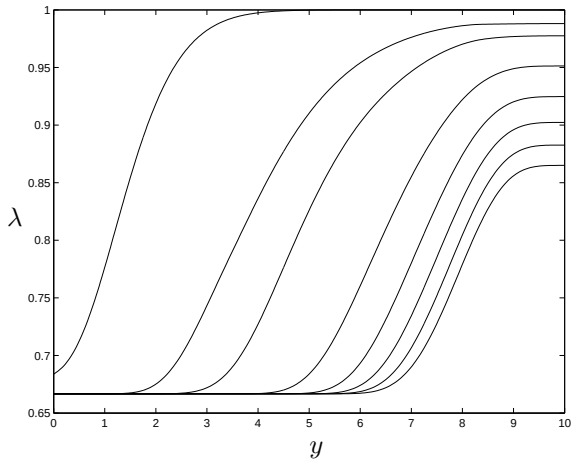

Figure 3.17: 'Pseudo-Newtonian' regime: snapshots of the structure parameter $\lambda(y,t)$ at (from left to right) $t = 1$, 10, 25, 100, 200, 300, 400, 500, with $a = 1$, $b = 1$, $c = 1$, $d = 1$, $\epsilon = 1$ and $\kappa_2 = 2$.

3.7 Appendix: Maple code

3.7.1 Code for obtaining figure 3.1

```
>restart;with(plots):
```

Set up ordinary differential equation (3.29).

```
>ode:=omega*diff(l(tau),tau)+l(tau)^d*abs
(cos(tau))^c=abs(cos(tau))^a;
```

Set parameter values.

```
>parvals01:=omega=0.1,a=2,c=1,d=0.5;
>parvals05:=omega=0.5,a=2,c=1,d=0.5;
>parvals1000:=omega=1000,a=2,c=1,d=0.5;
```

Put parameter values into the ODE and solve.

```
>sol01:=dsolve(subs(parvals01,ode,l(0)=0.616),l(tau),
numeric);
>sol05:= dsolve(subs(parvals05,ode,l(0)=0.616),l(tau),
numeric);
>sol1000:= dsolve(subs(parvals1000,ode,l(0)=0.616),l(tau),
numeric);
```

3.7.2 Code for obtaining f and g in section 3.3.1.3

```
>restart;with(plots):
```

Set up governing equations (3.57) and (3.58).

```
>de1:=omega*diff(g(tau),tau)=-abs(alpha*f(tau)+phi0*diff(
f(tau),tau))∧a*(g(tau))∧b+abs(alpha*f(tau)+phi0*diff(
f(tau),tau))∧c;
>de2:=omega*diff(f(tau),tau)=(2*g(tau)+phi0*diff(g(tau),
tau))*(alpha*f(tau)+phi0*diff(f(tau),tau))+g(tau)*((alpha
-1)*(alpha*f(tau)+phi0*diff(f(tau),tau))+(phi0*alpha*diff(
f(tau),tau)+phi0∧2*diff(f(tau),tau$2)));
```

Set parameter values.

```
>parvals:=a=1,b=1/2,c=2,d=1,omega=1;
>de1a:=subs(parvals,subs(alpha=1+2/c,de1)):
>de2a:=subs(parvals,subs(alpha=1+2/c,de2)):
>phi00:=2.59151;
```

Put parameter values into the governing equations and solve.

```
>sol:=dsolve(subs(phi0=phi00,de1a,de2a,g(0)=0.1,f(0)=0.1,
D(f)(0)=0),{f(tau),g(tau)},numeric):
```

Plot f over a single period and change `phi00` value until the start and end of the period match up.

```
>odeplot(sol,subs(parvals,[[tau,f(tau)],[tau+2*Pi,f(tau)
]]),200..200+2*Pi,numpoints=500);
```

This procedure builds an array of data for f.

```
>farray:=proc(npts,phi00) global parvals,farr;
local i,taui,solf,T;
T:= 2*Pi;
solf:= dsolve(subs(phi0=phi00,de1a,de2a,g(0)=0.1,f(0)=0.1,
D(f)(0)=0),f(tau),g(tau),numeric);
for i from 0 to npts-1 do taui:=evalf(T*(4+i/npts));
farr[i,0]:=T*(taui/T-floor(taui/T));
farr[i,1]:=subs(solf(taui),f(tau));
farr[i+npts,0]:=T*(taui/T-floor(taui/T))+T;
farr[i+npts,1]:=subs(solf(taui),f(tau))od;
end;
```

This procedure takes a value of τ and returns the corresponding value of f.

```
>fout:= proc(tau,npts) global farr, parvals;
local i, tau0, fval, T;
T:= 2*Pi;
tau0:= T*(tau/T-floor(tau/T));
for i from 0 to 2*npts-3 do
if evalf((farr[i,0]-tau0)*(farr[i+1,0]-tau0)) <=0 then
fval:= farr[i,1]+(farr[i+1,1]-farr[i,1])/(farr[i+1,0]-
farr[i,0])*(tau0-farr[i,0]) fi od;
return(evalf(fval));
end;
```

Same procedure for g: start by plotting g and checking the start and end of the period match up.

```
>odeplot(sol,subs(parvals,[[tau,g(tau)],[tau+2*Pi,g(tau)
]]),200..200+subs(parvals,2*Pi),numpoints=500);
```

This procedure builds an array of data for g.

```
>garray:= proc(npts,phi00) global parvals, garr;
local i, taui, solg, T;
T:= 2*Pi;
solg:= dsolve(subs(phi0=phi00,de1a,de2a,g(0)=0.1,f(0)=0.1,
D(f)(0)=0),f(tau),g(tau),numeric);
for i from 0 to npts-1 do taui:= evalf(T*(4+i/npts));
garr[i,0]:= T*(taui/T-floor(taui/T));
garr[i,1]:= subs(solg(taui),g(tau));
garr[i+npts,0]:= T*(taui/T-floor(taui/T))+T;
garr[i+npts,1]:= subs(solg(taui),g(tau)) od;
end;
```

This procedure takes a value of τ and returns the corresponding value of g.

```
>gout:= proc(tau,npts) global garr, parvals;
local i, tau0, gval, T;
T:= 2*Pi;
tau0:= T*(tau/T-floor(tau/T));
for i from 0 to 2*npts-3 do
if evalf((garr[i,0]-tau0)*(garr[i+1,0]-tau0)) <=0 then
gval:= garr[i,1]+(garr[i+1,1]-garr[i,1])/(garr[i+1,0]-
garr[i,0])*(tau0-garr[i,0]) fi od;
return(evalf(gval));
end;
```

Chapter 4

Flows of thixotropic and antithixotropic fluids in a slowly-varying channel

4.1 Introduction

In this chapter we will consider flow of thixotropic and antithixotropic fluids in a slowly-varying channel.

We recall from section 1.5.2 that although there are several studies which consider thin-film and related flows (for example dam-break flow, flow in a narrow fracture and levelling), these studies either require full numerical simulations on which to base a reduced dynamical model (Livescu *et al.* 2011) or make *ad hoc* assumptions such as postulating a layer-averaged value of the structure parameter (Chanson *et al.* 2006; Pritchard and Pearson 2006). It is not clear whether such assumptions are justifiable, and so a systematic approach is needed. The work in this chapter is the first attempt, to our knowledge, to do so; we will develop such an approach in the paradigmatic setting of slowly-varying

two-dimensional channel flow.

We will first (section 4.2) present the classical lubrication theory for Newtonian fluids and use this as a foundation for the more complicated thixotropic and antithixotropic problems. In section 4.3 we will present a general lubrication theory for thixotropic and antithixotropic fluids, based like the Newtonian theory on an expansion in powers of the small aspect ratio δ. To illustrate this approach, in section 4.4 we will investigate the special case $d = 0$ of our rheological model in which we recover a power-law rheology at equilibrium.

4.2 The Newtonian problem

We consider the two-dimensional steady pressure-driven flow of fluid in a slowly-varying channel $0 \leq \hat{y} \leq \hat{h}(\hat{x})$ with characteristic length scales $\hat{L}$ in the $\hat{x}$-direction and $\hat{H}$ in the $\hat{y}$-direction, as shown in figure 4.1. The channel is slowly-varying provided that the aspect ratio $\delta = \hat{H}/\hat{L} \ll 1$ is small.

We will first describe the well-known solution for a Newtonian fluid. The steady flow is governed by the mass conservation and Navier-Stokes equations

$$\hat{\nabla} \cdot \hat{\mathbf{u}} = 0 \tag{4.1}$$

and

$$\hat{\rho}\frac{\mathrm{D}\hat{\mathbf{u}}}{\mathrm{D}\hat{t}} = -\hat{\nabla}\hat{p} + \hat{\nabla} \cdot \underline{\underline{\hat{\tau}}}, \tag{4.2}$$

where the fluid velocity $\hat{\mathbf{u}}(\hat{x}, \hat{y}) = (\hat{u}(\hat{x}, \hat{y}), \hat{v}(\hat{x}, \hat{y}))$, the pressure $\hat{p} = \hat{p}(\hat{x}, \hat{y})$ and $\underline{\underline{\hat{\tau}}}$ is the shear stress tensor. From equation (4.1),

$$\frac{\partial \hat{u}}{\partial \hat{x}} + \frac{\partial \hat{v}}{\partial \hat{y}} = 0. \tag{4.3}$$

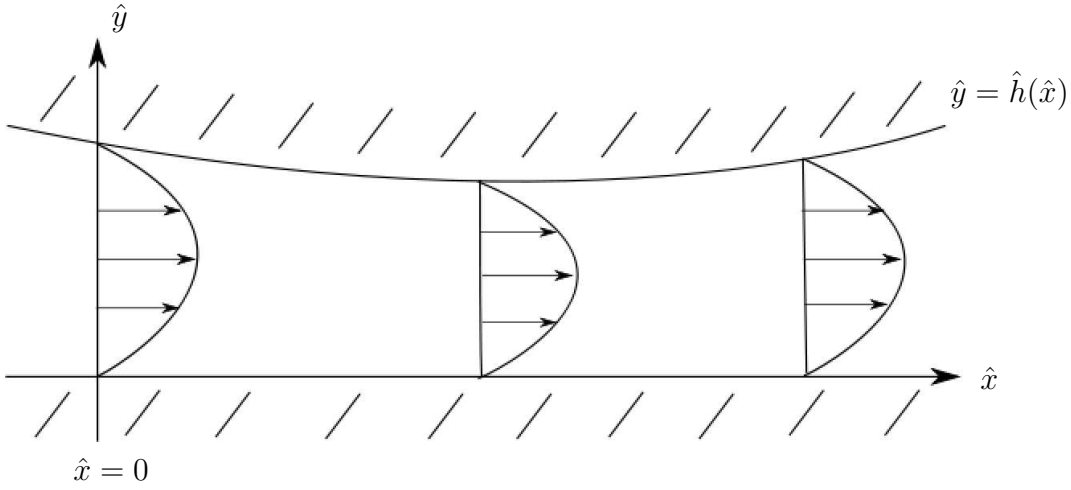

Figure 4.1: Sketch of steady pressure-driven flow in a slowly-varying channel.

In steady flow the convective derivative in equation (4.2) reduces to

$$\frac{\mathrm{D}\hat{\mathbf{u}}}{\mathrm{D}\hat{t}} = (\hat{\mathbf{u}} \cdot \hat{\nabla})\hat{\mathbf{u}}. \tag{4.4}$$

For a Newtonian fluid, $\hat{\tau}_{ij} = \hat{\eta}\hat{e}_{ij}$ (see equation (1.3)), and so the $\hat{x}$- and $\hat{y}$-components from equation (4.2) are given by

$$\hat{\rho}\hat{u}_j \frac{\partial \hat{u}_i}{\partial \hat{x}_j} = -\frac{\partial \hat{p}}{\partial \hat{x}_i} + \frac{\partial}{\partial x_j}\left(\hat{\eta}\hat{e}_{ij}\right). \tag{4.5}$$

Using the definition (1.2) of the shear rate tensor,

$$\hat{e}_{ij} = \frac{\partial \hat{u}_j}{\partial \hat{x}_j} + \frac{\partial \hat{u}_j}{\partial \hat{x}_i}, \tag{4.6}$$

equation (4.5) yields

$$\hat{\rho}\left(\hat{u}\frac{\partial \hat{u}}{\partial \hat{x}} + \hat{v}\frac{\partial \hat{u}}{\partial \hat{y}}\right) = -\frac{\partial \hat{p}}{\partial \hat{x}} + \frac{\partial}{\partial \hat{x}}\left(2\hat{\eta}\frac{\partial \hat{u}}{\partial \hat{x}}\right) + \frac{\partial}{\partial \hat{y}}\left(\hat{\eta}\left[\frac{\partial \hat{u}}{\partial \hat{y}} + \frac{\partial \hat{v}}{\partial \hat{x}}\right]\right) \tag{4.7}$$

and

$$\hat{\rho}\left(\hat{u}\frac{\partial\hat{v}}{\partial\hat{x}}+\hat{v}\frac{\partial\hat{v}}{\partial\hat{y}}\right)=-\frac{\partial\hat{p}}{\partial\hat{y}}+\frac{\partial}{\partial\hat{x}}\left(\hat{\eta}\left[\frac{\partial\hat{u}}{\partial\hat{y}}+\frac{\partial\hat{v}}{\partial\hat{x}}\right]\right)+\frac{\partial}{\partial\hat{y}}\left(2\hat{\eta}\frac{\partial\hat{v}}{\partial\hat{y}}\right). \tag{4.8}$$

The fluid is subject to no-slip and no-penetration conditions at the channel walls, $\hat{u}(\hat{x},0)=0$, $\hat{u}(\hat{x},\hat{h}(\hat{x}))=0$, $\hat{v}(\hat{x},0)=0$ and $\hat{v}(\hat{x},\hat{h}(\hat{x}))=0$. Since the flow is steady and incompressible, mass conservation requires that the volume flux per unit width $\hat{Q}$ is constant, i.e.

$$\hat{Q}=\int_0^{\hat{h}}\hat{u}\,\mathrm{d}\hat{y}=\text{constant}. \tag{4.9}$$

Note that at this point we have the choice between choosing the flux and choosing the pressure, and we have chosen to fix the flux.

4.2.1 Non-dimensionalisation

Before proceeding further we non-dimensionalise and rescale the problem. We start by non-dimensionalising using $\hat{H}$ as the characteristic length scale. We first set $\hat{x}=\hat{H}x^*$, $\hat{y}=\hat{H}y$, $\hat{u}=\hat{U}u$, $\hat{v}=\hat{U}v^*$ and $\hat{p}=\hat{P}p^*$, where $\hat{H}$, $\hat{U}$ and $\hat{P}$ are characteristic length, velocity and pressure scales. Equations (4.7) and (4.8) become

$$\frac{\hat{\rho}\hat{H}\hat{U}}{\hat{\eta}}\left(u\frac{\partial u}{\partial x^*}+v^*\frac{\partial u}{\partial y}\right)=-\frac{\hat{P}\hat{H}}{\hat{U}\hat{\eta}}\frac{\partial p^*}{\partial x^*}+2\frac{\partial}{\partial x^*}\left(\frac{\partial u}{\partial x^*}\right)+\frac{\partial}{\partial y}\left(\frac{\partial u}{\partial y}+\frac{\partial v^*}{\partial x^*}\right) \tag{4.10}$$

and

$$\frac{\hat{\rho}\hat{H}\hat{U}}{\hat{\eta}}\left(u\frac{\partial v^*}{\partial x^*}+v^*\frac{\partial v^*}{\partial y}\right)=-\frac{\hat{P}\hat{H}}{\hat{U}\hat{\eta}}\frac{\partial p^*}{\partial y}+\frac{\partial}{\partial x^*}\left(\frac{\partial u}{\partial y}+\frac{\partial v^*}{\partial x^*}\right)+2\frac{\partial}{\partial y}\left(\frac{\partial v^*}{\partial y}\right). \tag{4.11}$$

To eliminate the dimensionless group of parameters from equations (4.10) and (4.11) we choose the pressure scale $\hat{P}$ to be

$$\hat{P} = \frac{\hat{\eta}\hat{U}}{\hat{H}}, \tag{4.12}$$

which is just the usual viscous scaling for pressure in Stokes flow. Hence equations (4.10) and (4.11) become

$$\frac{\hat{\rho}\hat{H}\hat{U}}{\hat{\eta}}\left(u\frac{\partial u}{\partial x^*} + v^*\frac{\partial u}{\partial y}\right) = -\frac{\partial p^*}{\partial x^*} + 2\frac{\partial}{\partial x^*}\left(\frac{\partial u}{\partial x^*}\right) + \frac{\partial}{\partial y}\left(\frac{\partial u}{\partial y} + \frac{\partial v^*}{\partial x^*}\right) \tag{4.13}$$

and

$$\frac{\hat{\rho}\hat{H}\hat{U}}{\hat{\eta}}\left(u\frac{\partial v^*}{\partial x^*} + v^*\frac{\partial v^*}{\partial y}\right) = -\frac{\partial p^*}{\partial y} + \frac{\partial}{\partial x^*}\left(\frac{\partial u}{\partial y} + \frac{\partial v^*}{\partial x^*}\right) + 2\frac{\partial}{\partial y}\left(\frac{\partial v^*}{\partial y}\right). \tag{4.14}$$

To fix the velocity scale $\hat{U}$ we choose the dimensionless flux to be equal to one. The flux is given by

$$\hat{Q} = \int_0^{\hat{h}} \hat{u}\,\mathrm{d}\hat{y} = \hat{U}\hat{H}\int_0^h u\,\mathrm{d}y = \hat{U}\hat{H}Q \tag{4.15}$$

and so if we set $Q = \hat{Q}/(\hat{U}\hat{H}) = 1$ then

$$\hat{U} = \frac{\hat{Q}}{\hat{H}}. \tag{4.16}$$

4.2.2 Thin-film approximation

We now rescale equations (4.3), (4.13) and (4.14) by introducing the small aspect ratio $\delta = \hat{H}/\hat{L}$ with $0 < \delta \ll 1$. We define $x^* = x/\delta$ and $v^* = \delta v$, so that $\hat{x} = \hat{L}x$ and $\hat{v} = \hat{H}\hat{U}v/\hat{L}$. We implicitly consider unadorned variables to be $O(1)$. From equation (4.13), $p^* = p/\delta$, i.e. $\hat{p} = \hat{\eta}\hat{U}\hat{L}p/\hat{H}^2$, which is the usual viscous

scaling for pressure in thin-film flows (see, e.g., Acheson (1990) §7.6). The scaled and non-dimensionalised problem described by equations (4.3), (4.13), (4.14) is therefore given by

$$\frac{\partial u}{\partial x} + \frac{\partial v}{\partial y} = 0, \tag{4.17}$$

$$\frac{\partial p}{\partial x} = \frac{\partial^2 u}{\partial y^2} + \delta^2 \left[2\frac{\partial^2 u}{\partial x^2} + \frac{\partial^2 v}{\partial y \partial x} \right] - \delta^2 Re \left(u\frac{\partial u}{\partial x} + v\frac{\partial u}{\partial y} \right) \tag{4.18}$$

and

$$\frac{\partial p}{\partial y} = \delta^2 \left[2\frac{\partial^2 v}{\partial y^2} + \frac{\partial^2 u}{\partial x \partial y} \right] + \delta^4 \frac{\partial^2 v}{\partial x^2} - \delta^4 Re \left(u\frac{\partial v}{\partial x} + v\frac{\partial v}{\partial y} \right), \tag{4.19}$$

where $Re = \rho \hat{U} \hat{L}/\hat{\eta}$ is the Reynolds number. These equations are subject to the no-slip and no-penetration conditions at the channel walls $u(x,0) = 0$, $u(x,h(x)) = 0$, $v(x,0) = 0$ and $v(x,h(x)) = 0$ and the condition of prescribed flux $Q = 1$. In classical leading-order thin-film theory, we neglect inertia effects and therefore require that $\delta^2 Re = o(1)$. In this case, equations (4.18) and (4.19) reduce to

$$\frac{\partial p}{\partial x} = \frac{\partial^2 u}{\partial y^2} + o(1), \tag{4.20}$$

$$\frac{\partial p}{\partial y} = o(1). \tag{4.21}$$

Note that only even powers of δ appear in equations (4.18) and (4.19): this point will be important when we consider thixotropic fluids. At leading order in $\delta \ll 1$, equations (4.20) and (4.21) are the well-known lubrication equations

$$\frac{\partial p}{\partial x} = \frac{\partial^2 u}{\partial y^2}, \tag{4.22}$$

$$\frac{\partial p}{\partial y} = 0, \tag{4.23}$$

and the leading-order velocity in the x-direction is therefore just the classical Poiseuille parabolic profile

$$u = \frac{G}{2}(hy - y^2), \tag{4.24}$$

where $G = G(x) = -\mathrm{d}p/\mathrm{d}x$ is the leading-order pressure gradient. This classical solution will be a useful reference point as we formulate the corresponding problem for thixotropic and antithixotropic fluids.

4.3 Problem formulation and governing equations

We now consider flow of thixotropic and antithixotropic fluids in a slowly-varying channel. As in chapter 3, we will use the general rheological model presented by Mewis and Wagner (2009), which comprises an evolution equation for the structure parameter and a constitutive relation giving the shear stress tensor $\hat{\tau}_{ij}$ in terms of the shear rate tensor $\hat{e}_{ij}$ and the local value of λ. The structure equation is given by

$$\frac{\mathrm{D}\lambda}{\mathrm{D}\hat{t}} = -\hat{k}_1\dot{\gamma}^a\lambda^b + \hat{k}_2\dot{\gamma}^c(1-\lambda)^d, \tag{4.25}$$

where a, b, c and d are non-negative dimensionless exponents. The constitutive relation used throughout is

$$\hat{\tau}_{ij} = \hat{\eta}_0\lambda\hat{e}_{ij}, \tag{4.26}$$

where $\hat{\eta}_0$ is a constant viscosity parameter. Recall that the total shear rate $\dot{\gamma}$ is related to the shear rate tensor $\hat{e}_{ij}$ in the usual manner by

$$\dot{\gamma} = \sqrt{\frac{1}{2}\hat{e}_{ij}\hat{e}_{ij}}. \tag{4.27}$$

For steady flow, using (4.26), the mass conservation and momentum equations (4.1) and (4.2) yield

$$\frac{\partial \hat{u}}{\partial \hat{x}} + \frac{\partial \hat{v}}{\partial \hat{y}} = 0, \tag{4.28}$$

$$\hat{\rho}\left(\hat{u}\frac{\partial \hat{u}}{\partial \hat{x}} + \hat{v}\frac{\partial \hat{u}}{\partial \hat{y}}\right) = -\frac{\partial \hat{p}}{\partial \hat{x}} + \frac{\partial}{\partial \hat{x}}\left(\hat{\eta}_0\lambda\left[2\frac{\partial \hat{u}}{\partial \hat{x}}\right]\right) + \frac{\partial}{\partial \hat{y}}\left(\hat{\eta}_0\lambda\left[\frac{\partial \hat{u}}{\partial \hat{y}} + \frac{\partial \hat{v}}{\partial \hat{x}}\right]\right), \tag{4.29}$$

$$\hat{\rho}\left(\hat{u}\frac{\partial \hat{v}}{\partial \hat{x}} + \hat{v}\frac{\partial \hat{v}}{\partial \hat{y}}\right) = -\frac{\partial \hat{p}}{\partial \hat{y}} + \frac{\partial}{\partial \hat{x}}\left(\hat{\eta}_0\lambda\left[\frac{\partial \hat{u}}{\partial \hat{y}} + \frac{\partial \hat{v}}{\partial \hat{x}}\right]\right) + \frac{\partial}{\partial \hat{y}}\left(\hat{\eta}_0\lambda\left[2\frac{\partial \hat{v}}{\partial \hat{y}}\right]\right). \tag{4.30}$$

In steady flow,

$$\hat{u}\frac{\partial \lambda}{\partial \hat{x}} + \hat{v}\frac{\partial \lambda}{\partial \hat{y}} = -\hat{k}_1\dot{\gamma}^a\lambda^b + \hat{k}_2\dot{\gamma}^c(1-\lambda)^d, \tag{4.31}$$

where from equation (4.27)

$$\dot{\gamma}^2 = 2\left(\frac{\partial \hat{u}}{\partial \hat{x}}\right)^2 + 2\left(\frac{\partial \hat{v}}{\partial \hat{y}}\right)^2 + \left(\frac{\partial \hat{u}}{\partial \hat{y}} + \frac{\partial \hat{v}}{\partial \hat{x}}\right)^2. \tag{4.32}$$

The fluid is subject to no-slip and no-penetration conditions at the channel walls, $\hat{u}(\hat{x},0) = 0$, $\hat{u}(\hat{x},\hat{h}(\hat{x})) = 0$, $\hat{v}(\hat{x},0) = 0$ and $\hat{v}(\hat{x},\hat{h}(\hat{x})) = 0$. Since the flow is steady and incompressible, as in the Newtonian problem, the volume flux per unit width is constant, i.e.

$$\hat{Q} = \int_0^{\hat{h}} \hat{u}\,\mathrm{d}\hat{y} = \text{constant}. \tag{4.33}$$

As in the Newtonian case, we have the choice between choosing the flux and choosing the pressure, and we have chosen to fix the flux. The impact of this choice will be made apparent in later sections.

4.3.1 Non-dimensionalisation and thin-film approximation

As in section 4.2.1, we non-dimensionalise and rescale the problem. First we non-dimensionalise according to $\hat{x} = \hat{H}x^*$, $\hat{y} = \hat{H}y$, $\hat{u} = \hat{U}u$, $\hat{v} = \hat{U}v^*$ and $\hat{p} = \hat{P}p^*$ and so equations (4.29) and (4.30) become

$$\frac{\hat{\rho}\hat{H}\hat{U}}{\hat{\eta}_0}\left(u\frac{\partial u}{\partial x^*} + v^*\frac{\partial u}{\partial y}\right) = -\frac{\hat{P}\hat{H}}{\hat{U}\hat{\eta}_0}\frac{\partial p^*}{\partial x^*} + 2\frac{\partial}{\partial x^*}\left(\lambda\left[\frac{\partial u}{\partial x^*}\right]\right) + \frac{\partial}{\partial y}\left(\lambda\left[\frac{\partial u}{\partial y} + \frac{\partial v^*}{\partial x^*}\right]\right) \tag{4.34}$$

and

$$\frac{\hat{\rho}\hat{H}\hat{U}}{\hat{\eta}_0}\left(u\frac{\partial v^*}{\partial x^*} + v^*\frac{\partial v^*}{\partial y}\right) = -\frac{\hat{P}\hat{H}}{\hat{U}\hat{\eta}_0}\frac{\partial p^*}{\partial y} + \frac{\partial}{\partial x^*}\left(\lambda\left[\frac{\partial u}{\partial y} + \frac{\partial v^*}{\partial x^*}\right]\right) + 2\frac{\partial}{\partial y}\left(\lambda\left[\frac{\partial v^*}{\partial y}\right]\right), \tag{4.35}$$

To eliminate the dimensionless group of parameters from equations (4.34) and (4.35) we set

$$\hat{P} = \frac{\hat{\eta}_0\hat{U}}{\hat{H}}, \tag{4.36}$$

corresponding to (4.12) in the Newtonian case. Hence equations (4.34) and (4.35) become

$$\frac{\hat{\rho}\hat{H}\hat{U}}{\hat{\eta}_0}\left(u\frac{\partial u}{\partial x^*} + v^*\frac{\partial u}{\partial y}\right) = -\frac{\partial p^*}{\partial x^*} + 2\frac{\partial}{\partial x^*}\left(\lambda\left[\frac{\partial u}{\partial x^*}\right]\right) + \frac{\partial}{\partial y}\left(\lambda\left[\frac{\partial u}{\partial y} + \frac{\partial v^*}{\partial x^*}\right]\right) \tag{4.37}$$

and

$$\frac{\hat{\rho}\hat{H}\hat{U}}{\hat{\eta}_0}\left(u\frac{\partial v^*}{\partial x^*} + v^*\frac{\partial v^*}{\partial y}\right) = -\frac{\partial p^*}{\partial y} + \frac{\partial}{\partial x^*}\left(\lambda\left[\frac{\partial u}{\partial y} + \frac{\partial v^*}{\partial x^*}\right]\right) + 2\frac{\partial}{\partial y}\left(\lambda\left[\frac{\partial v^*}{\partial y}\right]\right). \tag{4.38}$$

To fix $\hat{U}$ we again choose the dimensionless flux to be equal to one. The flux is given by

$$\hat{Q} = \int_0^{\hat{h}} \hat{u}\,\mathrm{d}\hat{y} = \hat{U}\hat{H}\int_0^h u\,\mathrm{d}y = \hat{U}\hat{H}Q \tag{4.39}$$

and so if we set $Q = \hat{Q}/(\hat{U}\hat{H}) = 1$ then

$$\hat{U} = \frac{\hat{Q}}{\hat{H}}, \tag{4.40}$$

the same as (4.16) in the Newtonian case. We have chosen $Q = 1$ which in turn sets $\hat{H}$. We will see the impact of this in a later section.

We rescale as before by introducing the aspect ratio $\delta = \hat{H}/\hat{L}$ with $0 < \delta \ll 1$. We define $x^* = x/\delta$ and so $v^* = \delta v$, so that $\hat{x} = \hat{L}x$ and $\hat{v} = \hat{H}\hat{U}v/\hat{L}$. We again implicitly consider unadorned variables to be $O(1)$. From equation (4.37), $p^* = p/\delta$, i.e $\hat{p} = \hat{\eta}_0\hat{U}\hat{L}p/\hat{H}^2$. The scaled and non-dimensionalised problem described by (4.28), (4.29), (4.30) and (4.31) is therefore given by

$$\frac{\partial u}{\partial x} + \frac{\partial v}{\partial y} = 0, \tag{4.41}$$

$$\frac{\partial p}{\partial x} = \frac{\partial}{\partial y}\left(\lambda\frac{\partial u}{\partial y}\right) + \delta^2\left[2\frac{\partial}{\partial x}\left(\lambda\frac{\partial u}{\partial x}\right) + \frac{\partial}{\partial y}\left(\lambda\frac{\partial v}{\partial x}\right)\right] - \delta^2 Re_0\left(u\frac{\partial u}{\partial x} + v\frac{\partial u}{\partial y}\right), \tag{4.42}$$

$$\frac{\partial p}{\partial y} = \delta^2\left[2\frac{\partial}{\partial y}\left(\lambda\frac{\partial v}{\partial y}\right) + \frac{\partial}{\partial x}\left(\lambda\frac{\partial u}{\partial y}\right)\right] + \delta^4\frac{\partial}{\partial x}\left(\lambda\frac{\partial v}{\partial x}\right) - \delta^4 Re_0\left(u\frac{\partial v}{\partial x} + v\frac{\partial v}{\partial y}\right), \tag{4.43}$$

$$\delta\left(u\frac{\partial\lambda}{\partial x} + v\frac{\partial\lambda}{\partial y}\right) = -k_1\dot{\gamma}^a\lambda^b + k_2\dot{\gamma}^c(1-\lambda)^d, \tag{4.44}$$

where $Re_0 = \rho\hat{U}\hat{L}/\hat{\eta}_0$ is the Reynolds number, now defined in terms of the consistency parameter $\hat{\eta}_0$ rather than the Newtonian viscosity. These equations are subject to the no-slip and no-penetration conditions at the channel walls $u(x,0) = 0$, $u(x,h(x)) = 0$, $v(x,0) = 0$ and $v(x,h(x)) = 0$ and the condition of prescribed flux $Q = 1$. From equation (4.32)

$$\dot{\gamma}^2 = \left(\frac{\partial u}{\partial y}\right)^2 + \delta^2\left[2\left(\frac{\partial u}{\partial x}\right)^2 + 2\left(\frac{\partial v}{\partial y}\right)^2 + 2\frac{\partial u}{\partial y}\frac{\partial v}{\partial x}\right] + \delta^4\left(\frac{\partial v}{\partial x}\right)^2, \tag{4.45}$$

and the non-dimensional rate constants k_1 and k_2 are given by

$$k_1 = \hat{k}_1 \frac{\hat{Q}^{a-1}}{\hat{H}^{2(a-1)}} \quad \text{and} \quad k_2 = \hat{k}_2 \frac{\hat{Q}^{c-1}}{\hat{H}^{2(c-1)}}. \tag{4.46}$$

In the Newtonian case we were only interested in the leading-order problem; in what follows, however, we are now also concerned with first order, i.e. $O(\delta)$ terms. To ensure that inertial effects remain negligible at first order, we now require that $\delta^2 Re_0 = o(\delta)$. Equations (4.42) and (4.43) now become

$$\frac{\partial p}{\partial x} = \frac{\partial}{\partial y}\left(\lambda \frac{\partial u}{\partial y}\right) + o(\delta), \tag{4.47}$$

and

$$\frac{\partial p}{\partial y} = o(\delta). \tag{4.48}$$

We will make the assumption that k_1 and k_2 are $O(1)$, so the response timescales of the microstructure are comparable with the timescale set by the shear rate of the flow. Other regimes of behaviour could also be considered, but would require a somewhat different asymptotic approach.

4.3.2 Solution in the thin-film limit $\delta \to 0$

In the thin-film limit, $\delta \to 0$, we seek asymptotic solutions of the form

$$u = u_0 + \delta u_1 + O(\delta^2), \tag{4.49}$$

$$v = v_0 + \delta v_1 + O(\delta^2), \tag{4.50}$$

$$p = p_0 + \delta p_1 + O(\delta^2) \tag{4.51}$$

and

$$\lambda(x,y) = \lambda_0 + \delta\lambda_1 + O(\delta^2). \tag{4.52}$$

At leading order in $\delta \ll 1$, equations (4.41), (4.44), (4.47) and (4.48) yield

$$\frac{\partial u_0}{\partial x} + \frac{\partial v_0}{\partial y} = 0, \tag{4.53}$$

$$\frac{\partial p_0}{\partial x} = \frac{\partial}{\partial y}\left(\lambda_0 \frac{\partial u_0}{\partial y}\right), \tag{4.54}$$

$$\frac{\partial p_0}{\partial y} = 0 \tag{4.55}$$

and

$$\frac{\lambda_0^b}{(1-\lambda_0)^d} = \frac{k_2}{k_1}\left|\frac{\partial u_0}{\partial y}\right|^{c-a}. \tag{4.56}$$

From equation (4.55) we can immediately deduce that $p_0 = p_0(x)$, so that

$$G_0 = -\frac{\partial}{\partial y}\left(\lambda_0 \frac{\partial u_0}{\partial y}\right), \tag{4.57}$$

where $G_0 = G_0(x) = -\mathrm{d}p_0/\mathrm{d}x$ is the leading-order pressure gradient. The leading-order boundary conditions are $u_0(x,0) = 0$, $u_0(x,h(x)) = 0$, $v_0(x,0) = 0$ and $v_0(x,h(x)) = 0$.

At first order in $\delta \ll 1$, equations (4.41), (4.44), (4.47) and (4.48) yield

$$\frac{\partial u_1}{\partial x} + \frac{\partial v_1}{\partial y} = 0, \tag{4.58}$$

$$\frac{\partial p_1}{\partial x} = \frac{\partial}{\partial y}\left(\lambda_0 \frac{\partial u_1}{\partial y} + \lambda_1 \frac{\partial u_0}{\partial y}\right), \tag{4.59}$$

$$\frac{\partial p_1}{\partial y} = 0 \tag{4.60}$$

and

$$u_0\frac{\partial\lambda_0}{\partial x}+v_0\frac{\partial\lambda_0}{\partial y}=k_1\lambda_0^b\left|\frac{\partial u_0}{\partial y}\right|^a\left[(c-a)\frac{\partial u_1/\partial y}{\partial u_0/\partial y}-b\frac{\lambda_1}{\lambda_0}+d\frac{\lambda_1}{1-\lambda_0}\right]. \tag{4.61}$$

From (4.60) we can immediately deduce that $p_1 = p_1(x)$, so that to $O(\delta)$ the pressure gradient remains independent of y and

$$G_1=-\frac{\partial}{\partial y}\left(\lambda_0\frac{\partial u_1}{\partial y}+\lambda_1\frac{\partial u_0}{\partial y}\right), \tag{4.62}$$

where $G_1 = G_1(x) = -\mathrm{d}p_1/\mathrm{d}x$ is the first-order perturbation to the pressure gradient. The first-order boundary conditions are $u_1(x,0) = 0$, $u_1(x,h(x)) = 0$, $v_1(x,0) = 0$ and $v_1(x,h(x)) = 0$.

4.4 Solution in the special case $d = 0$

In order to make analytical progress and to illustrate the behaviour predicted by our theory we take $d = 0$ in equation (4.25), recalling that in this case λ may increase unboundedly (see section 1.2.5).

4.4.1 Leading order solution

We first consider the leading-order terms. From equation (4.56),

$$\lambda_0=k^{1/b}\left|\frac{\partial u_0}{\partial y}\right|^{n-1}, \tag{4.63}$$

where $n = (c-a+b)/b$ and $k = k_2/k_1$, and hence the fluid behaves, to leading order in δ, as a power-law fluid with exponent n. Equation (4.57) becomes

$$G_0=-k^{1/b}\frac{\partial}{\partial y}\left(\left|\frac{\partial u_0}{\partial y}\right|^{n-1}\frac{\partial u_0}{\partial y}\right). \tag{4.64}$$

We expect qualitatively different behaviour for different values of n: $n < 1$ corresponds to shear-thinning fluids, those whose viscosity will decrease with increased shear; $n > 1$ corresponds to shear-thickening fluids, those whose viscosity will increase with increased shear; and $n = 1$ corresponds to Newtonian behaviour with constant viscosity as λ_0 is constant. When λ_0 is given by (4.63), analytical solutions for u_0, λ_0 and v_0 can be obtained. These solutions correspond to channel flow for a power-law fluid, first solved by Flumerfelt *et al.* (1969).

The presence of the modulus sign in (4.64) means that it is important to consider separately the regions in which $\partial u_0/\partial y > 0$ and $\partial u_0/\partial y < 0$. We will assume symmetry of the flow about the centreline $y = h/2$, which simplifies the task of determining these regions. In the region $0 \leq y \leq h/2$, we expect the shear rate to be positive, $\partial u_0/\partial y > 0$, and so equation (4.64) becomes

$$G_0 k^{-1/b} = -\frac{\partial}{\partial y}\left(\left(\frac{\partial u_0}{\partial y}\right)^n\right). \tag{4.65}$$

Integrating (4.65) with respect to y and imposing the symmetry condition $\partial u_0/\partial y = 0$ at $y = h/2$ yields

$$\frac{\partial u_0}{\partial y} = \left(G_0 k^{-1/b}\left(\frac{h}{2} - y\right)\right)^{1/n}. \tag{4.66}$$

Integrating (4.66) with respect to y and imposing the no-slip condition $u_0 = 0$ at $y = 0$ yields

$$u_0 = \left(\frac{n}{n+1}\right)\left(G_0 k^{-1/b}\right)^{1/n}\left[\left(\frac{h}{2}\right)^{(n+1)/n} - \left(\frac{h}{2} - y\right)^{(n+1)/n}\right] \tag{4.67}$$

for $0 \leq y \leq h/2$. We can obtain the corresponding expression for $h/2 \leq y \leq h$ where $\partial u_0/\partial y < 0$, and so the full solution for u_0 valid for $0 \leq y \leq h$ can be

written as

$$u_0(x,y) = -\left(\frac{n}{n+1}\right)\left(G_0 k^{-1/b}\right)^{1/n}\left[\left|\frac{h}{2}-y\right|^{(n+1)/n} - \left(\frac{h}{2}\right)^{(n+1)/n}\right]. \tag{4.68}$$

Imposing the condition of prescribed flux, $Q = 1$, we can obtain an expression for the leading-order pressure gradient G_0,

$$G_0 = k^{1/b}\left(\frac{2n+1}{2n}\right)^n\left(\frac{h}{2}\right)^{-(1+2n)}. \tag{4.69}$$

Note that whether G_0 increases or decreases with n depends on the value of h. Figure 4.2 a shows G_0, given by equation (4.69), as a function of n with $k = 1$ and $h = 1$, 2 and 3. When $h > 2$, G_0 decreases as n increases, as demonstrated by the dotted line ($h = 3$). When $h = 2$, $G_0 \to k^{1/b}$ from below as $n \to \infty$ as demonstrated by the dashed line. When $h < 2$, G_0 increases as n increases, as demonstrated by the thin solid line ($h = 1$). From equation (4.69),

$$\begin{aligned}\log(G_0) &= \log(k^{1/b}) + n\log\left(\frac{2n+1}{2n}\right) - \log\left(\frac{h}{2}\right) - 2n\log\left(\frac{h}{2}\right)\\ &= \log\left(\frac{2k^{1/b}}{h}\right) + n\left[\log\left(\frac{2+1/n}{2}\right) - 2\log\left(\frac{h}{2}\right)\right],\end{aligned} \tag{4.70}$$

and so as $n \to \infty$

$$\log(G_0) \sim \log\left(\frac{2k^{1/b}}{h}\right) - 2n\log\left(\frac{h}{2}\right). \tag{4.71}$$

Therefore as $n \to \infty$

$$G_0 \sim \left(\frac{h}{2}\right)^{-2n}. \tag{4.72}$$

Equation (4.72) shows that the behaviour of G_0 as $n \to \infty$ depends on whether $h \gtrless 2$ and confirms that when $h < 2$, G_0 increases as $n \to \infty$ and when $h > 2$,

G_0 decreases as $n \to \infty$, as seen in figure 4.2 a.

This unusual condition is a consequence of the constant flux condition, (4.33), which we imposed. We will now dimensionalise (4.69) and see how $\hat{H}$, the height of the channel, effects the pressure gradient. We start with

$$\begin{aligned} G_0 \equiv -\frac{\mathrm{d}p_0}{\mathrm{d}x} &= k^{1/b}\left(\frac{2n+1}{2n}\right)^n\left(\frac{h}{2}\right)^{-(1+2n)} \\ &= \left(\frac{k_2}{k_1}\right)^{1/b}\left(\frac{2n+1}{2n}\right)^n\left(\frac{h}{2}\right)^{-(1+2n)} \\ = \left(\frac{\hat{k}_2\hat{Q}^{c-1}}{\hat{H}^{2(c-1)}}\frac{\hat{H}^{2(a-1)}}{\hat{k}_1\hat{Q}^{a-1}}\right)^{1/b}&\left(\frac{2n+1}{2n}\right)^n\left(\frac{\hat{h}}{2\hat{H}}\right)^{-(1+2n)} \end{aligned} \tag{4.73}$$

so that

$$-\frac{\mathrm{d}\hat{p}_0}{\mathrm{d}\hat{x}} = \frac{\hat{H}}{\hat{\eta}_0\hat{U}\hat{L}}\left(\frac{\hat{k}_2}{\hat{k}_1}\hat{Q}^{c-a}\right)\left(\frac{2n+1}{2n}\right)^n\left(\frac{\hat{h}}{2}\right)^{-(1+2n)}\hat{H}^{2(a-c)/b+1+2n}. \tag{4.74}$$

The powers of the $\hat{H}$ terms in (4.74) simplify so that

$$\hat{G}_0 \equiv -\frac{\mathrm{d}\hat{p}_0}{\mathrm{d}\hat{x}} = \frac{1}{\hat{\eta}_0\hat{U}\hat{L}}\left(\frac{\hat{k}_2}{\hat{k}_1}\hat{Q}^{c-a}\right)\left(\frac{2n+1}{2n}\right)^n\left(\frac{\hat{h}}{2}\right)^{-(1+2n)}\hat{H}^4. \tag{4.75}$$

We can now see how the pressure gradient varies with the lengthscale $\hat{H}$. Also, as $n \to \infty$

$$\hat{G}_0 \sim \left(\frac{\hat{h}}{2}\right)^{-2n}, \tag{4.76}$$

which is comparable with (4.72).

Substituting G_0 from (4.69) into equation (4.68) yields

$$u_0(x,y) = -\frac{(2n+1)}{2(n+1)}\left(\frac{h}{2}\right)^{-(2n+1)/n}\left[\left|\frac{h}{2}-y\right|^{(n+1)/n} - \left(\frac{h}{2}\right)^{(n+1)/n}\right], \tag{4.77}$$

and substituting G_0 from (4.69) into equation (4.63) yields the corresponding

solution for λ_0,

$$\lambda_0(x,y) = k^{1/b}\left(\frac{2n+1}{2n}\right)^{n-1}\left(\frac{h}{2}\right)^{-(2n+1)(n-1)/n}\left|\frac{h}{2}-y\right|^{(n-1)/n}. \tag{4.78}$$

From equation (4.53) we can obtain the solution for v_0,

$$\begin{aligned} v_0 &= -\int_0^y \frac{\partial u_0(y')}{\partial x}\mathrm{d}y' \\ &= -\frac{(2n+1)}{4(n+1)}h_x y\left(\frac{h}{2}\right)^{-(3n+1)/n}\left[\left|\frac{h}{2}-y\right|^{(n+1)/n} - \left(\frac{h}{2}\right)^{(n+1)/n}\right]. \end{aligned} \tag{4.79}$$

Figure 4.2 b shows u_0, given by equation (4.77), as a function of y with $b = 1$, $c = 1$, $h = 1$ and a varying such that $0.6 \leq n \leq 1.4$, corresponding to weakly shear-thinning and weakly shear-thickening fluids. (We will use a to vary n as a does not appear explicitly in equations (4.77), (4.78) and (4.79).) As n increases, the maximum value of u_0 also increases and the velocity profiles change from plug-like for smaller n, to more angular for larger n. This behaviour was also seen in the Stokes problem, where the velocity profiles became more angular for shear-thickening fluids (see section 2.2.3). When $n = 1$ we recover the familiar parabolic velocity profile (4.24) for a Newtonian fluid.

Figure 4.2 c shows λ_0, given by equation (4.78), as a function of y with $b = 1$, $c = 1$, $k = 1$, $h = 1$ and a varying such that $0.6 \leq n \leq 1.4$. Near the channel walls, $y = 0$ and $y = h$, the shear is highest, so the thixotropic fluids ($n < 1$) are most broken down and the antithixotropic fluids ($n > 1$) are most built up. In contrast, at the centreline $y = h/2$ the shear rate is zero, so for antithixotropic fluids ($n > 1$) the structure parameter λ_0 is zero at the centreline. Conversely, the effective viscosity of a shear-thinning power-law fluid becomes infinite at zero shear, so for thixotropic fluids ($n < 1$) the structure parameter becomes unbounded at the centreline, i.e. $\lambda_0 \to \infty$ as $y \to h/2$ (Myers 2005). We will

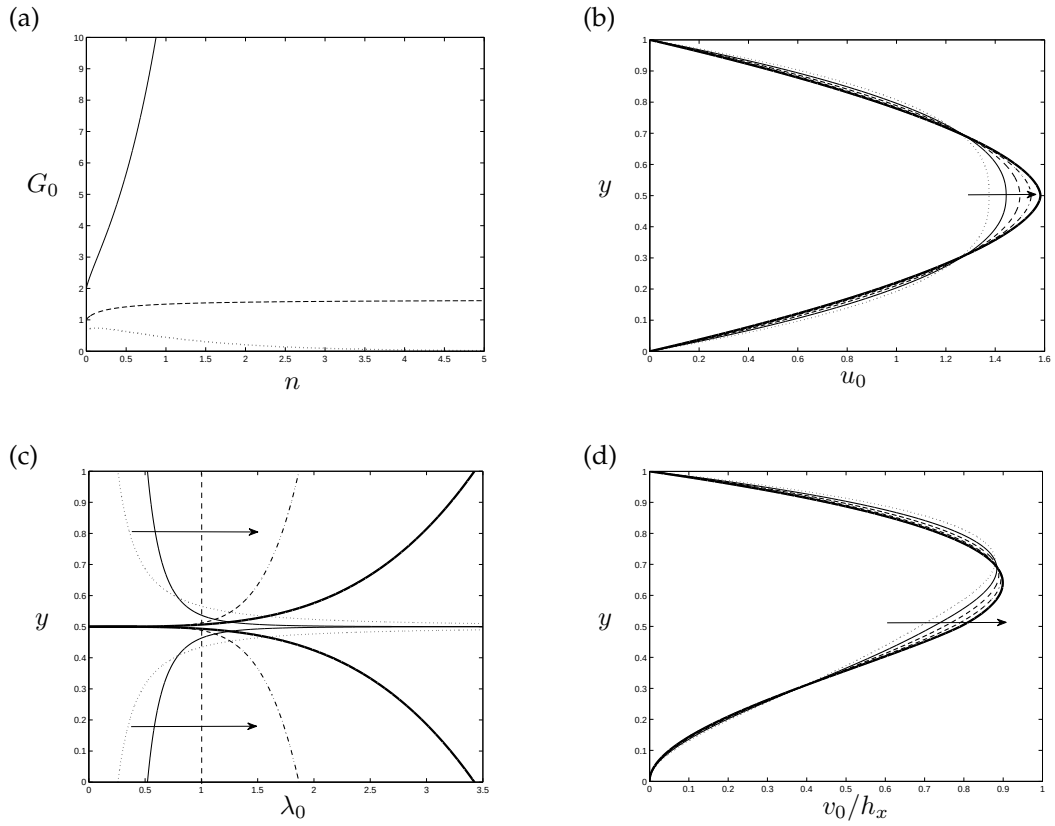

Figure 4.2: Plot (a) shows G_0, given by equation (4.69), when $k = 1$ and $h = 1$ (thin solid line), $h = 2$ (dashed line) and $h = 3$ (dotted line). Plots of (b) u_0, (c) λ_0 and (d) v_0 when $b = 1$, $c = 1$, $d = 0$, $k = 1$, $h = 1$ and a is varied such that $n = 0.6$ (dotted lines), $n = 0.8$ (thin solid lines), $n = 1$ (dashed lines), $n = 1.2$ (dot-dashed lines) and 1.4 (thick solid lines). The arrows indicate the direction of increasing n.

see in later sections that this singular behaviour is reflected in the breakdown of the asymptotic expansion near the centreline for strongly shear-thinning fluids. When $n = 1$ we recover the uniform structure of a Newtonian fluid, $\lambda_0 = 1$.

Figure 4.2 d shows v_0/h_x, given by equation (4.79), as a function of y with $b = 1$, $c = 1$, $h = 1$ and a varying such that $0.6 \leq n \leq 1.4$. As n increases the maximum value of v_0/h_x increases and its location moves towards $y = 0$, but unlike u_0, v_0/h_x is not symmetric about $y = 1/2$. The asymmetry of v_0 is because the streamlines must be parallel to the boundaries as $y \to 0$ and $y \to h$.

The gradient of the streamlines is given by

$$\frac{v_0}{u_0} = \frac{h_x y}{h}, \tag{4.80}$$

so as $y \to 0$, $v_0/u_0 \to 0$ but as $y \to h$, $v_0/u_0 \to h_x$.

4.4.2 First-order solution

In the Newtonian case, there is no $O(\delta)$ term in the asymptotic expansions of u, v and p, i.e. $u_1 = v_1 = p_1 \equiv 0$. This is not the case for the more complex fluids we are considering, since the $O(\delta)$ terms that appear in (4.44) will lead to non-zero terms at $O(\delta)$.

Rewriting equation (4.61) in the case $d = 0$ yields

$$u_0 \frac{\partial \lambda_0}{\partial x} + v_0 \frac{\partial \lambda_0}{\partial y} = k_1 \lambda_0^b \left| \frac{\partial u_0}{\partial y} \right|^a \left[(c-a) \frac{\partial u_1/\partial y}{\partial u_0/\partial y} - b \frac{\lambda_1}{\lambda_0} \right]. \tag{4.81}$$

To obtain the solution for u_1 we follow a similar method as for u_0. We can rearrange equation (4.81) to obtain an expression for λ_1, and this can be substituted into equation (4.62) to yield an ODE for u_1,

$$\frac{\partial}{\partial y} \left(n \lambda_0 \frac{\partial u_1}{\partial y} - \frac{\lambda_0^{1-b}}{b k_1} \left| \frac{\partial u_0}{\partial y} \right|^{-a} \frac{\partial u_0}{\partial y} \left(u_0 \frac{\partial \lambda_0}{\partial x} + v_0 \frac{\partial \lambda_0}{\partial y} \right) \right) + G_1(x) = 0. \tag{4.82}$$

Proceeding as before, integrating (4.82) with respect to y yields the first-order

velocity perturbation

$$u_1(x,y) = \frac{k^{1/b}h_x}{bk_2}\left(\frac{2n+1}{2n}\right)^{n-c+1}\left(\frac{h}{2}\right)^{-(2n+1)(n-c+1)/n-1}\left(\frac{n(n-1)}{n+1}\right) \times\left[-\frac{1}{3n-c+1}\left[\left|\frac{h}{2}-y\right|^{(3n-c+1)/n}-\left(\frac{h}{2}\right)^{(3n-c+1)/n}\right] +\frac{1}{2n-c}\left(\frac{h}{2}\right)^{(n+1)/n}\left[\left|\frac{h}{2}-y\right|^{(2n-c)/n}-\left(\frac{h}{2}\right)^{(2n-c)/n}\right]\right] -\frac{G_1k^{-1/b}}{n+1}\left(\frac{2n+1}{2n}\right)^{1-n}\left(\frac{h}{2}\right)^{(2n+1)(n-1)/n}\left[\left|\frac{h}{2}-y\right|^{(n+1)/n}-\left(\frac{h}{2}\right)^{(n+1)/n}\right] \quad (4.83)$$

for $0 \leq y \leq h$. Imposing the condition of prescribed flux, $Q_1 = 0$, we can obtain an expression for G_1,

$$G_1 = \frac{k^{2/b}h_x}{bk_2}\left(\frac{2n+1}{2n}\right)^{2n-c}\frac{n(2n+1)(n-1)}{(4n-c+1)(3n-c)}\left(\frac{h}{2}\right)^{-4n+2c-1}, \quad (4.84)$$

using which we obtain

$$u_1 = \frac{k^{1/b}h_x}{bk_2}\left(\frac{2n+1}{2n}\right)^{n-c+1}\left(\frac{h}{2}\right)^{2c-2n-1/n}n\left(\frac{n-1}{n+1}\right) \times\left[-\left(\frac{h}{2}\right)^{-2}\frac{(2n+1)}{(4n-c+1)(3n-c)}\left[\left|\frac{h}{2}-y\right|^{(n+1)/n}-\left(\frac{h}{2}\right)^{(n+1)/n}\right] -\left(\frac{h}{2}\right)^{-4+c/n}\frac{1}{3n-c+1}\left[\left|\frac{h}{2}-y\right|^{(3n-c+1)/n}-\left(\frac{h}{2}\right)^{(3n-c+1)/n}\right] +\left(\frac{h}{2}\right)^{-3+(c+1)/n}\frac{1}{2n-c}\left[\left|\frac{h}{2}-y\right|^{(2n-c)/n}-\left(\frac{h}{2}\right)^{(2n-c)/n}\right]\right]. \quad (4.85)$$

The first order velocity perturbation u_1 given by (4.85) has a non-integrable singularity at $y = h/2$ when $(2n-c)/n < -1$, i.e. when $n < c/3$. Furthermore, u_1 is singular but integrable, at $y = h/2$ when $-1 < (2n-c)/n < 0$, i.e. when $c/3 < n < c/2$, and so the solution is only valid when $n > c/2$.

Using the solution (4.85) for u_1, we can obtain the corresponding solution

for λ_1 from equation (4.61),

$$\lambda_1 = \frac{k^{2/b}h_x}{bk_2}(n-1)\left(\frac{2n+1}{2n}\right)^{2n-c-1}\left(\frac{h}{2}\right)^{-(2n-c-1)(2n+1)/n-1}\left|\frac{h}{2}-y\right|^{(n-1)/n} \times\left[\frac{(n-1)(2n+1)}{(4n-c+1)(3n-c)}\left(\frac{h}{2}\right)^{(2n-c)/n} -\frac{1}{n+1}\left|\frac{h}{2}-y\right|^{(n-c-1)/n}\left[\left|\frac{h}{2}-y\right|^{(n+1)/n}-\left(\frac{h}{2}\right)^{(n+1)/n}\right]\right]. \tag{4.86}$$

Figures 4.3 a and b show u_1/h_x and λ_1/h_x, given by equations (4.85) and (4.86) respectively, as functions of y with $b = 1$, $c = 1$, $k = 1$, $k_2 = 1$, $h = 1$ and a varying such $0.6 \leq n \leq 1.4$. Figure 4.3 c shows G_1/h_x, given by equation (4.84), as a function of n with $b = 1$, $c = 1$, $k = 1$, $k_2 = 1$ and $h = 1$.

The perturbations to the streamwise velocity, the structure parameter and the pressure gradient may be explained physically as follows. (Since all perturbation quantities are proportional to h_x, without loss of generality we consider an expanding channel, $h_x > 0$. We also discuss only a thixotropic fluid, $n < 1$, since the explanation for an antithixotropic fluid is simply the converse of that for a thixotropic fluid.)

In an expanding channel, the shear rate is higher upstream and lower downstream, so the microstructure of the fluid tends to be more strongly broken down upstream. Since the microstructure is advected with the fluid, this broken-down structure is carried downstream by the flow. The result of this is that, at any location, the thixotropic fluid is less structured (and its apparent viscosity is lower) than the corresponding shear-thinning generalised Newtonian fluid would be. (In terms of our asymptotic expansion, this corresponds to the condition $\lambda_1 < 0$, apparent in figure 4.3 b.) We also note from figure 4.3 b that the reduction in viscosity is more pronounced near the centre of the channel where the rate of downstream advection is highest, and is least pronounced near the

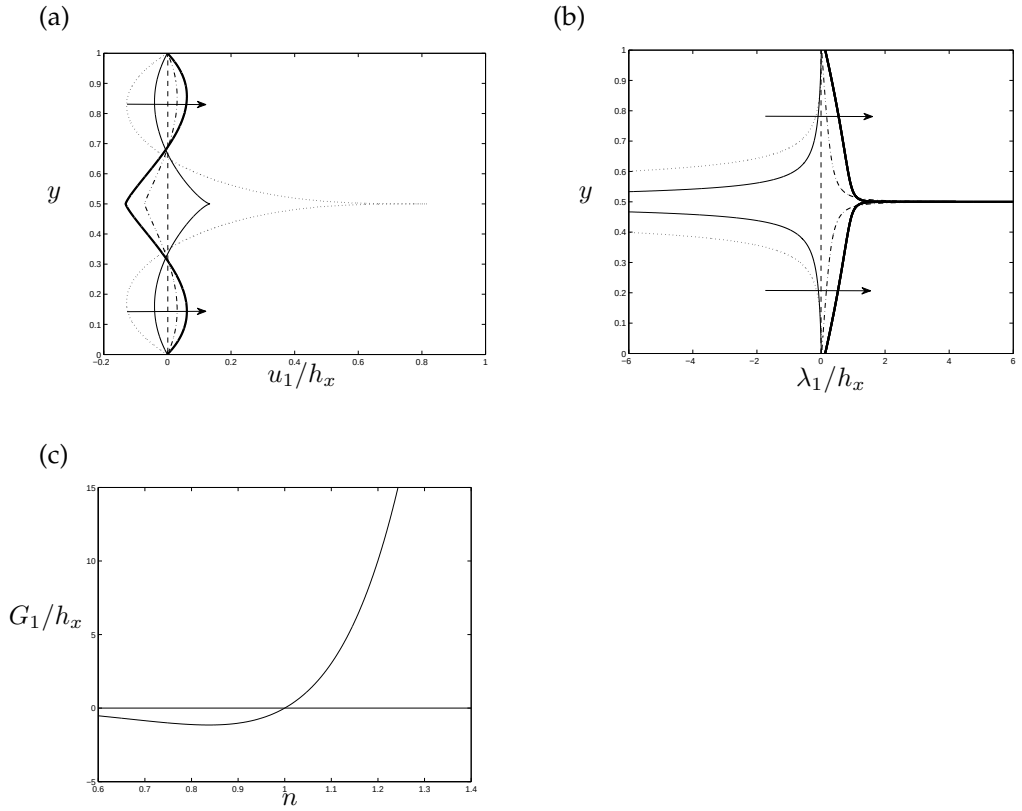

Figure 4.3: Plots of (a) u_1 and (b) λ_1 when $b = 1$, $c = 1$, $d = 0$, $k = 1$, $k_2 = 1$, $h = 1$, $\delta = 0.1$, $h_x = 1$ and a varies such that $n = 0.6$ (dotted lines), $n = 0.8$ (thin solid lines), $n = 1$ (dashed lines), $n = 1.2$ (dot-dashed lines) and 1.4 (thick solid lines). Plot (c) shows G_1/h_x, given by equation (4.84) when $b = 1$, $c = 1$, $k = 1$, $k_2 = 1$, $h = 1$ and a varies such that $0.6 \leq n \leq 1.4$. The arrows indicate the direction of increasing n.

walls where there is no advection.

This reduction in viscosity due to thixotropic effects leads to a reduction in the viscous shear stresses. In particular, the viscous stresses at the wall are reduced. Since these viscous stresses must be balanced by the driving force exerted by the streamwise pressure gradient, the effect of thixotropy is to reduce the magnitude of this pressure gradient. (In terms of our asymptotic expansion, this corresponds to the condition $G_1 < 0$, apparent in figure 4.3 c.)

The velocity perturbation u_1 must reflect both the changes in the viscosity due to thixotropy and the requirement that the net volume flux is unchanged.

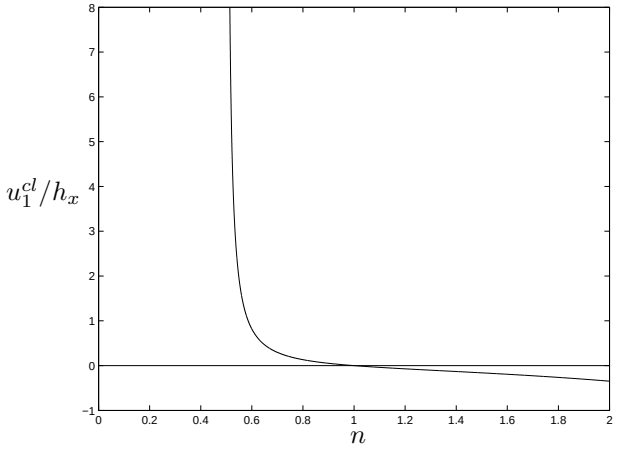

Figure 4.4: Plot shows u_1^{cl}/h_x, from equation (4.88), against n when $b = 1$, $c = 1$, $k = 1$, $k_2 = 1$, $h = 1$ and a varies such that $0 \leq n \leq 2$.

In particular, unless u_1 is identically zero, the flux condition requires that u_1 should be positive in some regions and negative in others. Near the centre of the channel, the stronger reduction in the viscosity due to thixotropy makes the fluid easier to shear, so it is in this region that the fluid moves faster ($u_1 > 0$). This faster flow near the centre of the channel must be compensated for by slower flow near the channel walls ($u_1 < 0$). This is indeed the pattern that can be observed in figure 4.3 a.

4.4.3 Behaviour of the first-order solution near the centreline $y = h/2$

As we have seen, u and λ show interesting behaviour near the centreline $y = h/2$. As $y \to h/2$, the shear rate tends towards zero, and the structure parameter tends to infinity, reflecting the singularity in the power-law model at zero shear rate (Myers 2005). This displays itself as singular behaviour of the $O(\delta)$ solutions at the centreline. When the $O(\delta)$ solutions become singular, the asymptotic expansion itself breaks down locally near the centreline since the (regular) $O(1)$ terms in the expansion are no longer dominant.

In order to examine the behaviour near the centreline, we write $y = h/2 - \epsilon$ and expand for small ϵ. Equation (4.85) becomes

$$u_1 = u_1^{cl} + \frac{k^{1/b} h_x}{b k_2} \left(\frac{2n+1}{2n}\right)^{n-c+1} \left(\frac{h}{2}\right)^{2c-2n-3} \frac{n(n-1)}{(n+1)} \times \left[-\frac{(2n+1)}{(4n-c+1)(3n-c)} |\epsilon|^{(n+1)/n} - \left(\frac{h}{2}\right)^{-2+c/n} \frac{1}{(3n-c+1)} |\epsilon|^{(3n-c+1)/n} + \left(\frac{h}{2}\right)^{-1+(c+1)/n} \frac{1}{(2n-c)} |\epsilon|^{(2n-c)/n} \right] \tag{4.87}$$

where

$$u_1^{cl} = \frac{k^{1/b} h_x}{b k_2} \left(\frac{2n+1}{2n}\right)^{n-c+1} \left(\frac{h}{2}\right)^{2c-2n-1} n \frac{(n-1)}{(n+1)} \times \left[\frac{2n+1}{(4n-c+1)(3n-c)} - \frac{n+1}{(3n-c+1)(2n-c)} \right]. \tag{4.88}$$

Figure 4.4 shows u_1^{cl}/h_x, given by equation (4.88), as a function of n, with $b = 1$, $c = 1$, $k = 1$, $k_2 = 1$ and $h = 1$ and a varying such that $0 \leq n \leq 2$. As mentioned in the previous section, the solution for u_1 is singular when $n < c/2$, i.e. when $n < 1/2$, and this will be discussed again later in this section. As $n \to 1/2^+$, u_1^{cl}/h_x increases unboundedly, and as n increases, u_1^{cl}/h_x decreases.

We are interested in the behaviour of u_1 in the limit $\epsilon \to 0$, which involves finding the dominant higher-order term in the limit $\epsilon \to 0$. Equation (4.87) contains terms proportional to $|\epsilon|^{(n+1)/n}$, $|\epsilon|^{(3n-c+1)/n}$ and $|\epsilon|^{(2n-c)/n}$. We have

$$\frac{2n-c}{n} < \frac{3n-c+1}{n} \quad \text{if and only if} \quad n > 0 \text{ or } n < -1,$$

so $|\epsilon|^{(2n-c)/n} \gg |\epsilon|^{(3n-c+1)/n}$ for all positive n. We have

$$\frac{2n-c}{n} < \frac{n+1}{n} \quad \text{if and only if} \quad 0 < n < c+1,$$

so $|\epsilon|^{(2n-c)/n} \gg |\epsilon|^{(n+1)/n}$ for $n < c+1$. When $n < c+1$, the dominant term in ϵ is proportional to $\epsilon^{(2n-c)/n}$ and when $n > c+1$ the dominant term in ϵ is proportional to $\epsilon^{(n+1)/n}$.

When $(2n-c)/n > 0$, i.e. when $n > c/2$, and $n < c+1$, we find that $u_1^{cl} \gg \epsilon^{(2n-c)/n}$ and the centreline velocity at $O(\delta)$ is finite. However, when $(2n-c)/n < 0$, i.e. when $n < c/2$, the centreline velocity is no longer finite (i.e. u_1 is singular at $y = h/2$). Thus in the regime $n < c/2$, our asymptotic solution breaks down locally in the vicinity of the centreline.

In the cases where u_1 is finite at the centreline, we can consider whether cusps or corners develop in the velocity profile. When $c/2 < n < c+1$, u_1 is given, to leading order in ϵ, by

$$u_1 \sim \frac{k^{1/b}h_x}{bk_2}\left(\frac{2n+1}{2n}\right)^{n-c+1}\left(\frac{h}{2}\right)^{2c-2n-1} n\frac{(n-1)}{(n+1)}\left[\frac{2n+1}{(4n-c+1)(3n-c)} - \frac{n+1}{(3n-c+1)(2n-c)} + |\epsilon|^{(2n-c)/n}\frac{1}{2n-c}\left(\frac{h}{2}\right)^{c/n-2}\right]. \tag{4.89}$$

The velocity profile will have a cusp if $(2n-c)/n < 1$, i.e. if $n < c$; it will have a corner if $(2n-c)/n = 1$, i.e. if $n = c$; and it will have a finite gradient at the centreline if $(2n-c)/n > 1$, i.e. if $n > c$.

When $n > c+1$, u_1 is given, to leading order in ϵ, by

$$u_1 \sim \frac{k^{1/b}h_x}{bk_2}\left(\frac{2n+1}{2n}\right)^{n-c+1}\left(\frac{h}{2}\right)^{2c-2n-1} n\frac{(n-1)}{(n+1)}\left[\frac{2n+1}{(4n-c+1)(3n-c)} - \frac{n+1}{(3n-c+1)(2n-c)} - |\epsilon|^{(n+1)/n}\frac{2n+1}{(4n-c+1)(3n-c)}\left(\frac{h}{2}\right)^{-1-1/n}\right]. \tag{4.90}$$

Since $(n+1)/n > 1$, the velocity profiles in this regime always have a finite gradient at the centreline.

Figure 4.5 illustrates this behaviour. The plots show the leading-order be-

haviour of u_1/h_x, given by equation (4.89), as a function of ϵ with $b = 1$, $c = 1$, $k = 1$, $k_2 = 1$, $h = 1$ and a varying such that $0.6 \leq n \leq 1.4$. As n increases from 0.6 to 1.4, the profiles in figures 4.5 a to d change from cusps ($n < c$) to lancet-shaped ($n > c$) near $\epsilon = 0$.

The regime $n > c + 1$, in which u_1 is given by equation (4.90), cannot be accessed with the parameter values used for plotting figures 4.5. Specifically, thus far, we have varied n by varying a where, from section 4.4.1, we know that

$$a = c - (n - 1)b, \tag{4.91}$$

and so, for $a > 0$, n satisfies

$$n < \frac{c}{b} + 1. \tag{4.92}$$

In particular, we have taken $b = 1$ and $c = 1$, and so from equation (4.92), n satisfies $n < 2$, and so we cannot access the regime $n > c + 1$. In section 4.4.4 we will instead vary n by varying c, and this will allow us to access the large-n limit.

Near the centreline, λ_1 dominates the behaviour of λ, and so the expansion breaks down. In a similar way to in the previous section, we compare the exponents of the $h/2 - y$ terms in equations (4.78) and (4.86) as $y \to h/2$ from below. Equation (4.86) contains terms proportional to $|\epsilon|^{(n-1)/n}$, $|\epsilon|^{(2n-c-2)/n}$ and $|\epsilon|^{(3n-c-1)/n}$. We have

$$\frac{2n - c - 2}{n} < \frac{3n - c - 1}{n} \quad \text{if and only if} \quad n > 0 \text{ or } n < -1,$$

so $|\epsilon|^{(2n-c-2)/n} \gg |\epsilon|^{(3n-c-1)/n}$ for all positive n. We have

$$\frac{2n - c - 2}{n} < \frac{n - 1}{n} \quad \text{if and only if} \quad 0 < n < c + 1,$$

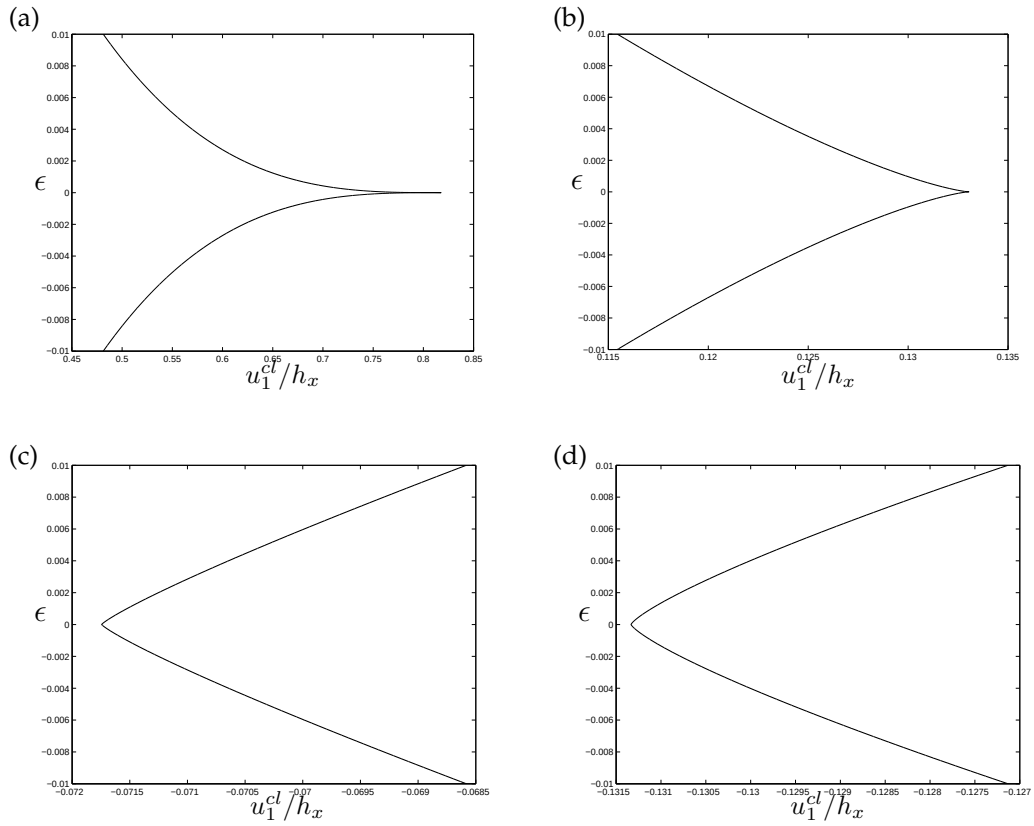

Figure 4.5: Plots of u_1^{cl}/h_x, given by equation (4.89), when $b = 1$, $c = 1$, $k = 1$, $k_2 = 1$, $h = 1$ and a varies such that (a) $n = 0.6$, (b) $n = 0.8$, (c) $n = 1.2$ and (d) $n = 1.4$.

so $|\epsilon|^{(2n-c-2)/n} \gg |\epsilon|^{(n-1)/n}$ for $n < c + 1$. When $n < c + 1$, the dominant term in ϵ is proportional to $\epsilon^{(2n-c-2)/n}$ and when $n > c + 1$, the dominant term in ϵ is proportional to $\epsilon^{(n-1)/n}$.

Therefore, when $n < c + 1$, λ_1 is given, to leading order in ϵ, by

$$\lambda_1 \sim \frac{k^{2/b} h_x}{b k_2} \left(\frac{n-1}{n+1}\right) \left(\frac{2n+1}{2n}\right)^{2n-c-1} \left(\frac{h}{2}\right)^{(-4n^2+2cn+c+2)/n} |\epsilon|^{(2n-c-2)/n} \quad (4.93)$$

and λ_0 is given, from (4.78), by

$$\lambda_0 = k^{1/b}\left(\frac{2n+1}{2n}\right)^{n-1}\left(\frac{h}{2}\right)^{(-2n^2+n-1)/n}|\epsilon|^{(n-1)/n}. \tag{4.94}$$

We have shown that in this regime $|\epsilon|^{(n-1)/n} \ll |\epsilon|^{(2n-c-2)/n}$. Therefore $\delta\lambda_1 \gg \lambda_0$, i.e. the expansion breaks down near the centreline when $n < c+1$.

When $n > c+1$, λ_1 is given, to leading order in ϵ, by

$$\lambda_1 \sim \frac{k^{2/b}h_x}{bk_2}\frac{(2n+1)(n-1)^2}{(4n-c+1)(3n-c)}\left(\frac{2n+1}{2n}\right)^{2n-c-1}\left(\frac{h}{2}\right)^{(-4n^2+2cn+n+1)/n}|\epsilon|^{(n-1)/n}, \tag{4.95}$$

and λ_0 is given by (4.94). Both λ_0 and λ_1 are of the same order in ϵ, but $\delta\lambda_1 \ll \lambda_0$, i.e. the expansion remains valid near the centreline.

4.4.4 The limit of strongly shear-thickening behaviour $n \to \infty$

For some other problems in the flow of power-law fluids, the finite-n solutions converge to a solution independent of n in the limit of strongly shear-thickening behaviour $n \to \infty$. For example, Yatim *et al.* (2010) considered thin rivulets of a power-law fluid draining down an inclined plane, and demonstrated that in the $n \to \infty$ limit the shear-thickening solutions converged to solutions independent of n. We will now investigate this limit for the present problem.

As discussed previously (section 4.4.3) the parameters used thus far ($b = 1$, $c = 1$ and varying a) restrict n such that $n < 2$. To examine the limit $n \to \infty$ we must choose different parameters, and we can most easily explore this limit by setting a and b constant and taking the limit $c \to \infty$.

We must first check that changing the parameters does not change the shear-thinning and shear-thickening behaviour seen previously. Figures 4.6 a and b show u_1/h_x and λ_1/h_x, given by equations (4.85) and (4.86), as functions of y

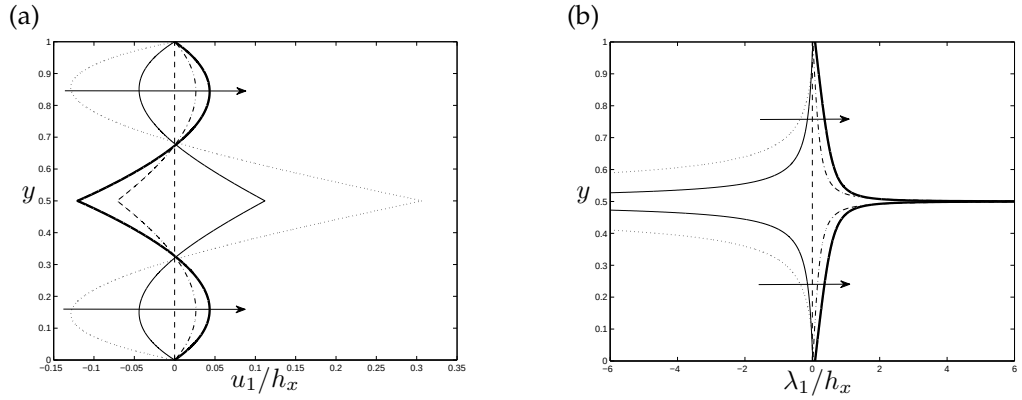

Figure 4.6: Plots of (a) u_1/h_x and (b) λ_1/h_x when $a = 1$, $b = 1$, $k = 1$, $k_2 = 1$, $h = 1$ and c varying such that $n = 0.6$ (dotted lines), $n = 0.8$ (thin solid lines), $n = 1$ (dashed lines), $n = 1.2$ (dot-dashed solid lines) and $n = 1.4$ (thick solid lines). The arrows indicate the direction of increasing n.

with $a = 1$, $b = 1$, $k = 1$, $k_2 = 1$, $h = 1$ and c varying such that $0.6 \leq n \leq 1.4$. It is clear that the shear-thinning and thickening behaviour shown in figures 4.3 a and b is also seen here.

In the limit $n \to \infty$, u_0 and v_0 each converge to a solution independent of n. Specifically, from equations (4.77) and (4.79)

$$u_0 \sim u_0^{\infty}(x, y) = -\left(\frac{h}{2}\right)^{-2}\left[\left|\frac{h}{2} - y\right| - \left(\frac{h}{2}\right)\right] \tag{4.96}$$

and

$$v_0 \sim v_0^{\infty}(x, y) = -\frac{1}{2}h_x y\left(\frac{h}{2}\right)^{-3}\left[\left|\frac{h}{2} - y\right| - \left(\frac{h}{2}\right)\right] \tag{4.97}$$

as $n \to \infty$. The limiting behaviour of u_1, given by equation (4.85), is more

complicated,

$$u_1 \sim u_1^{\infty}(x,y) = \frac{k^{1/b}h_x}{bk_2}\left(\frac{h}{2}\right)^{2(a-c+bc-2b)/b}\left[\frac{-2}{(4-b)(3-b)}\left[\left|\frac{h}{2}-y\right|-\left(\frac{h}{2}\right)\right]\right.$$
$$-\left(\frac{h}{2}\right)^{b-2}\frac{1}{3-b}\left[\left|\frac{h}{2}-y\right|^{3-b}-\left(\frac{h}{2}\right)^{3-b}\right]$$
$$\left.+\left(\frac{h}{2}\right)^{b-1}\frac{1}{2-b}\left[\left|\frac{h}{2}-y\right|^{2-b}-\left(\frac{h}{2}\right)^{2-b}\right]\right]. \tag{4.98}$$

Both u_0^{∞} and v_0^{∞} are independent of c and n, but u_1^{∞} still depends on c through the exponent of

$$U_1^{\infty} = \left(\frac{h}{2}\right)^{2(a-c+bc-2b)/b}. \tag{4.99}$$

The magnitude of u_1 depends on the behaviour of b and h. For $b > 1$ and $h > 2$, and for $b < 1$ and $h < 2$, the magnitude of u_1 increases unboundedly as $c \to \infty$. For $b < 1$ and $h > 2$, and for $b > 1$ and $h < 2$, the magnitude of u_1 tends to zero as $c \to \infty$.

We can also obtain expressions for λ_0 and λ_1, given by equations (4.78) and (4.86), in the limit $n \to \infty$,

$$\lambda_0 \sim \lambda_0^{\infty} = k^{1/b}\Lambda_0^{\infty}\left|\frac{h}{2}-y\right| \tag{4.100}$$

where

$$\Lambda_0^{\infty} = \left(\frac{h}{2}\right)^{-2n}, \tag{4.101}$$

and

$$\lambda_1 \sim \lambda_1^{\infty} = \frac{2k^{2/b}h_x}{bk_2(4-b)(3-b)}\Lambda_1^{\infty}\left|\frac{h}{2}-y\right| \tag{4.102}$$

where

$$\Lambda_1^{\infty} = n\left(\frac{h}{2}\right)^{2c-4c/b}. \tag{4.103}$$

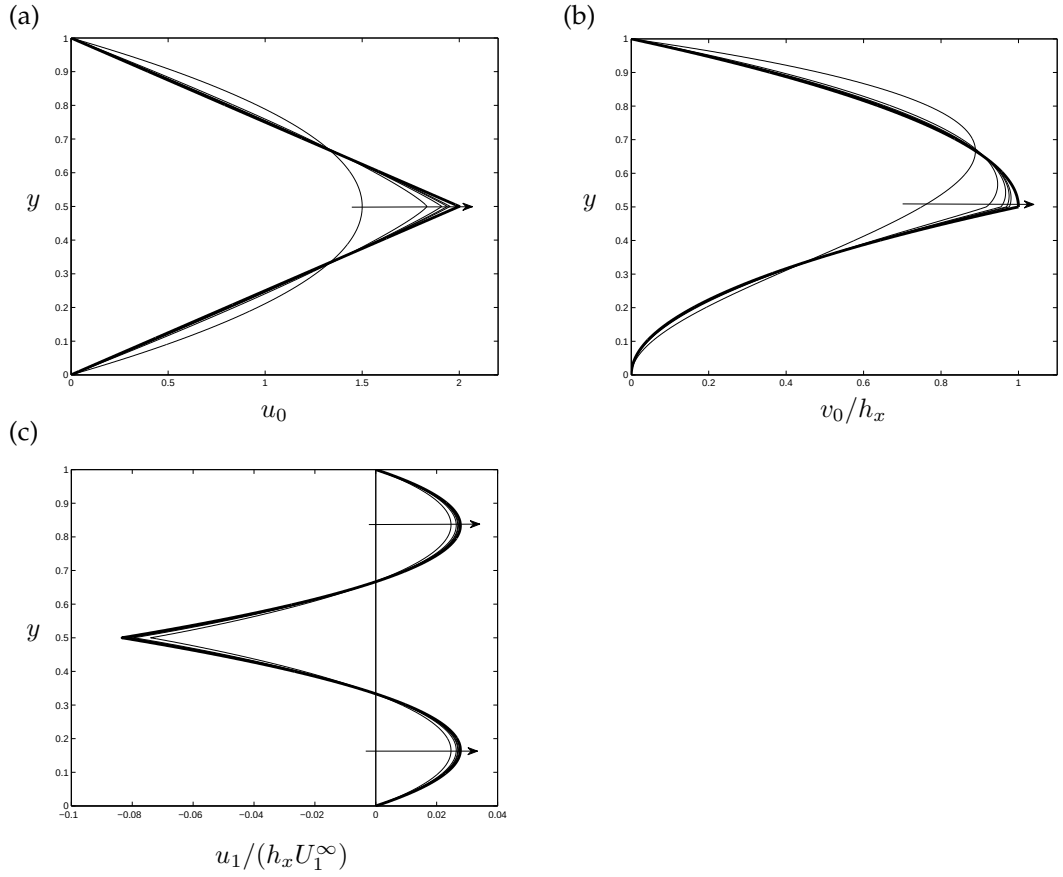

Figure 4.7: Plots of (a) u_0, (b) v_0/h_x and (c) $u_1/(h_xU_1^\infty)$ with thin lines denoting equations (4.77), (4.79) and (4.85) respectively and thick lines denoting equations (4.96), (4.97) and (4.98) respectively. For all plots $a = 1$, $b = 1$, $h = 1$, $k = 1$ and $k_2 = 1$ and c varies such that $n = 1$, 5, 10, 15 and 20. The arrows indicate the direction of increasing n.

Note that both λ_0 and λ_1 depend on n and c.

Figure 4.7 a shows u_0 with $a = 1$, $b = 1$, $h = 1$, $k = 1$ and $k_2 = 1$ and c varying such that $n = 1$, 5, 10, 15 and 20. The thick line represents the asymptotic solution for large n, u_0^∞ from (4.96), while the thin lines denote equation (4.77); the arrows indicate the direction of increasing n. It is clear that as n increases, the velocity profiles approach the piecewise linear limiting solution (4.96), and the centreline velocity increases. The finite-n solution from equation (4.77) tends towards the solution from equation (4.96).

Figure 4.7 b shows v_0/h_x with $a = 1$, $b = 1$, $h = 1$, $k = 1$ and $k_2 = 1$ and c varying such that $n = 1$, 5, 10, 15 and 20. The thick line represents the asymptotic solution for large n, v_0^∞/h_x from (4.97) and the thin lines denote equation (4.79); the arrows indicate the direction of increasing n. As n increases, the velocity profiles change from having a smooth maximum to having a corner. In the limit $n \to \infty$ the profiles become two parabolas joined at the centreline. The finite-n solution from equation (4.79) tends towards the solution from equation (4.97).

Figure 4.7 c shows the rescaled velocity perturbation $u_1/(h_x U_1^\infty)$ with $a = 1$, $b = 1$, $h = 1$, $k = 1$ and $k_2 = 1$ and c varying such that $n = 1$, 5, 10, 15 and 20. The thick line represents the asymptotic solution for large n, $u_1^\infty/(h_x U_1^\infty)$ from (4.98) and the thin lines denote equation (4.85); the arrows indicate the direction of increasing n. As n increases, the first-order velocity increases near the channel walls and decreases towards the centre of the channel. The finite-n solution from equation (4.85) tends towards the solution from equation (4.98).

Figure 4.8 a shows the rescaled structure parameter $\lambda_0/\Lambda_0^\infty$ with $a = 1$, $b = 1$, $h = 1$, $k = 1$ and $k_2 = 1$ and c varying such that $n = 1$, 5, 10, 15 and 20. The thick line represents the asymptotic solution for large n, $\lambda_0^\infty/\Lambda_0^\infty$ from (4.100) and the thin lines denote equation (4.78); the arrows indicate the direction of increasing n. As n increases, the structure parameter increases near the channel walls and decreases towards zero in the centre of the channel. The finite-n solution from equation (4.78) tends towards the solution from equation (4.100).

Figure 4.8 b shows the rescaled structure parameter perturbation $\lambda_1/(h_x \Lambda_1^\infty)$ with $a = 1$, $b = 1$, $h = 1$, $k = 1$ and $k_2 = 1$ and c varying such that $n = 1$, 5, 10, 15 and 20. The thick line represents the asymptotic solution for large n, $v_0^\infty/(h_x \Lambda_1^\infty)$ from (4.102) and the thin lines denote equation (4.86); the arrows indicate the direction of increasing n. As n increases the structure parameter

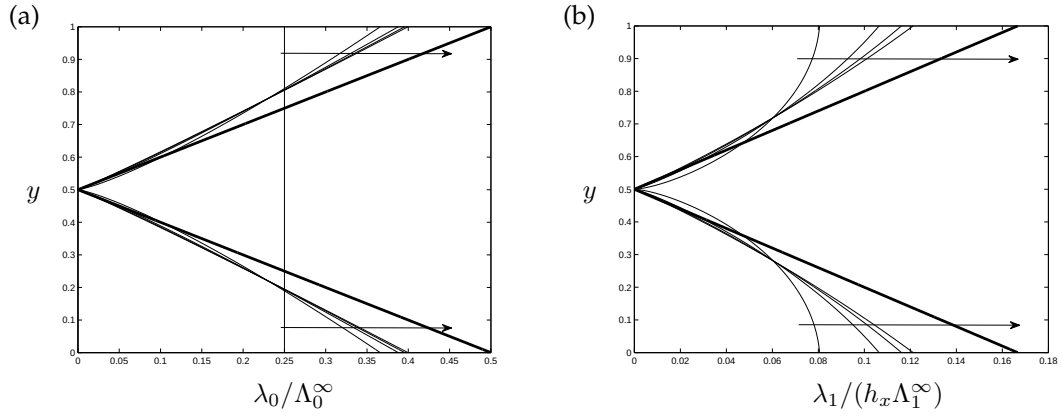

Figure 4.8: Plots of (a) $\lambda_0/\Lambda_0^\infty$ and (b) $\lambda_1/(h_x\Lambda_1^\infty)$ with thin lines given by equations (4.78) and (4.86) respectively and thick lines given by equations (4.100) and (4.102) respectively. For all plots $a = 1$, $b = 1$, $h = 1$, $k = 1$ and $k_2 = 1$ and c varies such that $n = 1$, 5, 10, 15 and 20. The arrows indicate the direction of increasing n.

increases near the channel walls, and as we move towards the centre of the channel the structure parameter decreases towards zero at the centreline.

4.5 Summary

In this chapter we have considered the two-dimensional flow of a thixotropic or antithixotropic fluid along a two-dimensional slowly-varying channel. Although several previous studies (e.g. Huynh *et al.* (2005) and Livescu *et al.* (2011)) had considered similar geometries, ours appears to be the first systematic development of a thin-film theory for a thixotropic or antithixotropic fluid.

Like the conventional lubrication approach for a Newtonian fluid, our approach was based on an asymptotic expansion in powers of the aspect ratio δ, in the limit $\delta \to 0$. Under appropriate conditions concerning the Reynolds number and the dimensionless structure response rates, we obtained the governing equations for the velocity, pressure and structure parameter up to $O(\delta)$. In con-

trast to the Newtonian case, the lubrication equations included terms at $O(\delta)$, and it is at this order that thixotropic and antithixotropic effects occur.

To illustrate the effectiveness of this rather general approach, we obtained explicit solutions for the velocity and structure parameter in the special case $d = 0$, in which the fluid behaves, to leading order, like a power-law fluid.

As the power-law index n decreases (i.e. changing from an antithixotropic to a thixotropic fluid) the leading-order velocity profiles become flatter near the centre of the channel and start to form a plug-like flow. For thixotropic fluids ($n < 1$), the structure is most built up near the centre of the channel, where the shear is lowest, and most broken down near the channel walls where the shear is highest . Conversely, for antithixotropic fluids ($n > 1$) the structure is most broken down near the centre of the channel and most built up near the walls.

For thixotropic fluids ($n < 1$), in expanding channels, near the channel walls the first-order velocity perturbation is negative and near the centre of the channel it is positive (see figures 4.3 a and b). The first-order structure parameter perturbation is negative everywhere as less structured fluid is advected downstream and smallest near the channel walls. The structure parameter is thus reduced most strongly near the centre of the channel, making the fluid easier to shear and hence flow faster. The faster flow near the centre of the channel is compensated for by slower flow near the walls where the structure parameter is highest. However, for antithixotropic fluids ($n > 1$) the structure is most built up near the centre of the channel, which results in the velocity being reduced there. The converse holds near the walls of the channel. The net effect is that for flow in an expanding channel, thixotropic effects reduce the pressure gradient required to drive a given volume flux of fluid through the channel, while antithixotropic effects increase the pressure gradient required.

Although these results are interesting and physically plausible, their valid-

ity is restricted by problems related to the behaviour of the power-law model at zero shear rate (Myers 2005). At the centre of the channel the shear rate is zero and the rheological model breaks down because the leading-order structure parameter becomes unbounded. This singularity is felt more strongly at $O(\delta)$, and can cause the expansion to become locally inconsistent at the centreline as the first-order solution dominates over the leading-order solution. For sufficiently strongly shear-thinning fluids (i.e. for n sufficiently small), the velocity singularity at $O(\delta)$ means there are no meaningful solutions. However, in the limit of strongly shear-thickening behaviour, $n \to \infty$, the finite-n velocity solutions converge to solutions independent of n.

Chapter 5

Conclusions and future work

In this thesis we considered two fundamental flow problems, the Stokes problem and flow in a slowly-varying channel, for complex fluids. Specifically, we investigated these problems for thixotropic and antithixotropic fluids described by Mewis and Wagner's (2009) general structure parameter model together with a version of the constitutive law proposed by Moore (1959). In certain limits, this model reduces to the generalised Newtonian power-law model, which we also considered.

5.1 The Stokes problem

In chapters 2 and 3 of this thesis we considered the Stokes problem for power-law, and thixotropic and antithixotropic fluids, respectively. Our main motivation for studying the Stokes problem was to investigate the interplay between the timescales of the fluid response and the forcing. Therefore, the emphasis of our investigations was on the periodic oscillatory behaviour of the systems, rather than on the transient initial phase during which the system adjusts to the attracting periodic solution.

For the thixotropic and antithixotropic problems, we carried out an asymptotic analysis in the limit of small-amplitude oscillations, $\epsilon \to 0$, where ϵ is the dimensionless amplitude of the oscillations of the wall. This asymptotic analysis revealed distinct regimes of fast and slow structural response for both thixotropic and antithixotropic fluids. In the fast-adjusting regimes, the structure is an instantaneous function of the shear, and so the fluid acts like a generalised Newtonian fluid. In the slowly-adjusting regimes, the local structure is determined by a long-term average of build-up and breakdown rates. In the marginal regimes between the limits of fast and slow adjustment, the variation of the structure parameter is lagged and attenuated relative to its instantaneous equilibrium value. This hysteretic response becomes increasingly dominant in all regimes as the amplitude of oscillation increases. When this amplitude is large enough, the distinction between the fast- and slowly-adjusting regimes disappears entirely.

The boundaries of the fast- and slowly-adjusting regimes depend on the relative magnitudes of the dimensionless amplitude of oscillation ϵ and the dimensionless frequency of oscillation ω. In each regime we developed asymptotic solutions for small ϵ and numerical solutions for larger values of ϵ. In one particular regime (fast-adjusting, antithixotropic behaviour), the fluid behaves at small amplitudes like a shear-thickening power-law fluid, and this problem was investigated separately in chapter 2.

The most interesting feature of the solutions for the velocity is that for shear-thickening fluids ($n > 1$), in chapter 2, and antithixotropic fluids, in chapter 3, we find a boundary layer of finite thickness, with no motion beyond a certain distance from the wall. This arises because the viscosity of a shear-thickening fluid decreases as the shear rate decreases, so the viscosity at the edge of the boundary layer is zero and the diffusing signal cannot penetrate further into

the fluid. This is, of course, an idealised situation and experimentally we would not see the viscosity going to zero. We would most likely see the viscosity going towards some small number, and so the signal would propagate but the fluid would be far less affected than inside the boundary layer. For antithixotropic fluids, the thickness of this layer scales with $\epsilon^{\beta/2}$, where the parameter β is defined in terms of the exponents in the structure evolution equation, the velocity amplitude decays algebraically and the structure parameter decays quadratically towards the edge of the layer.

Conversely, for shear-thinning fluids ($n < 1$), in chapter 2, and thixotropic fluids, in chapter 3, the influence of the wall extends much further into the fluid than in the Newtonian case, decaying algebraically rather than exponentially with distance from the wall.

For power-law fluids, a clear qualitative indicator of shear-thickening or shear-thinning behaviour is the non-sinusoidal waveform of the velocity oscillations. For shear-thickening fluids the oscillations adopt a 'saw-tooth' form, with a rapid decrease in absolute velocity after each minimum or maximum; shear-thinning fluids adopt a 'shark-tooth' waveform which is nearly triangular with rapid reversal at each maximum. In all other regimes, at low amplitudes the velocity oscillations are sinusoidal.

For power-law fluids, the histories of shear stress at the oscillating wall differ for shear-thinning and shear-thickening cases: shear-thinning cases are characterised by gradual increases in stress followed by rapid decreases, whereas shear-thickening cases are characterised by rapid increases in stress followed by more gradual decreases. In most thixotropic and antithixotropic regimes, however, the shear stress at the wall shows surprisingly weak deviations from Newtonian behaviour. In particular, changes in the structure and the shear rate close to the wall counteract each other so that for both thixotropic and antithix-

otropic fluids the shear stress scales roughly as predicted by the small-ϵ asymptotics well beyond the regime in which this scaling is formally valid. Thixotropy affects the shear stress most obviously for large amplitudes of oscillation, when it leads to rapid variations of the shear stress shortly before and after the wall shear rate changes sign. The feedback between increasing structure and decreasing shear that leads to these variations shows up as a characteristic 'secondary loop' when the stress and shear at the wall are plotted as rheograms. The rheograms also reveal hysteresis clearly in many cases; however, it is not in general straightforward to identify the rheological characteristics of the fluid from them.

Perhaps the most unexpected finding of this work was that the regime boundaries, and thus the qualitative behaviour of the fluid, depends rather subtly on the exponents that control the buildup and breakdown rates in the structure evolution equation. This occurs because the buildup and breakdown timescales are not constants, but in general depend on the shear rate. This finding suggests that in future studies employing the structure model from Mewis and Wagner (2009), as much attention should be paid to the choice of these exponents as to the accompanying constitutive law.

5.1.1 Future work

In this thesis we have inevitably left some avenues unexplored.

The first obvious development of the Stokes problem would be to use our asymptotic approaches to examine the transient adjustment to the periodic state, which was considered numerically for power-law fluids by Ai and Vafai (2005). Another possible extension would be to investigate the response of fluid layers of finite thickness, recalling that the asymptotic solutions we have considered are for an unbounded domain. This would allow a comparison between model

predictions and experiments of the kind carried out by Balmforth *et al.* (2009), who sinusoidally oscillated a rectangular box containing kaolin slurry. Such a comparison could help fulfil Balmforth *et al.* 's (2009) suggestion that such experiments could be used as a kind of unconventional rheometer.

Another interesting extension of the Stokes problem for the power-law fluid would be to examine the strongly shear-thinning ($n \to 0^+$) and strongly shear-thickening ($n \to \infty$) limits. In chapter 4 we obtained asymptotic results for velocity and structure parameter in the limit $n \to \infty$, and so it would be interesting to consider this limit for the Stokes problem. Other authors, such as Yatim *et al.* (2010) who considered slender rivulets of power-law fluids, have been able to obtain asymptotic solutions in both the strongly shear-thinning ($n \to 0$) and strongly shear-thickening ($n \to \infty$) limits.

Another possible extension would be to consider the Rayleigh problem, sometimes called Stokes' first problem, for thixotropic and antithixotropic fluids. The Rayleigh problem concerns the flow of semi-infinite fluid (occupying $y > 0$) generated by the instantaneous tangential movement of the wall located at $y = 0$ and has a well-known solution for a Newtonian fluid (see, e.g.,Drazin and Riley 2006, §4.2). The Rayleigh problem has already been considered for a power-law fluid by Pascal (1992).

The response of the fluid to stress-based, rather than velocity-based, forcing at the wall would make an interesting study for both the power-law and thixotropic and antithixotropic fluids. A further intriguing possibility, raised by the complex time-dependence of the thixotropic and antithixotropic fluid response, would be to investigate how effectively non-sinusoidal forcing might drive net fluid transport, following the recent investigation of this question for generalised Newtonian fluids (Hossain and Daidzic 2012).

The model we considered in chapters 3 and 4 was for purely thixotropic

and antithixotropic fluids. As described in chapter 1, there are several other more complicated types of thixotropic fluids. It would be of particular interest to solve the Stokes problem for a viscoplastic thixotropic fluid, following the experimental work of Balmforth *et al.* (2009). To do so we could employ a relatively simple constitutive law such as that used by Coussot *et al.* (2002) and Huynh *et al.* (2005), or the more complicated law proposed by Billingham and Ferguson (1993), coupled to Mewis and Wagner's (2009) general structure parameter model. This potentially very rich problem could give great insight into the behaviour of viscoplastic thixotropic fluids.

5.2 Slowly-varying flow

In chapter 4 we considered the two-dimensional flow of a thixotropic or antithixotropic fluid along a slowly-varying channel. Although previous studies had considered similar geometries, ours appears to be the first systematic development of a thin-film theory for a thixotropic or antithixotropic fluid.

Like the conventional lubrication approach for a Newtonian fluid, our approach was based on an asymptotic expansion in powers of the aspect ratio δ, in the limit $\delta \to 0$. Under appropriate assumptions concerning the Reynolds number and the dimensionless structure response rates, we obtained the governing equations for the velocity, pressure and structure parameter up to $O(\delta)$. In contrast to the Newtonian case, the lubrication equations included terms at $O(\delta)$, and it is at this order that thixotropic and antithixotropic effects occur.

To illustrate the effectiveness of this rather general approach, we obtained explicit solutions for the velocity and structure parameter in the special case $d = 0$, in which the fluid behaves, to leading order, like a power-law fluid.

Although these solutions are restricted in their validity by a singularity that

develops at the centreline for thixotropic fluids, they present a physically reasonable picture of the effects of thixotropy and antithixotropy. At the centreline, the viscosity can either tend to zero (antithixotropic) or increase unboundedly (thixotropic). As we have already discussed, it is physically unlikely for a fluid to have zero viscosity, and so we would expect the viscosity to go to near zero. More complicated models, e.g. the Carreau model 1.2.2, do exist and would perhaps reveal more realistic behaviour. When less structured fluid is being advected from upstream, the velocity near the centre of the channel is increased and the velocity near the walls is reduced; the net effect is to reduce the pressure gradient required to drive the flow. The converse occurs when more structured fluid is being advected from upstream.

5.2.1 Future work

The most obvious extension to the work in chapter 4 would be to consider non-zero values of d. This would mean that the equilibrium behaviour of the fluid was no longer a simple power-law rheology. It would be interesting to see if this potentially richer problem had similarities to our work on the Stokes problem for the same model described in chapter 3, i.e. distinct regimes of fast and slow structural response.

The solutions obtained in chapter 4 have laid the foundations for investigating several further problems. We could return to some previously considered problems, and obtain solutions using our systematic asymptotic approach. One such problem worth attention is free-surface flow, as there are very few studies of free-surface flows of thixotropic fluids (Huynh *et al.* 2005). In particular, we could investigate the levelling of fluid under gravity, previously considered by Livescu *et al.* (2011), and draining of fluid down an inclined plane, previously considered by Coussot *et al.* (2002) and Liu and Zhu (2011), using our system-

atic asymptotic approach. All these problems have well-known solutions for Newtonian fluids, and tackling them for thixotropic and antithixotropic fluids would be interesting extensions of these well-known solutions.

Another possible extension would be to consider other channel flow problems. These could include problems where one or more boundaries were moving, flow down an inclined channel or considering a three-dimensional channel flow. Again all of these problems have well-known solutions for Newtonian fluids and so it would be interesting to extend them to include thixotropic and antithixotropic effects.

Despite the progress made in this thesis, evidently much remains to be learned about the behaviour of thixotropic and antithixotropic fluids. We believe that the work presented in this thesis is a useful contribution to this challenging and practically important research area.

Bibliography

Acheson, D. J. (1990). *Elementary Fluid Dynamics*. Oxford Applied Mathematics and Computing Science Series. Oxford University Press.

Ai, L. and K. Vafai (2005). An investigation of Stokes' second problem for non-Newtonian fluids. *Numerical Heat Transfer Part A – Applications* **47**, 955–980.

Ardakani, H. A., E. Mitsoulis and S. G. Hatzikiriakos (2011). Thixotropic flow of toothpaste through extrusion dies. *Journal of Non-Newtonian Fluid Mechanics* **166**, 1262–1271.

Balmforth, N. J. and R. V. Craster (1999). A consistent thin-layer theory for Bingham plastics. *Journal of Non-Newtonian Fluid Mechanics* **84**, 65–81.

Balmforth, N. J. and R. V. Craster (2001). Geophysical aspects of non-Newtonian fluid mechanics. In N. J. Balmforth and A. Provenzale (Eds.), *Geomorphological fluid mechanics*, Volume 582 of *Lecture Notes in Physics*, Chapter 2, pp. 34–51. Springer New York.

Balmforth, N. J. and J. R. de Bruyn (2013). Editorial: Viscoplastic fluids: From theory to application. *Journal of Non-Newtonian Fluid Mechanics* **193**, 1–2.

Balmforth, N. J., Y. Forterre and O. Pouliquen (2009). The viscoplastic Stokes layer. *Journal of Non-Newtonian Fluid Mechanics* **158**, 46–53.

Barnes, H. A. (1997). Thixotropy—a review. *Journal of Non-Newtonian Fluid*

Mechanics **70**, 1–33.

Barnes, H. A., J. F. Hutton and K. Walters (1989). *An Introduction to Rheology*. Elsevier.

Bautista, F., J. M. de Santos, J. E. Puig and O. Manero (1999). Understanding thixotropic and antithixotropic behaviour of viscoelastic micellar solutions and liquid crystalline dispersions. I. The model. *Journal of Non-Newtonian Fluid Mechanics* **80**, 93–113.

Billingham, J. and J. W. J. Ferguson (1993). Laminar, unidirectional flow of a thixotropic fluid in a circular pipe. *Journal of Non-Newtonian Fluid Mechanics* **47**, 21–55.

Chanson, H., S. Jarny and P. Coussot (2006). Dam break wave of thixotropic fluid. *Journal of Hydraulic Engineering* **132**, 280–293.

Chekila, A., C. Nouar, E. Plaut and A. Nemdili (2011). Subcritical bifurcation of shear-thinning plane Poiseuille flows. *Journal of Fluid Mechanics* **686**, 272–298.

Chhabra, R. P. (2010). Non-Newtonian fluids: An introduction. In A. Deshpande and J. M. Krishnan (Eds.), *Rheology of complex fluids*, Chapter 1, pp. 3–34. Springer New York.

Christov, I. C. and P. M. Jordan (2012). Comments on: "Starting solutions for some unsteady unidirectional flows of a second grade fluid" [Int. J. Eng. Sci. 43 (2005) 781]. *International Journal of Engineering Science* **51**, 326–332.

Comsol (2009). Comsol Multiphysics 3.5a. See www.comsol.com.

Corvisier, P., C. Nouar, R. Devienne and D. Lebouché (2001). Development of a thixotropic flow in a pipe. *Experiments in Fluids* **31**, 579–587.

Coussot, P., Q. D. Nguyen, H. T. Huynh and D. Bonn (2002). Avalanche be-

haviour in yield stress fluids. *Physical Review Letters* **88**, 175501.

Craster, R. V. and O. K. Matar (2009). Dynamics and stability of thin liquid films. *Reviews of Modern Physics* **81**, 1131–1198.

de Souza Mendes, P. R. (2009). Modeling the thixotropic behavior of structured fluids. *Journal of Non-Newtonian Fluid Mechanics* **164**, 66–75.

de Souza Mendes, P. R., F. S.-M. de Abreu Soares, C. M. Ziglio and M. Gonçalves (2012). Startup flow of gelled crudes in pipelines. *Journal of Non-Newtonian Fluid Mechanics* **179–180**, 23–31.

Derksen, J. J. and Prashant (2009). Simulations of complex flow of thixotropic liquids. *Journal of Non-Newtonian Fluid Mechanics* **160**, 65–75.

Drazin, P. G. and N. Riley (2006). *The Navier-Stokes Equations: a Classification of Flows and Exact Solutions*. Number 334 in London Mathematical Society Lecture Notes Series. Cambridge University Press.

Dullaert, K. and J. Mewis (2006). A structural kinetics model for thixotropy. *Journal of Non-Newtonian Fluid Mechanics* **139**, 21–30.

Fetecau, C. and C. Fetecau (2005). Starting solutions for some unsteady unidirectional flows of a second grade fluid. *International Journal of Engineering Science* **43**, 781–789.

Flumerfelt, R. W., M. W. Pierick, S. L. Cooper and R. B. Bird (1969). Generalized plane Couette flow of a non-Newtonian fluid. *Industrial and Engineering Chemistry Fundamentals* **8**, 354–357.

Fredrickson, A. G. (1970). A model for the thixotropy of suspensions. *American Institute of Chemical Engineers Journal* **16**, 436–441.

Harris, J. (1967). A continuum theory of time-dependent inelastic flow. *Rheologica Acta* **6**, 6–12.

Hayat, T., S. Asghar and A. M. Siddiqui (2004). Stokes' second problem for a Johnson–Segalman fluid. *Applied Mathematics and Computation* **148**, 697–706.

Hossain, M. S. and N. E. Daidzic (2012). The shear-driven fluid motion using oscillating boundaries. *Journal of Fluids Engineering* **134**, 051203.

Huynh, H. T., N. Roussel and P. Coussot (2005). Aging and free surface flow of a thixotropic fluid. *Physics of Fluids* **17**, 033101.

Joseph, D. J. (1990). *Fluid Dynamics of Viscoelastic Liquids*. Applied Mathematical Sciences 84. Springer-Verlag.

Khan, M., A. Anjum and C. Fetecau (2010). On exact solutions of Stokes' second problem for a Burgers fluid, I. The case $\gamma < \lambda^2/4$. *Zeitschrift für angewandte Mathematik und Physik* **61**, 697–720.

Leslie, G. A., S. K. Wilson and B. R. Duffy (2011). Non-isothermal flow of a thin film of fluid with temperature-dependent viscosity on a stationary horizontal cylinder. *Physics of Fluids* **23**, 062101.

Lighthill, J. (1978). *Waves in Fluids*. Cambridge University Press.

Liu, W. and K.-Q. Zhu (2011). A study of start-up flow of thixotropic fluids including inertia effects on an inclined plane. *Physics of Fluids* **23**, 013103.

Livescu, S., R. V. Roy and L. W. Schwartz (2011). Leveling of thixotropic liquids. *Journal of Non-Newtonian Fluid Mechanics* **166**, 395–403.

McAnally, W. H., C. Friedrichs, D. Hamilton, E. Hayter, P. Shrestha, H. Rodriguez, A. Sheremet and A. Teeter (2007). Management of fluid mud in estuaries, bays, and lakes. I: Present state of understanding on character and behaviour. *Journal of Hydraulic Engineering* **133**, 9–22.

McArdle, C. R., D. Pritchard and S. K. Wilson (2012). The Stokes boundary

layer for a thixotropic or antithixotropic fluid. *Journal of Non-Newtonian Fluid Mechanics* **185–186**, 18–38.

Mewis, J. and N. J. Wagner (2009). Thixotropy. *Advances in Colloid and Interface Science* **147–148**, 214–227.

Moore, F. (1959). The rheology of ceramic slips and bodies. *Transactions and Journal of the British Ceramic Society* **58**, 470–494.

Mujumdar, A., A. Beris and A. Metzner (2002). Transient phenomena in thixotropic systems. *Journal of Non-Newtonian Fluid Mechanics* **102**, 157–178.

Myers, T. G. (2005). Application of non-Newtonian models to thin film flow. *Physical Review E* **72**, 0663002.

Najmi, K., M. Karimzadeh and K. Sadeghy (2010). Simulating the flow of a thixotropic fluid above a fixed plate at arbitrary Reynolds numbers. *Journal of the Society of Rheology, Japan* **3**, 109–116.

Nguyen, Q. D. and D. V. Boger (1985). Thixotropic behaviour of concentrated bauxite residue suspensions. *Rheologica Acta* **24**, 427–65.

Oron, A., S. H. Davis and S. G. Bankoff (1997). Long-scale evolution of thin liquid films. *Reviews of Modern Physics* **69**, 931–980.

Pascal, H. (1992). Similarity solutions to some unsteady flows of non-Newtonian fluids of power law behaviour. *International Journal of Non-Linear Mechanics* **27**, 759–771.

Pearson, J. R. A. and P. M. J. Tardy (2002). Models for flow of non-Newtonian and complex fluids through porous media. *Journal of Non-Newtonian Fluid Mechanics* **102**, 447–473.

Péterfi, T. (1927). Die Abhebung der Befruchtungsmembran bei Seeigeleirn. *Archiv für Entwicklungsmechanik der Organismen* **112**, 660–695.

Phan-Thien, N. (2002). *Understanding Viscoelasticity: Basics of Rheology*. Springer Verlag.

Potanin, A. (2010). 3D simulations of the flow of thixotropic fluids, in large-gap Couette and vane-cup rheometers. *Journal of Non-Newtonian Fluid Mechanics* **165**, 299–312.

Pritchard, D., C. R. McArdle and S. K. Wilson (2011). The Stokes boundary layer for a power-law fluid. *Journal of Non-Newtonian Fluid Mechanics* **166**, 745–753.

Pritchard, D. and J. R. A. Pearson (2006). Viscous fingering of a thixotropic fluid in a porous medium or a narrow fracture. *Journal of Non-Newtonian Fluid Mechanics* **135**, 117–127.

Rajagopal, K. R. (1982). A note on unsteady unidirectional flows of a non-Newtonian fluid. *International Journal of Non-Linear Mechanics* **17**, 369–373.

Rajagopal, K. R. and T. Y. Na (1983). On Stokes' problem for a non-Newtonian fluid. *Acta Mechanica* **48**, 233–239.

Raju, K. S. (2011). *Fluid Mechanics, Heat Transfer, and Mass Transfer: Chemical Engineering Practice*. John Wiley & Sons.

Rile, K. F., M. P. Hobson and S. J. Bence (1998). *Mathematical Methods for Physics and Engineering*. Cambridge University Press.

Ross, A. B., S. K. Wilson and B. R. Duffy (2001). Thin-film flow of a viscoplastic material round a large horizontal stationary or rotating cylinder. *Journal of Fluid Mechanics* **430**, 309–333.

Sadeqi, S., K. Navid and K. Sadeghy (2011). Blasius flow of thixotropic fluids: a numerical study. *Communications in Nonlinear Science and Numerical Simulation* **16**, 711–721.

Schalek, E. and A. Szegvari (1923). Ueber Eisenoxydgallerten. *Kolloid-Zeitschrift* **32**, 318–319.

Shadrina, N. K. (1978). Shear flows of a thixotropic fluid. *Fluid Dynamics* **13**, 341–349. Translated from Izvestiya Akademii Nauk SSSR, Mekhanika Zhidkosti i Gaza, No. 3, pp. 3–12, 1978.

Stokes, G. G. (1851). On the effect of the internal friction of fluids on the motion of pendulums. *Transactions of the Cambridge Philosophical Society* **9**, 8–106.

Toorman, E. A. (1997). Modelling the thixotropic behaviour of dense cohesive sediment suspensions. *Rheologica Acta* **36**, 56–65.

Whelan, T. (1994). *Polymer technology dictionary*. Chapman & Hall.

Wilson, S. D. R. and S. L. Burgess (1998). The steady, spreading flow of a rivulet of mud. *Journal of Non-Newtonian Fluid Mechanics* **79**, 77–85.

Wilson, S. K., B. R. Duffy and R. Hunt (2002). Oa slender rivulet of a power-law fluid driven by either gravity or a constant shear stress at the free surface. *The Quarterly Journal of Mechanics and Applied Mathematics* **55**, 385–408.

Wilson, S. K., B. R. Duffy and A. B. Ross (2002). On the gravity-driven draining of a rivulet of a viscoplastic material down a slowly varying substrate. *Physics of Fluids* **14**, 555–571.

Worrall, W. E. and S. Tuliani (1964). Viscosity changes during the ageing of clay-water suspensions. *Transactions and Journal of the British Ceramic Society* **63**, 167–185.

Yatim, Y. M., S. K. Wilson and B. R. Duffy (2010). Unsteady gravity-driven slender rivulets of a power-law fluid. *Journal of Non-Newtonian Fluid Mechanics* **165**, 1423–1430.